



Investigations of Three Dominant Patterns of Large-Scale Circulation Variability in the Atmosphere

Citation

Ma, Ding. 2016. Investigations of Three Dominant Patterns of Large-Scale Circulation Variability in the Atmosphere. Doctoral dissertation, Harvard University, Graduate School of Arts & Sciences.

Permanent link

<http://nrs.harvard.edu/urn-3:HUL.InstRepos:33840725>

Terms of Use

This article was downloaded from Harvard University's DASH repository, and is made available under the terms and conditions applicable to Other Posted Material, as set forth at <http://nrs.harvard.edu/urn-3:HUL.InstRepos:dash.current.terms-of-use#LAA>

Share Your Story

The Harvard community has made this article openly available.
Please share how this access benefits you. [Submit a story](#).

[Accessibility](#)

Investigations of Three Dominant Patterns of Large-scale Circulation Variability in the Atmosphere

A dissertation presented

by

Ding Ma

to

The Department of Earth and Planetary Sciences

in partial fulfillment of the requirements

for the degree of

Doctor of Philosophy

in the subject of

Earth and Planetary Sciences

Harvard University

Cambridge, Massachusetts

August 2016

© 2016 Ding Ma

All rights reserved.

Chapters 2, 3, 4 and 5 are substantially based upon four articles, the information of which are listed as follows.

- Chapter 2

Ma, D., Boos, W. and Kuang, Z. (2014). Effects of orography and surface heat fluxes on the South Asian summer monsoon. *Journal of Climate*, **27**, 6647–6659.

© 2014 American Meteorological Society. Used with permission.

- Chapter 3

Ma, D. and Kuang, Z. (2016). A mechanism-denial study on the Madden-Julian Oscillation with reduced interference from mean state changes. *Geophysical Research Letters*, **43**, 2989–2997.

© 2016 American Geophysical Union. Used with permission.

- Chapter 4

Ma, D. and Kuang, Z. (2011). Modulation of radiative heating by the Madden-Julian Oscillation and convectively coupled Kelvin Waves as observed by CloudSat. *Geophysical Research Letters*, **38**, L21813.

© 2011 American Geophysical Union. Used with permission.

- Chapter 5

Ma, D., Hassanzadeh, P. and Kuang, Z. (2016). Quantifying the eddy-jet feedback strength associated with the annular mode in an idealized GCM and reanalysis data. *Journal of the Atmospheric Sciences*, under review.

Dissertation Advisor:
Professor Zhiming Kuang

Author:
Ding Ma

Investigations of Three Dominant Patterns of Large-scale Circulation Variability in the Atmosphere

Abstract

This work covers the investigations of three dominant patterns of large-scale circulation variability in the atmosphere, namely the South Asian summer monsoon, the Madden-Julian Oscillation (MJO) and the annular mode.

The role of the orography on South Asian monsoon is comprehensively examined using numerical simulations. The results show that the Tibetan Plateau creates a strong monsoon mainly by insulating the thermal maximum south of the Himalayas from extratropical air, as the monsoon strength is not sensitive to the orography and surface heating perturbations north of the Himalayas. It is also found that free-tropospheric moisture anomaly may lead to deviations from the theory of strict convective quasi-equilibrium, implying complexities that need to be included in existing theories of monsoon strength.

The MJO is the dominant mode of intraseasonal variability in the tropics. A mechanism-denial study is conducted to examine the importance of different physical processes to the MJO using numerical modeling. The results show that the essential MJO dynamics are internal to the equatorial Indian and Pacific Oceans. The wind-evaporation feedback tend to slow down propagation of the MJO and the radiative-convective feedback is important to MJO amplitude. In an observational study, the vertical distributions of radiative heating anomalies associated with the MJO is constructed using radiative heating profiles from CloudSat. Bottom-heavy radiative heating is seen in actively convecting regions of the MJO, which is argued to strengthen the MJO.

The annular mode corresponds to the meridional shift of the eddy-driven jet. Using

a linear response function (LRF), the present study confirms unequivocally a positive eddy feedback in the annular mode dynamics in an idealized GCM. The strength of the eddy-jet feedback is accurately quantified, and the result from the LRF is used to evaluate three statistical methods. Because of the quasi-oscillatory nature of eddies, the mean-state-independent eddy forcing reduces the accuracy of two statistical methods proposed by previous studies. The results from a new method proposed here converge to the value produced by the LRF as the mean-state-independent eddies are mostly filtered out. The statistical methods are then applied to the reanalysis data.

Contents

Abstract	iii
Acknowledgments	xii
1 Introduction	1
1.1 South Asian summer monsoon	2
1.2 Madden-Julian Oscillation	3
1.3 Annular mode	4
2 Effects of Orography and Surface Heat Fluxes on the South Asian Summer Monsoon	5
2.1 Introduction	6
2.2 Model and methods	9
2.3 Results and discussions	14
2.4 Conclusions	27
3 A mechanism-denial study on the Madden-Julian Oscillation with reduced interference from mean state changes	29
3.1 Introduction	30
3.2 Methodology	32
3.2.1 Model	32
3.2.2 Experimental setup	33
3.3 Results	34
3.4 Discussions and summary	41
4 Modulation of radiative heating by the Madden-Julian Oscillation and convectively coupled Kelvin waves as observed by CloudSat	44
4.1 Introduction	45
4.2 Data and method	46
4.3 Results	48
4.4 Discussions and summary	55

5	Quantifying the eddy-jet feedback strength of the annular mode in an idealized GCM and reanalysis data	57
5.1	Introduction	58
5.2	Methodology	60
5.3	Annular mode and eddy-jet feedback	62
5.3.1	Jet climatology and annular mode structure	62
5.3.2	Simple model of feedback	63
5.4	Eddy-jet feedback strength	67
5.4.1	Linear response function	72
5.4.2	Fitting cross-correlation functions	76
5.4.3	Lag regressions	76
5.4.4	Low-pass filtering	79
5.4.5	Application to the reanalysis data	80
5.5	Discussions and summary	83
6	Summary and future directions	90
6.1	South Asian summer monsoon	90
6.2	Madden-Julian Oscillation	92
6.3	Annular mode	93
	Appendix A Nudging on effective timescales longer than intraseasonal timescale	95
	References	98

List of Tables

2.1	Experiments configuration. The elevations of the altered orography in HIM90, HIM66, HIM33 and FLAT are denoted by the thin grey contours in Figures 2.2ABCD with interval of 1200 m. A sensible heat sink of 150 W m^{-2} is prescribed in the land-surface scheme in the first group of experiments with reduced surface sensible heat fluxes. In the second group of experiments with reduced surface sensible heat fluxes, the magnitude of surface sensible heat fluxes forcing follows the distribution of differences between θ_{eb} values for the FLAT experiment and those for the CONTROL experiment. TIBET includes the part of the Tibetan Plateau north of the Himalayas as denoted by the thick black contour in Figure 2.2E. HIM (thick black contour in Figure 2.2F) is defined as the region above 1200 m on the southern slope of the Himalayas, 70°E - 100°E , and covers $7.6 \times 10^5 \text{ km}^2$. INDIA (thick black contour in Figure 2.2G) covers the same areal extent as HIM, and is directly south of and adjacent to the HIM. INDIA2 (thick black contour in Figure 2.2H) is defined as the region with the highest θ_{eb} in the CONTROL covering $7.6 \times 10^5 \text{ km}^2$. THERM (thick black contour in Figure 2.6A) is the region south of the Himalayas, north to 22.5°N , 67°E - 90°E	11
3.1	Brief description of the experiments. See text for details.	33

List of Figures

2.1	The thermodynamic structure, precipitation and wind from observations, reanalysis data and the CONTROL. (A) ERA-40 temperature averaged between 175-450 hPa. (B) ERA-40 θ_{eb} : θ_e about 20 hPa above the surface. (C) Vertical-meridional distributions of the θ_e from the ERA-40 averaged between 70°E-95°E along the lines at the same relative latitude with respect to the peaks of the Himalayas (indicated by the thick white curve in A). (D) TRMM precipitation rate (color shading) and ERA-40 850 hPa winds (vectors). The right column (EFGH) shows the corresponding properties of averages of ensemble members from the CONTROL experiment. In F, the white box denotes the domain in which regions covering $3.7 \times 10^6 \text{ km}^2$ of the highest θ_{eb} are identified to calculate the maximum θ_{eb} over northern India. The black box indicates the domain in the Equatorial Indian Ocean where the reference θ_e^* is averaged over for $\Delta\theta_{ec}$. In ABDEFH, the grey contours denote elevations with the interval of 1200 m. In CG, the grey curve shows the maximum height of the orography along the relative latitude, so that below the grey curve, along each relative latitude there are different numbers of invalid data points that are not considered into the average. In H, the red box defines the region to calculate the mWYI.	8
2.2	The spatial distribution of θ_{eb} averaged for June, July and August (color shading). The thick white contours denote the regions covering $3.7 \times 10^6 \text{ km}^2$ of the highest θ_{eb} within 50°E-100°E, 15°N-30°N. The thin grey contours denote elevations with the interval of 1200 m. In the lower panels, the thick black contours show the regions where a sensible heat sink is applied on the surface.	12
2.3	Spatial distribution of the regression coefficient between the θ_{eb} and the mWYI from the CONTROL. Color shading represents the regression coefficients ($\text{K m}^{-1} \text{ s}$) that are statistically significant at 95% confidence level. The thick black contours indicate regions with correlation coefficients of 0.3 and 0.7. The thin grey contours denote elevations with interval of 1200 m.	16

2.4	The monsoon strength plotted against the maximum elevation of the orography in South Asia in the experiments with altered orography (A), and against total surface sensible heat flux forcing in the experiment with sensible heat sink (B). The averaged mWYI of 10 ensemble members is shown with error bars for CONTROL, TIBET, HIM, INDIA and INDIA2; the data from individual simulations is plotted for HIM90, HIM66, HIM33 and FLAT, because there are only three ensemble members for each of these experiments.	18
2.5	The monsoon strength (indicated by mWYI) regressed against $\Delta\theta_{ec}$ (i.e., the difference between the maximum θ_{eb} over South Asia and the average free tropospheric θ_e^* over the Equatorial Indian Ocean) in the experiments with altered orography (A), and reduced surface sensible heat fluxes (B). Each marker stands for an individual ensemble member, and the black line denotes the regression line.	20
2.6	(A) Same as Figure 2.2, but for the THERM1 experiment. (B) Same as Figure 2.5, but for the second group of experiments with reduced surface heat fluxes. Each marker stands for an individual integration from CONTROL, THERM1, THERM2 and THERM3, and the red solid line denotes the regression line for these simulations. As reference, the black dashed line is the same as the regression line in Figure 2.5B for the first group of experiments with reduced sensible heat fluxes, and the blue dashed line is the same as the regression line in Figure 2.5A for the experiments with altered orography.	22
2.7	(AB) Same as Figure 2.5, but the mWYI is regressed against the difference of between the free tropospheric θ_e^* averaged over the regions covering $3.7 * 10^6$ km ² of the highest θ_{eb} and the average free tropospheric θ_e^* over the Equatorial Indian Ocean. (CD) Same as AB, but θ_e^* anomalies averaged over the regions covering $3.7 * 10^6$ km ² of the highest θ_{eb} are plotted against θ_{eb} anomalies averaged in the same region. The dashed blue lines indicate the identity line. (EF) Same as CD, but the anomalous relative humidity between 400 and 700 hPa is plotted against θ_{eb} anomalies averaged over the regions covering $3.7 * 10^6$ km ² of the highest θ_{eb}	24
2.8	(A) Same as Figure 2.1G, but for the relative humidity of the CONTROL. (Middle and bottom panels) Same as A, but for the relative humidity difference between the experiments and the CONTROL.	26
3.1	Mean precipitation (shaded) and OLR variance of the MJO (black contours) from the (A) CTL, (B) NDG, (C) CHNn, (D) CHN, (E) BOX, (F) FLX and (G) RAD. The silver contours denote the coast lines.	35

3.2	Time-space power spectra of the OLR averaged between 20°S-0° of (A) CTL, (B) NDG, (C) CHNn, (D) CHN, (E) BOX, (F) FLX and (G) RAD.	37
3.3	Temporal and zonal mean eddy forcing in (A) CTL, (B) CHN and (C) CHN2. In (B) and (C), the dashed lines denote the latitudes starting from which the extratropical eddies are damped. The relaxation rate increases linearly poleward till the solid lines, and remains constant poleward from the solid lines.	38
3.4	Temporal and zonal mean circulation in (A) CTL, and anomalous circulation in (B) CHNn and (C) CHN. Negative streamfunction values (dashed contours) correspond to clockwise circulation, and positive streamfunction values (solid contours) correspond to counter-clockwise circulation.	40
4.1	The 4-year climatology of radiative heating averaged between 10°S and 10°N (A) SW, (B) LW, (C) total radiative heating, (D) total cloud water content, and (E) the number of days for which the identified active centers of the MJO/KWs fall in a particular 2.5 degrees longitude bin.	49
4.2	The vertical-longitudinal distributions of anomalous (A) SW, (B) LW, (C) total radiative heating, (D) total cloud water, (E) temperature, and (F) water vapor associated with the MJO.	51
4.3	Same as Figure 4.2, but for the KWs.	53
4.4	(A) Normalized vertical distribution of radiative heating and (B) total cloud water content. The solid red and blue with stars are for the MJO and KWs anomalies respectively, using the full 4-year dataset. The dashed lines are results from two 2-year subsets of the data.	54
5.1	(A) Climatology of zonal mean zonal wind in the reanalysis data. Anomalous (B) zonal mean zonal wind and (C) zonal mean temperature regressed on the leading PC of $\langle [u] \rangle$	64
5.2	The same as Figure 5.1, except for model outputs of CTL.	64
5.3	Summary statistics for z and m in the reanalysis data. Power spectrum of (A) z and (B) m , and autocorrelations of (C) z and (D) m	65
5.4	Cross-correlation between z and m in the reanalysis data (black curve), and between \tilde{z} and \tilde{m} (i.e., without eddy feedback following LH01). Positive values of lag denote that zonal index leads eddy forcing.	68

5.5	The same as Figure 5.3, except for model outputs of CTL.	69
5.6	The same as Figure 5.4, except for model outputs of CTL.	70
5.7	The difference of (A) zonal mean zonal wind, (B) zonal mean temperature, (C) zonal average eddy momentum flux and (D) zonal average eddy heat flux between EXP and CTL.	71
5.8	Strength of eddy-jet feedback estimated in the idealized GCM following different methods: (A) LH01, (B) S13 and (C) low-pass filtering. The red lines in each panel shows the value calculated using the LRF. The dashed lines denoting 95% confidence intervals	74
5.9	Power spectrum of the total eddy forcing (black) and the mean-state-independent eddy forcing (red).	75
5.10	The ratio between the total eddy forcing calculated from daily wind anomalies and that calculated from 6-hourly wind anomalies for (A) model outputs of CTL and (B) the reanalysis data.	77
5.11	The same as Figure 5.7, except for the second EOF of zonal mean zonal wind.	78
5.12	Real component of $\frac{MZ^*}{ZZ^*}$ in CTL, with the dashed curves denoting 95% confidence intervals.	81
5.13	Similar to Figure 5.8, except for the reanalysis data.	82
5.14	Anomalous zonal average (A) eddy momentum flux and (B) eddy heat flux associated with the Southern annular mode in the reanalysis data.	84
5.15	Modulus of Z/\tilde{M} from model outputs (black dashed curve) and least squares fitting (black solid curve) for model outputs of CTL.	88
S1	(A) the weight function of the moving average. (B) the effective damping time of the nudging term on oscillations with different periods. The red star denotes that for the oscillations with a period of 68 days, the effective damping time is the same as the period.	97

Acknowledgments

General

My deepest thanks go to my adviser, Zhiming Kuang, who has always been a great inspiration to me through this long journey. I would also like to thank the other members of my committee, Brian Farrell, Peter Huybers and Eli Tziperman, for their helpful advice. I thank all members of the Kuang group and other friends in the Earth and Planetary Sciences department, and it is my honor to study and work with these talented people. I am also grateful to the administrations in the department, who have been kind to help and advise in their respective roles. Finally, thank you to my parents and my wife for their love, patience and constant support.

Chapter 2

This research is supported by NSF grants AGS-0754332 and AGS-1062016 and a grant from Harvard's Asia center. The authors thank Peter Molnar and two anonymous reviewers for very constructive comments.

Chapter 3

This research is supported by NASA grant NNX13AN47 and DOE grant DE-SC0008464. The authors thank Jeffrey Shaman and Nathan Arnold for helping with model configuration and two anonymous reviewers for constructive reviews.

Chapter 4

The research is supported by NSF grant AGS-1062016 and DOE grant DE-FG02-08ER64556 as part of the Atmospheric System Research program. The authors thank Adam Sobel and an anonymous reviewer for very constructive and helpful reviews, Joe Andersen for

valuable codes to start this study and helpful discussions, Mary Moore and Baijun Tian for valuable comments.

Chapter 5

This work is supported by NSF grants AGS-1062016 and AGS-1552385. Sincere thanks go to Nicholas Byrne for sharing analysis scripts and pointing out an important issue in an earlier draft of the manuscript that led us to realize the significance of using 6-hourly data. The authors thank Nicholas Byrne, Dennis Hartmann and Aditi Sheshadri for very constructive reviews and Martin Singh for discussions and comments on the manuscript.

Chapter 1

Introduction

The climate system is characterized by large-scale atmospheric variabilities at different spatial and temporal scales, in distinct regions and for various reasons. Understanding the dynamical mechanisms associated with these variabilities is not only scientifically intriguing *per se*, but also has important implications for weather prediction and for interpretation of climate projection. In particular, this work covers investigations of three dominant patterns of large-scale circulation variability in the atmosphere, namely the South Asian summer monsoon, the Madden-Julian Oscillation (MJO) and the annular mode. These patterns of large-scale variability have tremendous societal impacts, and a better understanding of the dynamical mechanisms of these variabilities is warranted.

The South Asian monsoon is essentially driven by the annual cycle of solar forcing, and features seasonal variations of winds and precipitation. The MJO dominates intraseasonal variability in the tropics, and is associated with complicated internal dynamics (see review by Zhang, 2005). The annular mode is a prominent pattern of the zonal mean variability at intraseasonal to interannual timescales, and has been interpreted as a forced-dissipative system (e.g., Lorenz and Hartmann, 2001). These phenomena are introduced in more detail in this chapter and in the beginning sections of Chapters 2-5.

This work emphasizes a combination of observational studies and numerical modeling. Guided by observations, numerical experiments are designed and conducted to pursue a

better theoretical understanding of the dynamical mechanisms governing these systems.

1.1 South Asian summer monsoon

The South Asian summer monsoon is a major feature of the general circulation of the Earth's atmosphere. The monsoon is characterized by seasonal variations of winds and precipitation, and affects the lives of billions of people (e.g., Lau *et al.*, 2006). Since the physical origin of the monsoons was first addressed by Halley (1686), the monsoons have been considered as a planetary-scale sea breeze caused by the thermal contrast between the land and ocean. In particular, the classic view holds that the Tibetan Plateau drives a strong South Asian summer monsoon as an elevated heat source (e.g., Yeh *et al.*, 1957; Li and Yanai, 1996). This idea appeared to be supported by numerical simulations (e.g., Hahn and Manabe, 1975; Prell and Kutzbach, 1992). The classic view of the role of the orography on the monsoon was challenged by new interpretations of observations with modern theories (see review by Boos, 2015). Under the framework of convective quasi-equilibrium, moist convection is a fast process that maintains the atmosphere to a state of quasi-equilibrium balance between convection and large-scale forcing, so that temperature nearly follows a moist adiabatic lapse rate in the troposphere above the cloud base (Emanuel *et al.*, 1994). As a result, the thermal forcing for the monsoon is uniquely related to the meridional distribution of the sub-cloud moist entropy (Emanuel, 1995). Reanalysis data shows that during the boreal summer, the sub-cloud moist entropy maximum collocate with the free-tropospheric temperature maximum south of the Himalayas, contradicting that the plateau serves as a heat source to the monsoon (e.g., Boos and Emanuel, 2009; Boos and Kuang, 2010). Also, the monsoon remains largely unchanged in numerical simulations by the removal of the Tibetan Plateau as long as the narrow range of Himalayas is preserved, suggesting the orography creates a strong monsoon mainly by insulating the thermal maximum from extratropical air (Boos and Kuang, 2010).

However, the resolution of the numerical simulations in the previous studies are too coarse to resolve topographic details in the regions of interest. For example, the narrow

range of the Himalayas is not distinct from the Tibetan Plateau in a climate model integrated at 2° horizontal resolution. In Chapter 2, the role of the orography on South Asian monsoon is comprehensively examined using state-of-the-art numerical modeling.

1.2 Madden-Julian Oscillation

Since the MJO, the dominant mode of intraseasonal variability in the tropics, was first discovered in the early 1970s (Madden and Julian, 1971), it has been extensively studied and well documented (see review by Zhang, 2005). The MJO features planetary-scale convective envelopes propagating eastward, primarily over the equatorial Indian and western/central Pacific oceans, at around 5 m s^{-1} . Under a recently proposed framework, the MJO is regarded as a moisture mode, where column-integrated moisture is the central prognostic variable. MJO's propagation is often viewed as the result of horizontal moisture advection, which has been argued to lead the column integrated moist static energy (hereafter column MSE) anomaly (e.g., Sobel and Maloney, 2013; Pritchard and Bretherton, 2014), and the growth and maintenance of the disturbance are often interpreted in the context of processes (e.g., wind-evaporation and radiative-convective feedbacks) recharging column MSE anomalies associated with the MJO (e.g., Andersen and Kuang, 2012; Sobel and Maloney, 2012). Meanwhile, it has been proposed that extratropical waves propagating into the tropics are important to MJO initiation, and circumnavigating waves caused by a preceding MJO event can trigger a successive MJO event (e.g., Ray and Li, 2013; Maloney and Wolding, 2015).

Failure of current GCMs to simulate a realistic MJO urges an improved understanding of the MJO initiation/propagation mechanisms. In Chapter 3, a mechanism-denial study is conducted to examine the importance of influences from extratropical and circumnavigating waves, wind-evaporation feedback and radiative-convective feedback to the MJO. In particular, time-invariant forcing and nudging are implemented to maintain the climatology in the experiments, so as to reduce the interference from mean state changes, which is a common issue in previous mechanism-denial studies (e.g., Ray and Li, 2013). Chapter 4 is focused on observational analysis, the vertical profile of the radiative heating anomaly associated with

the MJO is constructed using satellite products.

1.3 Annular mode

The variability of the zonal mean circulation of the atmosphere has been studied since almost 80 years ago (Rossby, 1939; Namias, 1950). With more reliable data available recently, there has been growing interest in the annular mode, a dominant mode of variability of the extratropical circulation in both hemispheres at intraseasonal to interannual timescales (Kidson, 1988; Thompson and Wallace, 1998; Gong and Wang, 1999; Thompson and Wallace, 2000). The annular mode features an equivalent barotropic dipolar structure of zonal mean zonal wind, and represents latitudinal shifts of the eddy-driven jet (Nigam, 1990; Hartmann and Lo, 1998; Thompson and Woodworth, 2014; Thompson and Li, 2015). A positive feedback between anomalous zonal flow and eddy fluxes has been argued to be responsible for the persistence of the annular mode. Quantifying the strength of the eddy-jet feedback is important for understanding both internal variability and response to external forcing. Statistical methods have been proposed to quantify the feedback strength (Lorenz and Hartmann, 2001; Simpson *et al.*, 2013). However, how well the statistical methods quantify the feedback has not been established. Furthermore, a recent study (Byrne *et al.*, 2016) has demonstrated the shortcomings of these statistical methods in distinguishing between an eddy feedback and an interannual variability that is external to any processes in the midlatitude troposphere (e.g., stratospheric variability). It is argued that previous evidence for the existence of a positive eddy .

In Chapter 5, a linear response function, which relates the temporal tendencies of zonal mean temperature and zonal wind to their anomalies and external forcing (Hassanzadeh and Kuang, 2016), is used to quantify the strength of the eddy-jet feedback associated with the annular mode in an idealized GCM. The statistical methods are evaluated against the results from the linear response function before they are applied to the reanalysis data.

Chapter 2

Effects of Orography and Surface Heat Fluxes on the South Asian Summer Monsoon ¹

Abstract

A high-resolution (40 km horizontal) global model is used to examine controls on the South Asian summer monsoon by orography and surface heat fluxes. In a series of integrations with altered topography and reduced surface heat fluxes, monsoon strength, as indicated by a vertical wind shear index, is highly correlated with the amplitude of the maximum boundary layer equivalent potential temperature (θ_{eb}) over South Asia. Removal of the Tibetan Plateau while preserving the Himalayas and adjacent mountain ranges has little effect on monsoon strength, and monsoon strength decreases approximately linearly as the height of the Himalayas is reduced. In terms of surface heat flux changes, monsoon strength is most sensitive to those in the location of the θ_{eb} maximum just south of the Himalayas. These results are consistent with the recent idea that topography creates a strong monsoon by insulating the thermal maximum from dry extratropical air. However,

¹Co-authored with William Boos and Zhiming Kuang

monsoon strength is found to be more sensitive to variations in the θ_{eb} maximum when topography is altered than when surface heat fluxes are reduced, and it is suggested that free tropospheric humidity changes lead to deviations from strict convective quasi-equilibrium and cause this difference. When topography is reduced, dry extratropical air intrudes into the troposphere over the θ_{eb} maximum and is entrained by local deep convection, requiring a higher θ_{eb} to achieve convective equilibrium with a given upper-tropospheric temperature and associated balanced monsoon flow. These results illustrate potential complexities that need to be included in simple theories for monsoon strength built on strict convective quasi-equilibrium.

2.1 Introduction

The boreal summer South Asian monsoon is a major feature of the general circulation of the Earth's atmosphere and affects the lives of billions of people (e.g., Lau *et al.*, 2006). The thermally direct monsoon circulation is caused by the thermodynamic contrast between the Eurasian Continent and the Indian Ocean. In particular, the Tibetan Plateau has for decades been thought to drive this large-scale monsoon by acting as an elevated heat source (Yeh *et al.*, 1957). The sensible heat flux from the surface of the Tibetan Plateau in spring was argued to heat air above the plateau to higher temperatures than air over surrounding non-elevated surfaces, leading to the reversal of the free-tropospheric meridional temperature gradient that accompanies the onset of the monsoon. The meridional temperature gradient would then be maintained through the summer by a combination of surface heat fluxes, the diabatic heating of precipitating convection that is caused by the plateau-induced ascent, and adiabatic warming by dynamically induced subsidence (e.g., He *et al.*, 1987; Yanai *et al.*, 1992; Wu and Zhang, 1998). The importance of elevated heating seemed to be supported by the fact that the intensity and northward extent of monsoon precipitation were greatly reduced in model simulations in which all topography was removed (e.g., Hahn and Manabe, 1975; Prell and Kutzbach, 1992). Temporal correlations between Tibetan Plateau uplift and some proxy indicators of monsoon strength seem to support the idea that elevated topography

creates a strong monsoon (e.g., An *et al.*, 2001), but there is considerable uncertainty in the timing of orographic uplift and in the interpretation of proxies for monsoon strength (see review by Molnar *et al.*, 2010).

While Asian topography is clearly needed to produce a strong monsoon circulation, the roles of the broad Tibetan Plateau and the comparatively narrow mountain ranges adjacent to the plateau (e.g., the Himalayas) were not distinguished in many previous modeling studies (e.g., Abe *et al.*, 2003; Yasunari *et al.*, 2006). As reproduced in Figure 2.1A, modern observations (e.g., Boos and Emanuel, 2009) show that the maximum free tropospheric temperature is centered slightly south of the peaks of the Himalayas (the thick white curve in Figure 2.1A) instead of being centered over or to the northwest of the Tibetan Plateau as one would expect for the response to a heat source (e.g., Gill, 1980). The free tropospheric temperature maximum lies almost directly over the maximum boundary layer equivalent potential temperature (θ_{eb} ; Figure 2.1B), consistent with convective quasi-equilibrium treatments of precipitating large-scale flow as discussed in Boos and Emanuel (2009), and the maximum θ_{eb} is located over the non-elevated region of northern India. These facts, together with the existence of sharp horizontal gradients in θ_{eb} coincident with the Himalayas and adjacent mountain ranges, led Boos and Kuang (2010) to hypothesize that topography creates a strong monsoon primarily by insulating the monsoon thermal maximum from the low θ_{eb} (i.e., dry) air of the Asian continental interior (see also Chakraborty *et al.*, 2006). They confirmed that the monsoon circulation is largely unchanged by removal of the Tibetan Plateau in a climate model as long as the Himalayas and adjacent mountain ranges are preserved. These model results and observations of θ_{eb} are consistent with the idea that the elevated heating over the Tibetan Plateau is not crucial to the monsoon, but the radiative and surface heat fluxes over the non-elevated parts of northern India are important. Wu *et al.* (2012) subsequently argued that the surface sensible heat flux from the southern slopes of the Himalayas provides an elevated heating that drives a large part of the monsoon, and showed that monsoon strength decreased when sensible heating from these mountain ranges was suppressed in a climate model. However, additional model simulations showed

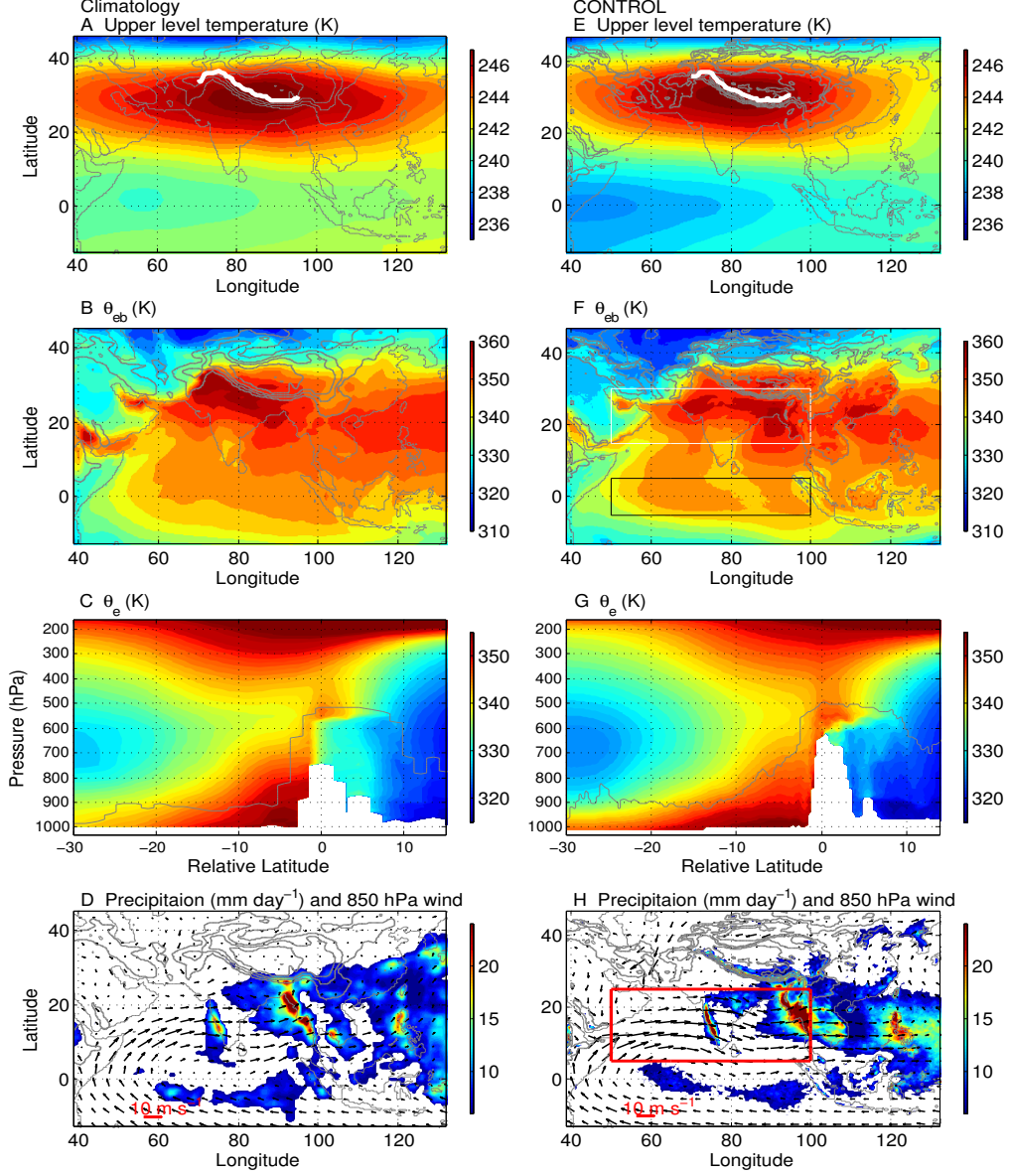


Figure 2.1: The thermodynamic structure, precipitation and wind from observations, reanalysis data and the CONTROL. (A) ERA-40 temperature averaged between 175-450 hPa. (B) ERA-40 θ_{eb} : θ_e about 20 hPa above the surface. (C) Vertical-meridional distributions of the θ_e from the ERA-40 averaged between 70°E-95°E along the lines at the same relative latitude with respect to the peaks of the Himalayas (indicated by the thick white curve in A). (D) TRMM precipitation rate (color shading) and ERA-40 850 hPa winds (vectors). The right column (EFGH) shows the corresponding properties of averages of ensemble members from the CONTROL experiment. In F, the white box denotes the domain in which regions covering $3.7 \times 10^6 \text{ km}^2$ of the highest θ_{eb} are identified to calculate the maximum θ_{eb} over northern India. The black box indicates the domain in the Equatorial Indian Ocean where the reference θ_e^* is averaged over for $\Delta\theta_{ec}$. In ABDEFH, the grey contours denote elevations with the interval of 1200 m. In CG, the grey curve shows the maximum height of the orography along the relative latitude, so that below the grey curve, along each relative latitude there are different numbers of invalid data points that are not considered into the average. In H, the red box defines the region to calculate the mWYI.

that the monsoon is more sensitive to heat fluxes from non-elevated surfaces over northern India than it is to heat fluxes from the Himalayas and other elevated terrain (Boos and Kuang, 2013). Thus, surface heat fluxes in the region of the θ_{eb} maximum seem to be most important for monsoon strength, with topography creating a strong monsoon primarily by suppressing the horizontal advective flux of low equivalent potential temperature (θ_e) air into the thermal maximum.

However, all of the studies discussed above used models with coarse resolution that barely resolve topographic details in the regions of interest. For example, the narrow range of the Himalayas is not distinct from the Tibetan Plateau in a climate model integrated at 2° horizontal resolution. Cane (2010) noted the need for results concerning the role of topography in the South Asian summer monsoon to be reproduced in higher resolution models. Boos and Hurley (2013) found that a collection of the latest generation of climate models has a negative bias in the strength of the monsoon thermal maximum that seems to be caused by an overly strong flow of dry air across the smoothed model topography. With these motivations, here we employ the Weather Research and Forecast (WRF) Model as a high resolution general circulation model to explore the effects of orography and surface heat fluxes on the South Asian summer monsoon. This model is integrated at 40 km horizontal resolution, substantially finer than the roughly 200 km resolution employed by Boos and Kuang (2010) or the wavenumber 42 rhomboidal truncation used in the spectral model of Wu *et al.* (2012). Furthermore, we conducted a fairly large number of model experiments in which topographic heights and surface heat fluxes were altered. The results provide insight into the relative importance of topography and regional surface heat fluxes in setting the monsoon strength.

2.2 Model and methods

Using WRF Version 3, eleven sets of global experiments were conducted. All integrations were performed with the horizontal resolution of 40 km and 40 vertical levels with prescribed sea surface temperature and sea ice. Convection is explicitly represented in the

model using the Reduced Acceleration in the VERTICAL (RAVE) methodology of Kuang *et al.* (2005), with a RAVE factor of 10. This method rescales convective motions and large-scale circulations, and allows global integrations at coarser resolutions with explicit (rather than parameterized) convection. The Noah Land-Surface Model was used over land. When the topography was modified, only the surface elevations were changed, and all other fixed properties of the land, such as soil temperature at the lower boundary of the land surface model, were left unchanged. A sensible heat sink was prescribed in the land-surface scheme in the experiments with reduced surface sensible heat fluxes. All runs were started in late February or early March using initial conditions from the National Centers for Environmental Prediction reanalysis data, and time averages were taken and analyzed in June, July and August.

Table 2.1 provides a brief summary of the experiments design. With no modification of the surface heat fluxes, the standard WRF topography (the thin grey contours in Figure 2.1E) is used in the control simulations, referred to as CONTROL. The orography is modified in HIM90, HIM66, HIM33 and FLAT, and each experiment with altered orography consists of an ensemble of three simulations, integrated globally from February 27, March 1, and March 3 to September 1, 1999. For HIM90, the surface elevations are first set to zero north of the point at which the Himalayas reach 90% of the elevation of the highest point at each longitude between 70°E and 100°E, so that the bulk of the Tibetan Plateau is removed while the narrow range of the Himalayas is mostly preserved. Then a poleward slope of 10 m km⁻¹ is applied north of the point with the highest elevation to avoid numerical instability. The thin grey contours in Figure 2.2A denote the topography implemented in HIM90. We did not keep 100% of the maximum height at each longitude because the highest point is located north of the Himalayas at some longitudes. HIM66 and HIM33 are configured similarly as in HIM90, except that the Himalayas are truncated at 66% and 33% of the maximum height at each longitude, respectively. The topography for these two experiments is illustrated in Figures 2.2BC. In FLAT, the elevations are set to zero north of 20°N and between 60°E to 120°E as shown in Figure 2.2D.

Table 2.1: Experiments configuration. The elevations of the altered orography in HIM90, HIM66, HIM33 and FLAT are denoted by the thin grey contours in Figures 2.2ABCD with interval of 1200 m. A sensible heat sink of 150 W m^{-2} is prescribed in the land-surface scheme in the first group of experiments with reduced surface sensible heat fluxes. In the second group of experiments with reduced surface sensible heat fluxes, the magnitude of surface sensible heat fluxes forcing follows the distribution of differences between θ_{eb} values for the FLAT experiment and those for the CONTROL experiment. TIBET includes the part of the Tibetan Plateau north of the Himalayas as denoted by the thick black contour in Figure 2.2E. HIM (thick black contour in Figure 2.2F) is defined as the region above 1200 m on the southern slope of the Himalayas, 70°E - 100°E , and covers $7.6 \times 10^5 \text{ km}^2$. INDIA (thick black contour in Figure 2.2G) covers the same areal extent as HIM, and is directly south of and adjacent to the HIM. INDIA2 (thick black contour in Figure 2.2H) is defined as the region with the highest θ_{eb} in the CONTROL covering $7.6 \times 10^5 \text{ km}^2$. THERM (thick black contour in Figure 2.6A) is the region south of the Himalayas, north to 22.5°N , 67°E - 90°E .

variation in input		note
CONTROL		n/a
altered orography		
HIM90	Tibetan Plateau removed; 90% of Himalayas preserved	Figure 2.2A
HIM66	Tibetan Plateau removed; 66% of Himalayas preserved	Figure 2.2B
HIM33	Tibetan Plateau removed; 33% of Himalayas preserved	Figure 2.2C
FLAT	elevation set to 0 north to 20°N , 60°E - 120°E	Figure 2.2D
sensible heat sink (1st group)		
TIBET	344 TW in TIBET (over the Tibetan Plateau)	Figure 2.2E
HIM	114 TW in HIM (over southern slope of the Himalayas)	Figure 2.2F
INDIA	114 TW in INDIA (over northern India)	Figure 2.2G
INDIA2	114 TW in INDIA2 (over northern India)	Figure 2.2H
sensible heat sink (2nd group)		
THERM1	196 TW in THERM (over northern India)	Figure 2.6A
THERM2	392 TW in THERM (over northern India)	Figure 2.6A
THERM3	588 TW in THERM (over northern India)	Figure 2.6A

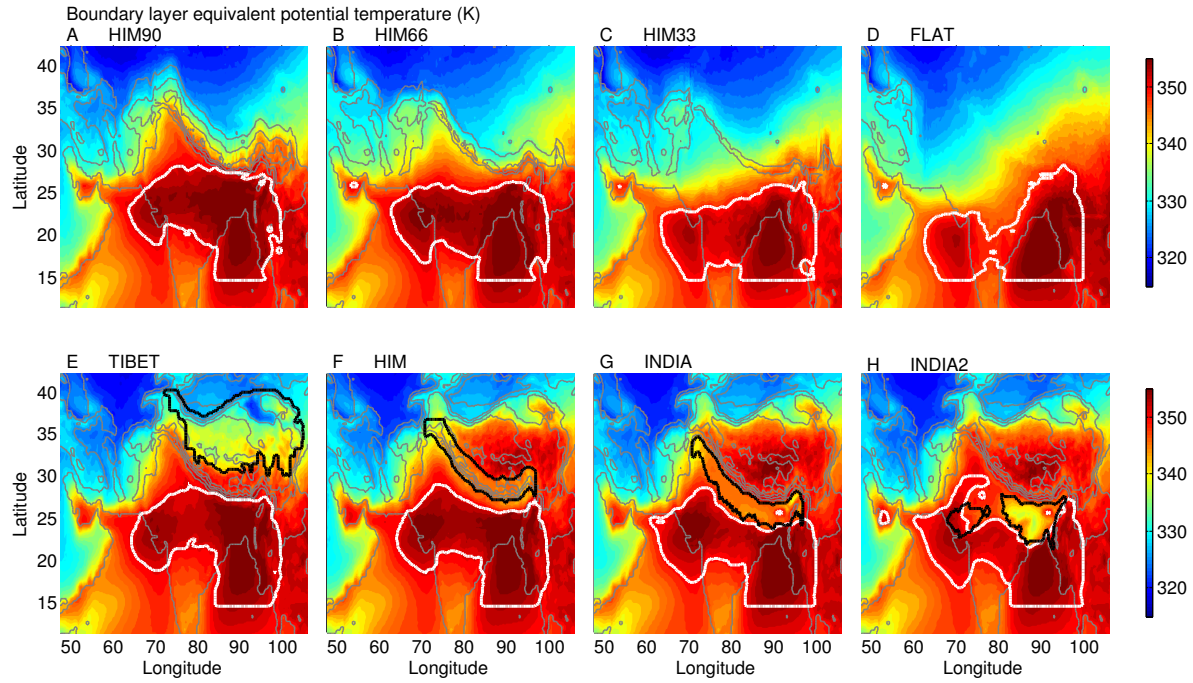


Figure 2.2: The spatial distribution of θ_{eb} averaged for June, July and August (color shading). The thick white contours denote the regions covering $3.7 \times 10^6 \text{ km}^2$ of the highest θ_{eb} within 50°E - 100°E , 15°N - 30°N . The thin grey contours denote elevations with the interval of 1200 m. In the lower panels, the thick black contours show the regions where a sensible heat sink is applied on the surface.

After the surface fluxes are calculated in the land-surface scheme at each time step, a sensible heat sink of 150 W m^{-2} is applied to the bottom layer of the atmosphere over a series of target regions in the first group of experiments with reduced surface heat fluxes (i.e., TIBET, HIM, INDIA and INDIA2). To improve the signal-to-noise ratio, the CONTROL, TIBET, HIM, INDIA and INDIA2 experiments include ten integrations, each starting from an individual date from February 24 through March 5, 1999. TIBET covers the regions with elevations higher than 1200 m north of the Himalayas between 70°E and 100°E (denoted by the thick black contour in Figure 2.2E), and the total reduction of surface sensible heat flux is 344 TW in the TIBET experiment. HIM is defined as the region above 1200 m on the southern slope of the Himalayas, between 70°E and 100°E , and covers around $7.6 \times 10^5 \text{ km}^2$ (thick black contour in Figure 2.2F). INDIA is the region covering the area of $7.6 \times 10^5 \text{ km}^2$, the same as HIM, and is south of and adjacent to HIM (thick black contour in Figure 2.2G). INDIA2 (thick black contour in Figure 2.2H) also covers $7.6 \times 10^5 \text{ km}^2$, but it consists of the regions with the highest θ_{eb} in the CONTROL. The total forcing of surface sensible heat fluxes in HIM, INDIA and INDIA2 is 114 TW. We also conduct a second group of experiments with modified surface sensible heat fluxes. In THERM1, the amplitude of the surface heat flux forcing follows the distribution of differences between θ_{eb} values for the FLAT experiment and those for the CONTROL experiment, and the sensible heat flux is reduced over the region north of 22.5°N and south of the Himalayas between 67°E and 92°E (thick black contour in Figure 2.6A). In total, 196 TW of surface sensible heat fluxes is eliminated in THERM1. Then in THERM2 and THERM3, the remaining surface sensible heat flux forcing is doubled and tripled, respectively. For THERM1, THERM2 and THERM3, the second group of experiments with reduced surface heat fluxes, four integrations are conducted in each experiment starting from February 37, March 1, March 2 and March 3.

The strength of the monsoon is quantified using an index based on the spatially averaged vertical wind shear (Webster and Yang, 2012). To better represent the dominant mode of interannual variations of the South Asian summer monsoon, instead of using the original definition of the Webster-Yang Index, we followed Wang *et al.* (2001) and used the modified

Webster-Yang Index (mWYI). This mWYI is defined as the difference in zonal wind between 200 and 850 hPa, averaged from 5°N to 25°N, 50°E to 100°E (indicated by the red box in Figure 2.1H). We also tried the Somali Jet index defined by Boos and Emanuel (2009) to indicate the strength of the monsoon: the fact that the Somali Jet index produced similar results as those from the mWYI suggests that our results are not highly sensitive to the choice of index.

2.3 Results and discussions

With realistic topography, the CONTROL runs produce similar precipitation to that estimated from the Tropical Rainfall Measuring Mission (TRMM) 3B43V6 data averaged for June, July and August, 1999 (Figures 2.1DH). The precipitation maxima are located off the Western Ghats in India, over the southern slope of the Himalayas and the coastal mountains of Myanmar. The precipitation peaks at around 24 mm day^{-1} , similar to the observations. The simulated 850 hPa winds capture the main pattern of the large-scale circulation represented in European Centre for Medium-Range Weather Forecasts 40 Year Reanalysis (ERA-40) data averaged for the same period. There is strong westerly flow over the North Indian Ocean and the Indian subcontinent. The modeled θ_{eb} (Figure 2.1F) and upper tropospheric temperature (Figure 2.1E) generally agree with the ERA-40 data (Figures 2.1AB), with the θ_{eb} maximum positioned in North India and the center of maximum upper tropospheric temperature located slightly south of the peaks of the narrow range of mountains (the thick white curve in Figure 2.1E). Although the model results show some bias compared to the observationally based estimates, such as overly strong low-level westerlies and a θ_{eb} maximum that is slightly weaker and positioned too far south, the climatology produced by the WRF model is substantially better than that produced by almost all global climate models previously used to study the boreal summer South Asian monsoon (e.g., Boos and Kuang, 2010; Wu *et al.*, 2012; Boos and Hurley, 2013).

The vertical cross-section of the θ_e profile from the CONTROL experiment (Figure 2.1G), averaged between 70°E-95°E in relative distance to the peaks of the Himalayas at that

longitude, is also consistent, in spite of different resolutions, with that derived from the ERA-40 data (Figure 2.1C). The grey curves in Figures 2.1CG define the maximum elevation along each relative latitude, with 0° in relative latitude representing the location of the Himalayan peaks (the thick white curves in Figures 2.1AE). The sharp gradient in θ_{eb} is consistent with the hypothesis that the Himalayas insulate the θ_{eb} maximum against the low θ_e air in the north. A rough scale for the anomalous horizontal moist static energy flux divergence in the experiments where the topography is eliminated can be estimated by $\left\langle v \frac{\partial h}{\partial y} \right\rangle$, where v , h , and y are the anomalous meridional velocity, the basic state moist static energy, and the meridional distance, respectively, and angle brackets denote a mass-weighted vertical integral. An estimate of the moist static energy gradient can be obtained from the θ_e field using $\frac{\partial h}{\partial y} \approx \frac{c_{pd} T}{\theta_e} \frac{\partial \theta_e}{\partial y}$, in which c_{pd} is the heat capacity for dry air and T is the temperature. Assuming the scale for v is 1 m s^{-1} , and using a rough scale for $\frac{\partial \theta_e}{\partial y}$ from the observations, the anomalous horizontal moist static energy flux divergence is around 150 W m^{-2} . The scale for the anomalous moist static energy flux divergence in the experiments with altered orography is comparable with the imposed surface heat flux forcing in the experiments with reduced sensible heat fluxes, so we expect the response of the monsoon to share the same order of magnitude in the experiments with altered orography and reduced sensible heat fluxes.

The ten integrations in CONTROL yield an average mWYI of $35.7 \pm 0.28 \text{ m s}^{-1}$, with the error of the mean estimated assuming a Gaussian distribution of error. Using three-month means for June, July and August, we regress the mWYI on θ_{eb} at each horizontal location for the ten integrations of the CONTROL experiment, which are analogues for ten different monsoon seasons. As shown in Figure 2.3, the mWYI is most strongly correlated with θ_{eb} in North India, very near the θ_{eb} maximum. The regression coefficients indicate the pattern of θ_{eb} anomaly in a year with strong monsoon circulation, and the contrast of regression coefficients between North India and the Equatorial Indian Ocean shows that a stronger monsoon circulation is accompanied by a stronger meridional θ_{eb} gradient. The positive correlation over the Indian Ocean does not result from any local changes in sea

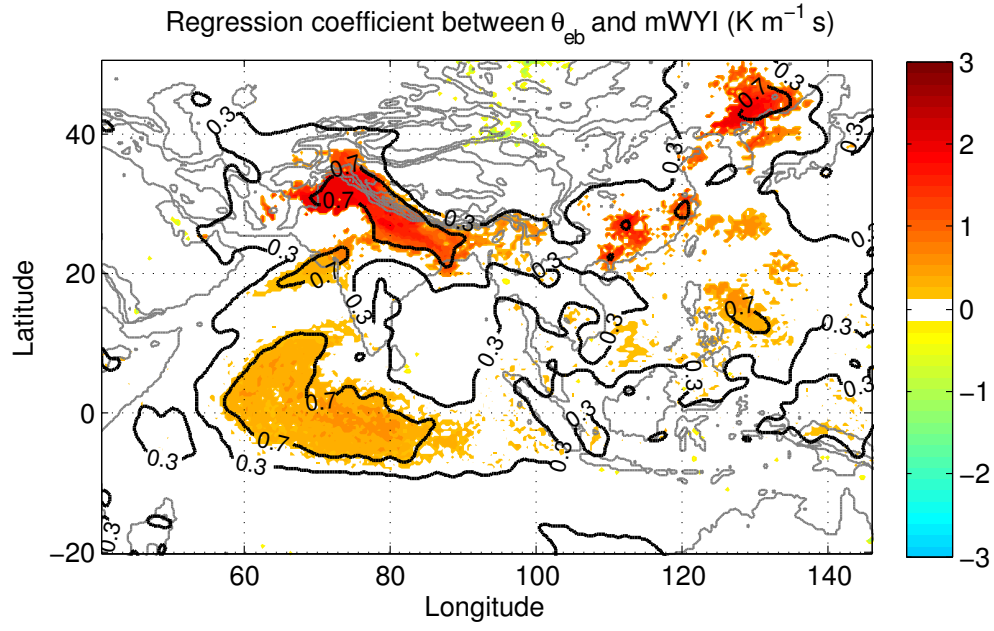


Figure 2.3: Spatial distribution of the regression coefficient between the θ_{eb} and the mWYI from the CONTROL. Color shading represents the regression coefficients ($\text{K m}^{-1} \text{s}$) that are statistically significant at 95% confidence level. The thick black contours indicate regions with correlation coefficients of 0.3 and 0.7. The thin grey contours denote elevations with interval of 1200 m.

surface temperature because sea surface temperature does not vary between the runs, so we conclude that it results from increased θ_{eb} due to intensified circulation. The positive signal in the East Asian marginal seas agrees with the results from the composite analysis by Wang *et al.* (2001), and was attributed to teleconnections with the surface warming associated with an anomalous anticyclone. The regression pattern for our model is similar to that calculated from 45 years of interannual variations in observed monsoon precipitation and θ_{eb} (Hurley and Boos, 2013, their Figure 2b).

When all orography is removed within 60°E-120°E, 20°N-90°N in the FLAT experiment, the monsoon circulation weakens greatly as in previous studies (e.g., Chakraborty *et al.*, 2002), and the mWYI drops to around 23 m s⁻¹ (Figure 2.4A). Precipitation over North India drops by more than 70% compared to the CONTROL, and the Somali Jet decreases by around 4 m s⁻¹ from 12.3 m s⁻¹ in the CONTROL. Also, the free tropospheric temperature peak south of the Himalayas decreases in amplitude and shifts equatorward, and the θ_{eb} peak drops by around 2.5 K and moves southwards to the Bay of Bengal (Figure 2.2D). The fine resolution of this model allows a more careful look at how the monsoon strength changes when topography is modified. Results from the HIM90 experiment show that the mWYI slightly decreases, by less than 4 m s⁻¹, compared to the CONTROL experiment. Then the monsoon circulation gradually weakens as the peaks of the Himalayas further decrease to 66% and 33% of their height in CONTROL (Figure 2.4A). These experiments confirm the conclusion by Boos and Kuang (2010) that the presence of the Tibetan Plateau is not required for the existence of a strong monsoon, and that the monsoon weakens as the elevation of the Himalayas decreases. The decrease of the monsoon strength is approximately linear with the decrease in the maximum elevation of the insulation with no threshold behavior observed. TIBET, HIM, INDIA, and INDIA2 are then conducted with realistic topography but reduced surface sensible heat fluxes. Because the internal variability of the mWYI grows in this group of experiments, the number of integrations for each experiment is increased to ten to improve the signal-to-noise ratio. There is a clear dependence of the mWYI on the surface heat flux forcing whether the forcing is over elevated terrain or not. A sensible heat

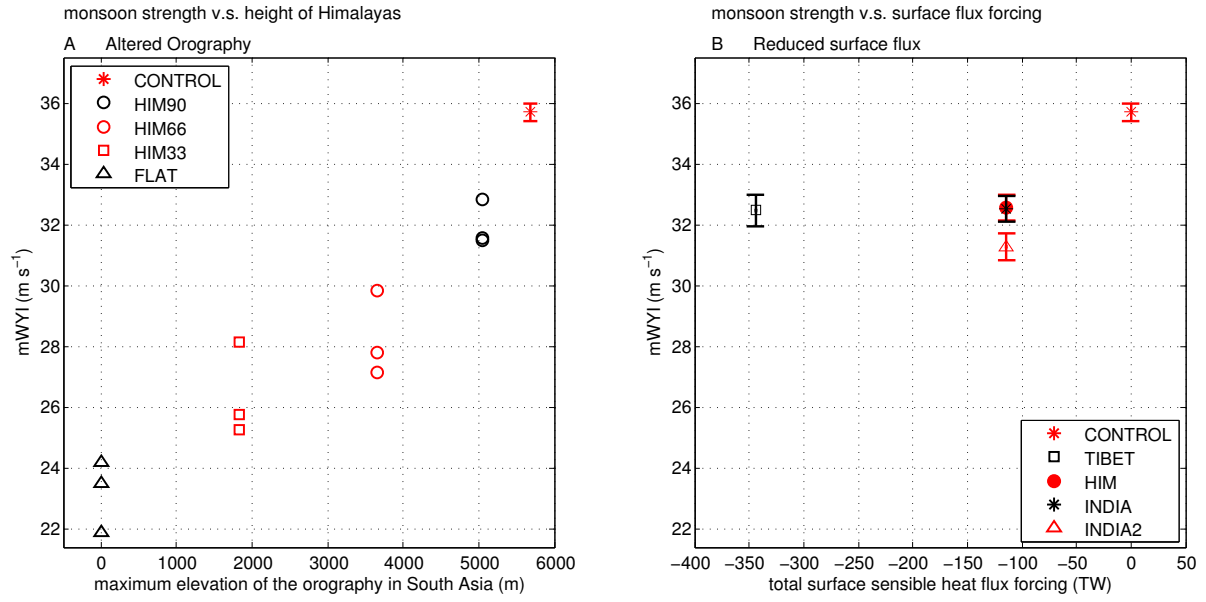


Figure 2.4: The monsoon strength plotted against the maximum elevation of the orography in South Asia in the experiments with altered orography (A), and against total surface sensible heat flux forcing in the experiment with sensible heat sink (B). The averaged mWYI of 10 ensemble members is shown with error bars for CONTROL, TIBET, HIM, INDIA and INDIA2; the data from individual simulations is plotted for HIM90, HIM66, HIM33 and FLAT, because there are only three ensemble members for each of these experiments.

sink of 150 W m^{-2} over INDIA2 decreases the mWYI by around 4.5 m s^{-1} , while the mWYI goes down by around 3 m s^{-1} when sensible heat sinks with the same magnitude per unit area are implemented over TIBET, HIM and INDIA (Figure 2.4B). Given the areal extent with reduced surface heat fluxes in different experiments, the monsoon is most sensitive to the forcing in INDIA2 (the non-elevated region in the location of the θ_{eb} maximum) and least sensitive to that in TIBET, which is more extensive than HIM, INDIA and INDIA2.

Figure 2.2 shows the spatial distribution of the θ_{eb} in the experiments with orographic and surface heat flux forcing, as it was suggested that the θ_{eb} maximum in North India is closely associated with the monsoon strength. It should be noted that, though the surface heat fluxes do change when the orography is reduced, the surface heat fluxes anomaly in the experiments with altered orography is very small compared to that from the experiments with reduced surface sensible heat flux. As a result, the θ_e anomalies in HIM90, HIM66, HIM33 and FLAT can mainly be considered as results from increased mixing between the high θ_e air south of the Himalayas and the dry air north of the topographic barrier. In the experiments with altered orography, the dry air from the north penetrates into North India. As the maximum height of the Himalayas is reduced, the θ_{eb} over the Tibetan Plateau and North India decreases gradually, and the regions with the highest θ_{eb} shift southwards (Figures 2.2ABCD). For the first group of experiments with reduced surface sensible heat fluxes (Figures 2.2EFGH), significant negative θ_{eb} anomalies can be seen in the regions where the sensible heat sink is implemented (denoted by the thick black contours), and the regions with the highest θ_{eb} vary accordingly. The mWYI is most sensitive to the surface forcing in INDIA2 because the corresponding θ_{eb} perturbation is coincident with the region with maximum θ_{eb} in the Control.

Figure 2.5 provides more insight into the thermal controls of the system. Since the strength of the monsoon is determined by horizontal thermal contrasts, the mWYI is plotted against an index, hereafter referred to as $\Delta\theta_{ec}$, representing the thermal contrast between South Asia and the Equatorial Indian Ocean. We define $\Delta\theta_{ec}$ as the difference between a measure of the maximum θ_{eb} over South Asia and the average saturated equivalent potential

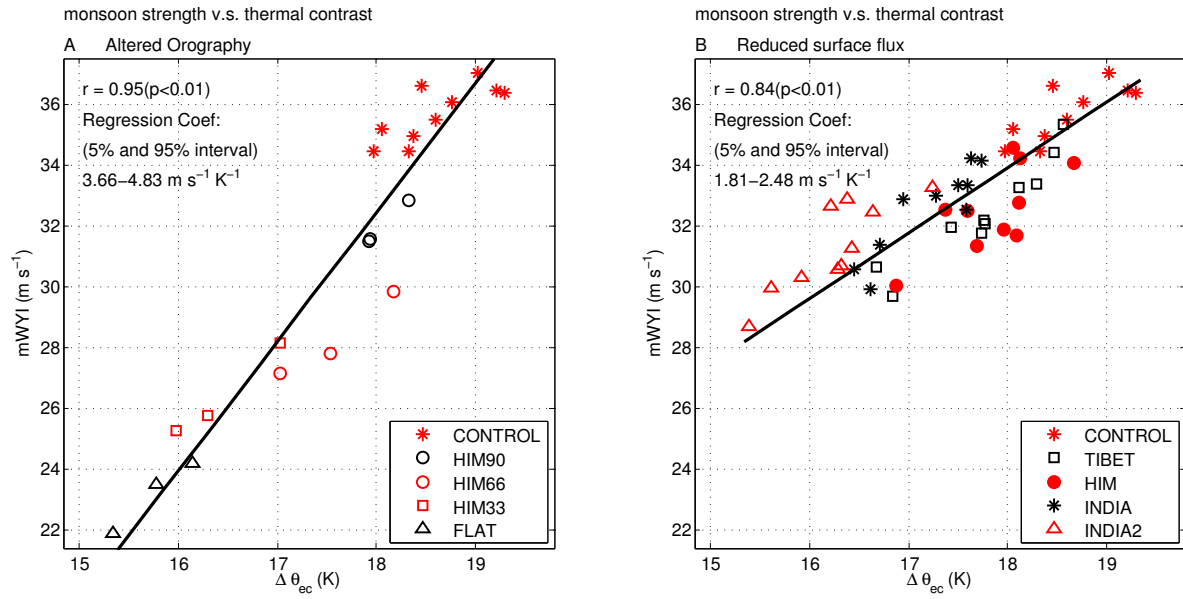


Figure 2.5: The monsoon strength (indicated by $mWYI$) regressed against $\Delta\theta_{ec}$ (i.e., the difference between the maximum θ_{eb} over South Asia and the average free tropospheric θ_e^* over the Equatorial Indian Ocean) in the experiments with altered orography (A), and reduced surface sensible heat fluxes (B). Each marker stands for an individual ensemble member, and the black line denotes the regression line.

temperature (θ_e^*) in the free troposphere over the Equatorial Indian Ocean. In practice, regions covering $3.7 \times 10^6 \text{ km}^2$ of the highest θ_{eb} within 50°E - 100°E , 15°N - 30°N (the white box in Figure 2.1F) are first identified for each experiment, and the maximum θ_{eb} is then calculated as the average over these regions (indicated by the thick white contours in Figure 2.2 and Figure 2.6A). The θ_e^* is averaged horizontally over 50°E - 100°E , 5°S - 5°N (the black box in Figure 2.1F), and vertically from 175 to 450 hPa. As expected, the mWYI is highly correlated with $\Delta\theta_{ec}$ for both the experiments with altered orography and reduced surface heat fluxes, with the correlation coefficient of 0.95 and 0.84, respectively (both significant at 99% confidence level). Although $\Delta\theta_{ec}$ was defined in this particular way to give a measure of thermal contrast that is related to the vertical shear through thermal wind balance, the variability of the averaged free tropospheric θ_e^* over the Equatorial Indian Ocean is quite small among different experiments. The maximum θ_{eb} averaged over the northern region thus dominates the variability of the thermal contrast, so the maximum θ_{eb} alone also has high correlation with the mWYI.

The regression coefficients are estimated assuming the error variance on each axis is proportional to the variance of the corresponding variable. For the experiments with altered orography, the slope is $4.25 \text{ m s}^{-1} \text{ K}^{-1}$, with the 95% confidence interval spanning 3.66 to $4.83 \text{ m s}^{-1} \text{ K}^{-1}$. In contrast, for the experiments with reduced surface heat fluxes, the estimated slope is $2.15 \text{ m s}^{-1} \text{ K}^{-1}$ with a 95% confidence interval of 1.81 to $2.48 \text{ m s}^{-1} \text{ K}^{-1}$. The difference in the regression coefficients is discussed in the next few paragraphs.

Recall that from Figure 2.2, the pattern of the θ_{eb} in response to orographic forcing differs from the structure of the θ_{eb} in the experiments with reduced surface heat fluxes, and these differences could contribute to the difference in the regression coefficients between the two groups of experiments seen in Figure 2.5. To clarify this issue, a second group of experiments with reduced surface sensible heat fluxes is conducted, in which the pattern of the surface flux forcing mimics the pattern of the θ_{eb} difference between the FLAT and CONTROL experiments. Taking the THERM1 experiment as an example, Figure 2.6A shows that the second group of experiments with reduced surface heat fluxes yields a similar

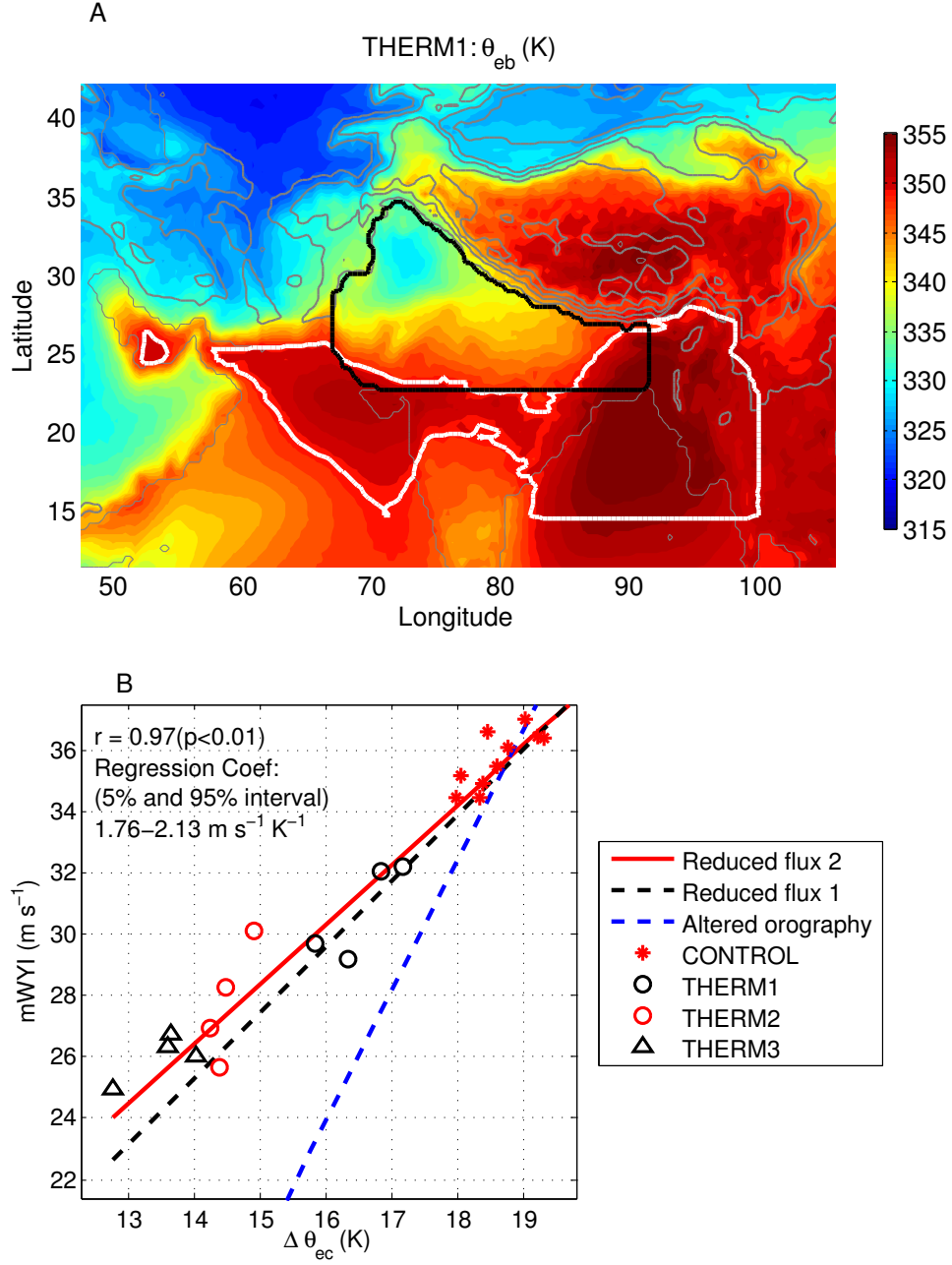


Figure 2.6: (A) Same as Figure 2.2, but for the THERM1 experiment. (B) Same as Figure 2.5, but for the second group of experiments with reduced surface heat fluxes. Each marker stands for an individual integration from CONTROL, THERM1, THERM2 and THERM3, and the red solid line denotes the regression line for these simulations. As reference, the black dashed line is the same as the regression line in Figure 2.5B for the first group of experiments with reduced sensible heat fluxes, and the blue dashed line is the same as the regression line in Figure 2.5A for the experiments with altered orography.

structure of θ_{eb} as in the FLAT experiment (Figure 2.2D), with the exception of the plateau region in which no heat flux anomalies were prescribed. The indices for monsoon strength and thermal contrast (i.e., mWYI and $\Delta\theta_{ec}$) from the second group of experiments with reduced surface heat fluxes are then regressed and presented in Figure 2.6B. The regression line for the second group of experiments with reduced surface heat fluxes shows little difference from that for the first group. The difference in the regression coefficients between the experiments with altered orography and reduced surface heat fluxes is thus robust, and this finding motivates further examination of why altered orography produces a larger change in monsoon strength for a given perturbation in thermal contrast as measured by $\Delta\theta_{ec}$.

Because the perturbation to the saturation equivalent potential temperature (θ_e^*) is much smaller than the mean value of θ_e^* , the mWYI is approximately proportional to the free-tropospheric meridional θ_e^* gradient according to the thermal wind relationship. In Figures 2.7AB the mWYI is regressed against free tropospheric θ_e^* difference between South Asia and the Equatorial Indian Ocean, with θ_e^* in South Asia averaged over the regions covering $3.7 \times 10^6 \text{ km}^2$ of the highest θ_{eb} as the thick white contours in Figure 2.2 indicate. The very high correlations seen in Figures 2.7AB, as expected, confirm the accuracy of this approximate thermal wind relationship. The regression coefficients are indistinguishable between the experiments with altered orography and those with reduced surface heat fluxes. Thus, the difference in the slopes between Figure 2.5A and Figure 2.5B has to come from the coupling between the θ_{eb} and free tropospheric θ_e^* . Without altering the orography, the values of the θ_{eb} anomalies are roughly the same as those of the θ_e^* anomalies (Figure 2.7D), which suggests that θ_e^* is closely coupled to θ_{eb} as in strict convective quasi-equilibrium. However, in the experiments with altered orography, the regressed line in Figure 2.7C deviates from the identity line, and we suggest that this is because dry air from the north makes the entire troposphere less moist in the region of the θ_{eb} maximum. The effect of the reduced Himalayas on the humidity is clearly seen in Figures 2.7EF where the anomalous relative humidity between 400 to 700 hPa is regressed against the θ_{eb} anomalies: the relative

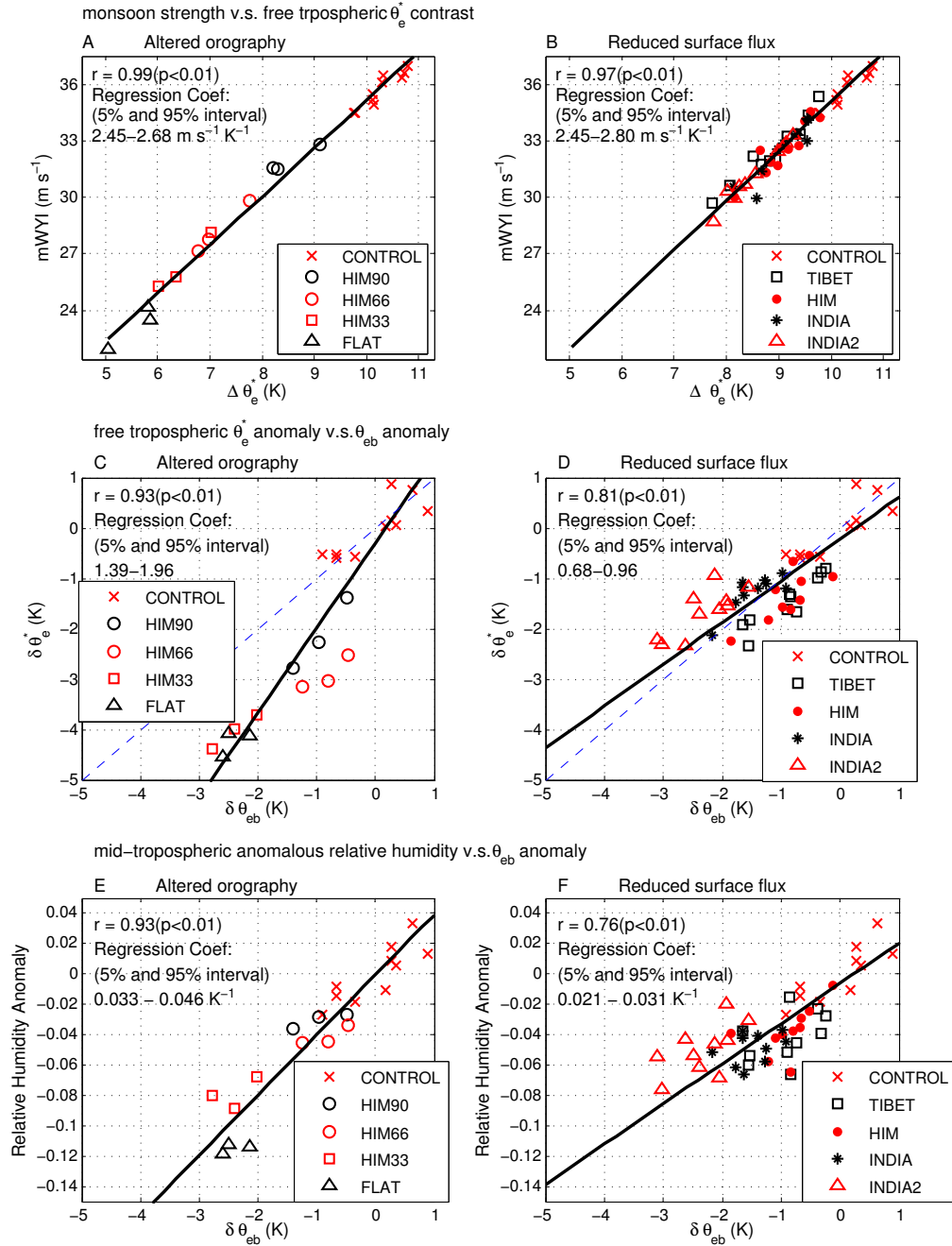


Figure 2.7: (AB) Same as Figure 2.5, but the mWYI is regressed against the difference of between the free tropospheric θ_e^* averaged over the regions covering $3.7 \times 10^6 \text{ km}^2$ of the highest θ_{eb} and the average free tropospheric θ_e^* over the Equatorial Indian Ocean. (CD) Same as AB, but θ_e^* anomalies averaged over the regions covering $3.7 \times 10^6 \text{ km}^2$ of the highest θ_{eb} are plotted against θ_{eb} anomalies averaged in the same region. The dashed blue lines indicate the identity line. (EF) Same as CD, but the anomalous relative humidity between 400 and 700 hPa is plotted against θ_{eb} anomalies averaged over the regions covering $3.7 \times 10^6 \text{ km}^2$ of the highest θ_{eb} .

humidity drops by 0.026 K^{-1} in response to surface fluxes forcing (Figure 2.7F), while it drops by 0.040 K^{-1} in response to altered orography (Figure 2.7E). Figure 2.8 provides cross-sections of relative humidity averaged between 70°E - 95°E in relative distance to the highest elevation at that longitude. The orography creates a sharp gradient of relative humidity across the high mountains in the CONTROL (Figure 2.8A). As the elevated orography is reduced, the troposphere becomes drier south of the Himalayas compared to the CONTROL (Figures 2.8BCDE). In contrast, in the experiments with reduced surface sensible heat fluxes, there are no significant changes in relative humidity in the free troposphere (Figures 2.8FGHI).

With a drier free troposphere, convective updrafts experience more severe loss of buoyancy from entrainment, and require a more unstable stratification to balance the same large-scale forcing that generates convective instability. The realized convective quasi-equilibrium thus deviates from a strict quasi-equilibrium, in which θ_e^* anomalies are roughly equal to θ_{eb} anomalies (e.g., Emanuel *et al.*, 1994). As a result, the free tropospheric θ_e^* over the northern region decreases more than θ_{eb} in the altered orography runs, leading to a greater reduction in monsoon strength for a given decrease in θ_{eb} . The fact that deviations from strict quasi-equilibrium can be important to the strength of the monsoon indicates the existence of complexity beyond that assumed in previous simple theories of the monsoon that are built upon strict quasi-equilibrium (e.g., Emanuel, 1995; Chou and Neelin, 2003).

This article focuses on the main monsoon season only, but how the orography and surface heat fluxes affect the monsoon before and after the mature phase is also of scientific interest. Some previous studies suggested that latent and sensible heat fluxes over the elevated surface are significant to the timing of monsoon onset (e.g., Wu and Zhang, 1998). On the other hand, Chakraborty *et al.* (2006) found evidence that monsoon onset requires surface moist static energy higher than a threshold value over India, and they linked the timing of monsoon onset to the West Himalayan orography as it blocks the cold extratropical air from entering northern India. More recent research has drawn attention to the importance of mechanically induced downstream convergence to the monsoon onset (e.g., Park *et al.*,

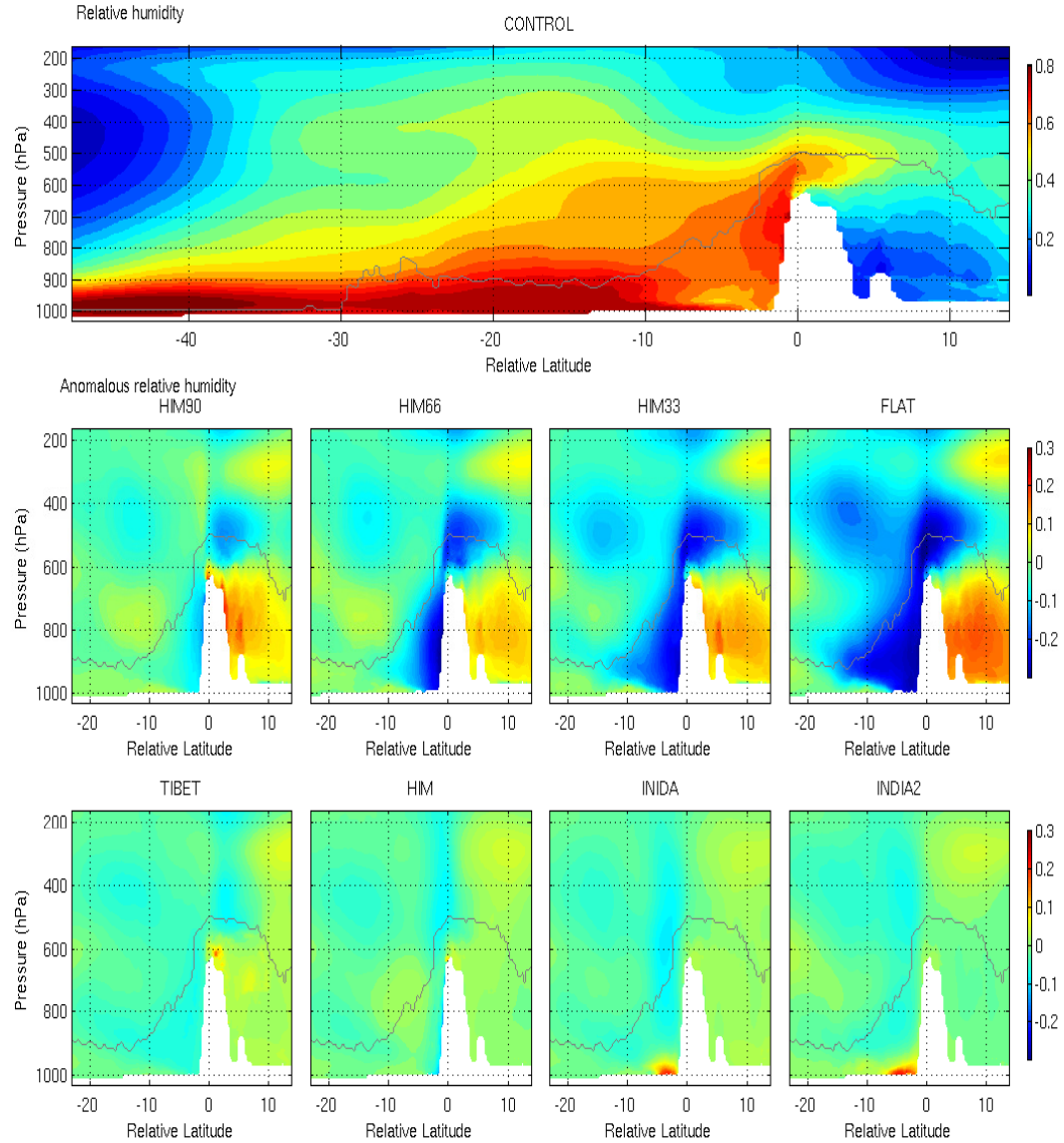


Figure 2.8: (A) Same as Figure 2.1G, but for the relative humidity of the CONTROL. (Middle and bottom panels) Same as A, but for the relative humidity difference between the experiments and the CONTROL.

2012). We will investigate the effects of orography and surface heat fluxes on the onset and decay phase of the monsoon with the high resolution model for future work.

2.4 Conclusions

A high resolution global model that resolves topography better than previous studies was used to examine effects of orography and surface heat fluxes on the South Asian summer monsoon. Experiments with altered orography and reduced surface sensible heat fluxes were conducted. As might be expected for the thermally direct monsoon circulation, we found high correlation between the strength of the monsoon, measured by the mWYI, and the thermal contrast between the θ_{eb} maximum in South Asia and the free tropospheric θ_e^* over the Equatorial Indian Ocean. The variability in the thermal contrast in these model integrations with fixed sea surface temperature is dominated by the θ_{eb} maximum, so the results can be interpreted under a convective quasi-equilibrium framework (e.g., Emanuel, 1995; Prive and Plumb, 2007a,b): the strength of the monsoon is closely associated with the amplitude of the θ_{eb} maximum located south of the Himalayas. It is shown that when the bulk of the Tibetan Plateau is removed, the South Asian monsoon does not change much as long as the narrow range of the Himalayas is preserved. Without the Tibetan Plateau, the monsoon weakens as the height of the Himalayas decreases, because of enhanced penetration of the low θ_e air from the north. Decreased surface heat fluxes in different regions can also reduce the θ_{eb} maximum and weaken the monsoon, with the largest weakening occurring when the sensible heat sink is placed directly over the non-elevated regions with the highest θ_{eb} , consistent with the results of Boos and Kuang (2013).

However, given the same change in θ_{eb} , the monsoon changes more in the simulations with altered orography than in those with reduced surface heat fluxes. It is suggested that reduced orography brings dry air north of the Tibetan Plateau into the regions with the highest θ_{eb} , causing this difference. In the experiments with reduced surface heat fluxes, the value of anomalous upper tropospheric θ_e^* is approximately tied to that of the θ_{eb} anomaly, as in strict convective quasi-equilibrium. In contrast, when the free troposphere gets drier,

convection requires a more unstable stratification, leading to a greater reduction in free tropospheric θ_e^* than in θ_{eb} , and hence a greater weakening of the monsoon. These results illustrate the importance of deviations from strict quasi-equilibrium in setting the strength of the monsoon, a complexity that may need to be added to existing theories of the monsoon based on strict quasi-equilibrium (e.g., Emanuel, 1995; Chou and Neelin, 2003), and call attention to an additional mechanism through which the monsoon may respond to changes in the hydrological cycle.

Chapter 3

A mechanism-denial study on the Madden-Julian Oscillation with reduced interference from mean state changes ¹

abstract

Mechanism-denial experiments using Superparameterized Community Atmosphere Model are conducted to investigate the importance of extratropical and circumnavigating waves, wind-evaporation feedback and radiative-convective feedback to the Madden-Julian Oscillation (MJO). A common issue with mechanism-denial studies is the interference from mean state changes when processes are turned off in the model. Here, time-invariant forcing and nudging on effective timescales longer than the intraseasonal timescale are implemented to maintain the mean state. The MJO activity remains largely unchanged with suppressed extratropical and circumnavigating waves when the mean state is maintained to

¹Co-authored with Zhiming Kuang

be close to that of the control run, suggesting that excitation of MJO by extratropical and circumnavigating waves is not necessary for the existence of MJO in this model. It is also shown that the wind-evaporation feedback slows down eastward propagation of the MJO, and the radiative-convective feedback amplifies the MJO.

3.1 Introduction

The MJO (Madden and Julian, 1971) is the dominant mode of intraseasonal variability in the tropics, and has been extensively studied in the past few decades (see, e.g., review by Zhang, 2005). The characteristics of the MJO are well documented. The MJO features a spatial scale of zonal wavenumbers 1-3 and eastward propagation primarily in the Indian Ocean and western Pacific Ocean at around 5 m s^{-1} . Below we introduce the processes considered important to MJO initiation and maintenance in previous studies and examined here, including (i) surface heat fluxes and radiative fluxes, i.e., sources of the column-integrated moist static energy (hereafter column MSE) (e.g., Hu and Randall, 1994; Maloney *et al.*, 2010; Andersen and Kuang, 2012), and (ii) influences of extratropical waves (e.g., Liebmann and Hartmann, 1984; Lau and Phillips, 1986) and circumnavigating waves (e.g., Knutson and Weickmann, 1987).

The MJO has been hypothesized as a moisture mode in the sense that column moisture dominates the column MSE variations, and the growth and maintenance of the MJO is often interpreted in the context of processes recharging the column MSE while the MJO's propagation is sometimes viewed as the result of horizontal moisture advection which has been argued to lead column MSE (e.g., Fuchs and Raymond, 2002; Maloney *et al.*, 2010; Sobel and Maloney, 2012; Sobel *et al.*, 2014; Pritchard and Bretherton, 2014). Wind-evaporation feedback and radiative-convective feedback are examples of such processes and are considered important to the MJO (e.g., Bony and Emanuel, 2005; Sobel *et al.*, 2010). With details different from the originally proposed linear theory (Emanuel, 1987; Neelin *et al.*, 1987), surface heat flux anomalies, led by surface wind anomalies, are argued to be positively correlated with the column MSE, and therefore strengthen the MJO (e.g., Maloney,

2009; Sobel *et al.*, 2010; Kiranmayi and Maloney, 2011). The radiative heating anomaly is found to be in phase with MJO precipitation and column MSE (Lin and Mapes, 2004; Ma and Kuang, 2011), and plays a significant role in maintaining the column MSE anomaly associated with the MJO (e.g., Andersen and Kuang, 2012; Sobel *et al.*, 2014).

The recharge-discharge mechanisms for the MJO are internal to the tropics. However, coherence between the tropical convection and extratropical circulation on the intraseasonal timescale has been noticed since the 1980s (e.g., Weickmann, 1983; Lau and Phillips, 1986), and Hsu (1996) suggested that the intraseasonal oscillation is a global phenomenon. Despite controversy over the statistical significance of the dependence between the tropical and extratropical intraseasonal signals (Ghil and Mo, 1991), many studies tried to better understand the interactions between the oscillations in the tropics and those in the mid-latitudes. One direction of the interaction is through the propagation of Rossby waves generated by tropical heating, which leads to global responses (Jin and Hoskins, 1995; Matthews *et al.*, 2004). In the other direction, it has been observed that extratropical waves can propagate into the tropics in the regions with westerlies and lead to MJO initiation (e.g., Hsu *et al.*, 1990). Hoskins and Yang (2000) further showed that westerly winds are not necessary for extratropical influence on the tropical atmosphere because extratropical forcing can project onto the equatorial modes. More recent results from numerical integrations indicate that proper extratropical forcing leads to MJO initiation (Lin *et al.*, 2007; Ray *et al.*, 2009; Ray and Zhang, 2010). In addition to extratropical waves, it has also been proposed that eastward circum-equatorial propagation of a Kelvin wave caused by a preceding MJO event (e.g., Knutson and Weickmann, 1987).

Mechanism-denial experiments have been conducted in recent years to examine the importance of particular processes to the MJO (Kim *et al.*, 2011; Ray and Li, 2013; Pritchard and Bretherton, 2014). However, in these mechanism-denial studies, MJO response to the suppression of a particular process without being mediated by mean state changes is not distinguished from the response to the departure of mean state away from the control simulations, which leads to ambiguity in the interpretation. To examine the direct influences

(i.e., without being mediated by mean state changes) of particular processes on the MJO, we have designed measures, largely inspired by Hall (2000), to minimize changes to the mean state when processes are disabled in the model. The methodology will be introduced in Section 3.2, including the model configuration, and experimental setup. In Section 3.3, we will first examine how the climatology and MJO activity respond in the experiments with suppressed extratropical waves, and use these experiments as an example to illustrate the importance of maintaining the mean state in mechanism-denial studies. The results from the other experiments are presented in the same section. A brief summary and further discussions follow in Section 3.4.

3.2 Methodology

3.2.1 Model

We used the Super-Parameterized Community Atmosphere Model (SPCAM; Khairoutdinov and Randall, 2001) Version 3.5, in which the conventional cloud parameterizations in the Community Atmosphere Model are replaced by a two-dimensional cloud system-resolving model (Khairoutdinov and Randall, 2003). SPCAM is chosen because it is known to produce robust MJO signals without tuning convection parameterization (e.g., Khairoutdinov *et al.*, 2005; Andersen and Kuang, 2012; Benedict *et al.*, 2014; Pritchard and Bretherton, 2014). The simulations are conducted using semi-Lagrangian advection at T42 resolution (around 280 km) with 30 vertical levels on the Community Atmosphere Model level. On each grid point of the Community Atmosphere Model component, the embedded cloud-resolving array has 32 grid points that spans 128 km in the north-south direction. All the integrations are forced with perpetual February, the peak season of MJO activities (Zhang and Dong, 2004), sea surface temperature (Hadley Center Optimally Interpolated Sea Surface Temperature, averaged from 1980-2000). The simulations are integrated for 13 years and the first 3 years are discarded.

Table 3.1: *Brief description of the experiments. See text for details.*

	process disabled	time-invariant forcing	nudging
CTL	n/a	×	×
NDG	n/a	×	✓
CHNn	extratropical waves outside of 30°N and 40°S	×	×
CHN	extratropical waves outside of 30°N and 40°S	✓	✓
CHN2	extratropical waves outside of 10°N and 30°S	✓	✓
BOX	extratropical wave outside of 30°N and 40°S and circumnavigating waves	✓	✓
FLX	wind-evaporation feedback	✓	✓
RAD	radiative-convective feedback	✓	✓

3.2.2 Experimental setup

Table 3.1 provides a brief description of the experiments. Inspired by Hall (2000), time-invariant forcing is applied to maintain the mean state. For each experiment, an ensemble of 28 simulations are restarted from different points of the CTL run, and integrated for 20 days. The first ensemble member restarts from the point where the CTL run has been integrated for six years, with each of the of following ensembles lagging the previous one by three months. Time-invariant forcing is computed using the tendency with which the ensemble mean drifts away from the climatology of the CTL run, and then applied to the next set of ensemble simulations. After four such iterations, the forcing can mostly compensate for the effects of the processes turned off. We also nudged the prognostic variables in the tropics back to the control run climatology on effective timescales longer than the intraseasonal timescale to make sure the mean state is well maintained in a long-term integration (see Appendix A for details).

To constrain the impact of the nudging described in Appendix A, NDG is integrated with the prognostic variables nudged back to the mean state of CTL. In CHN and CHNn, the intraseasonal disturbance can grow and propagate within a wide channel in the tropics, as the prognostic variables are relaxed towards the control run climatology north of 30°N and south of 40°S . The relaxation rate starts from zero at 30°N and 40°S, and increases linearly

poleward till 42°N and 52°S , respectively, so that the waves emanating from the tropics are not reflected back. Poleward of 42°N and 52°S , the relaxation time is fixed at 9 hours. These latitudes are chosen so that the damping reaches sufficiently low latitudes to adequately suppress the extratropical waves, but does not extend too far into the tropics and suppress the patterns (e.g., Rossby gyres) associated with the MJO. The procedure to maintain the climatology is applied to all the experiments discussed in this paper, except CHNn (and CTL), so the climatology of the CHNn run can be substantially different from that of the CTL run. Comparison of CHNn and CHN runs highlights the interference due to changes to the climatology. To test the sensitivity to the latitudes beyond which the extratropical waves are suppressed, the equatorward boundaries of the relaxation zones are shifted from 30°N and 40°S to 10°N and 30°S in CHN2, leaving a narrower channel compared to CHN. In the experiment BOX, we further relax the prognostic variables toward the control run climatology all over the globe except within the box over the tropical Indian and Pacific Oceans (40°S - 30°N , 0°E - 270°E), so that both extratropical waves and circumnavigating waves are suppressed. In addition, radiative-convective (wind-evaporation) feedback is turned off by prescribing the radiative heating (surface fluxes) using the control run climatology in the RAD (FLUX) experiment. Again, the climatologies of all experiments except CHNn (and CTL) are maintained to be that of the CTL run.

3.3 Results

The CTL run simulates the climatology reasonably well compared to observations. The precipitation maxima are located in the western Indian Ocean, the Maritime Continent and the western Pacific Ocean between 20°S and the Equator, as it is forced by perpetual February sea surface temperature (Figure 3.1A). The time-space power spectrum of the Outgoing Longwave Radiation (OLR) is calculated with successive 90-day segments of data overlapping by 60 days in the fashion of Wheeler and Kiladis (1999). The peak at small wavenumbers and low frequencies in the spectrum shows a robust MJO signal in the CTL run (Figure 3.2A). The MJO bandpass filtered (30-90 days, wavenumbers 1-3) variance of

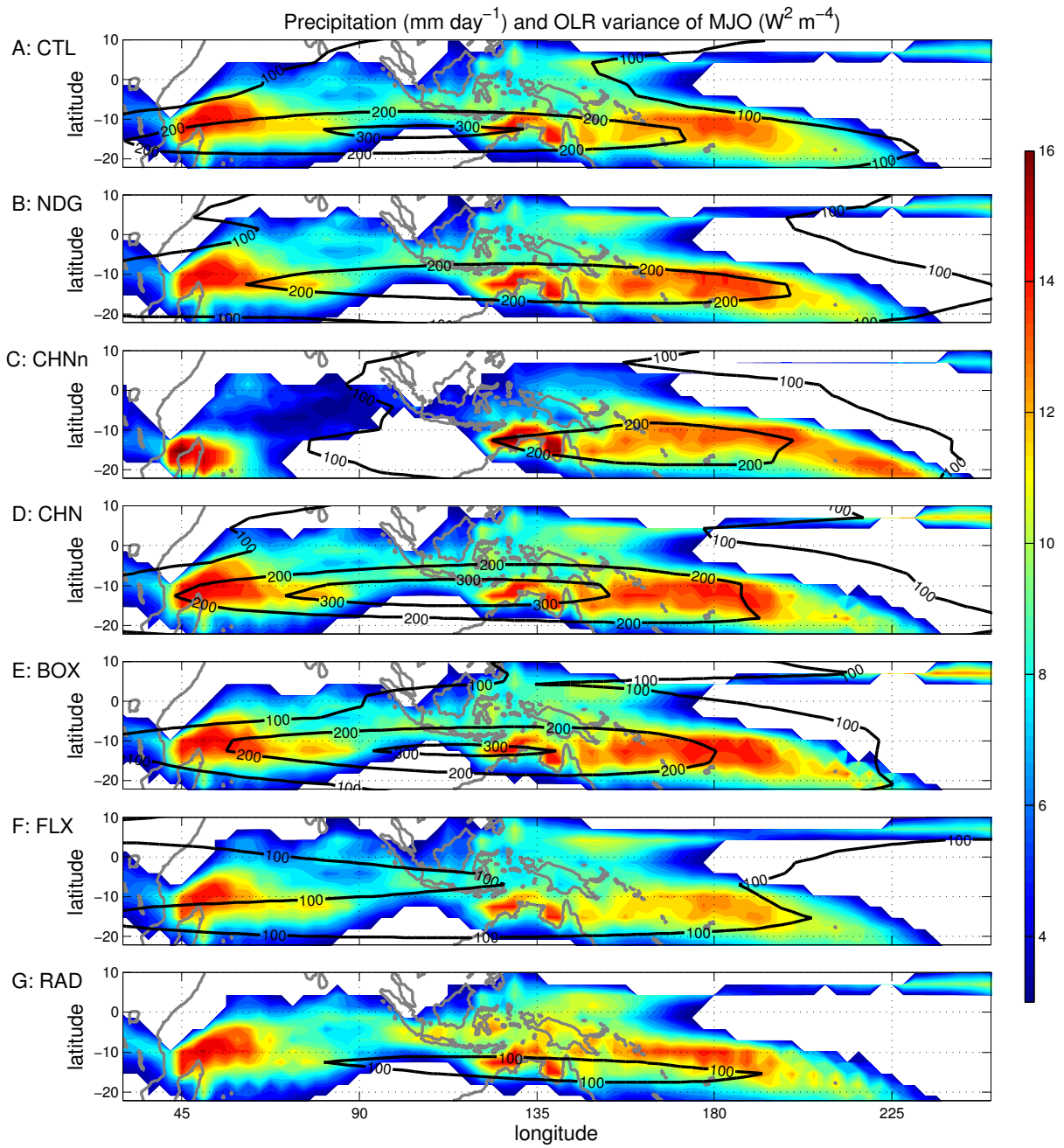


Figure 3.1: Mean precipitation (shaded) and OLR variance of the MJO (black contours) from the (A) CTL, (B) NDG, (C) CHNn, (D) CHN, (E) BOX, (F) FLX and (G) RAD. The silver contours denote the coast lines.

OLR (Figure 3.1A) indicates that the peak of MJO activity spans the Indian Ocean and the western Pacific Ocean between 20°S - 8°S , a few degrees poleward compared to observations during boreal winter (e.g., Zhang, 2005). When the prognostic variables are nudged on effective timescales longer than the intraseasonal timescale, the mean precipitation remains similar to that of the CTL run. While the tropical transients of the lowest resolved frequency ($1/90$ cpd) are damped (Figure 3.2B), the spatial distribution of MJO activity is also largely unchanged (Figure 3.1B). Despite that the power spectrum is dominated by a flat peak at wavenumbers 1-4, the frequency-wavenumber diagram confirms that the simulation produces a strong MJO signal when the nudging is implemented (Figure 3.2B).

We now turn to the responses of the mean states and MJO activity in the experiments with suppressed extratropical waves, and these experiments will serve as an example to highlight the importance of maintaining the mean states. In CTL, there are large values of eddy momentum flux convergence in the midlatitudes (Figure 3.3A), as Rossby waves originating from these latitudes propagate into the tropics and the polar regions. When the extratropical waves are suppressed, the eddy momentum flux convergence disappears in the Northern Hemisphere, while there is still weak eddy momentum flux convergence on the equator flank of the damping zone (the equatorward boundary is marked by the dashed line) in the Southern Hemisphere (Figure 3.3B). When the extratropical waves are damped starting from lower latitudes, there is a single peak of eddy momentum flux convergence in the upper atmosphere lying over the tropics (Figure 3.3C), and it confirms that the extratropical waves are adequately suppressed. In fact, the responses of the MJO are similar in both the wide channel (CHN) and the narrow channel (CHN2) experiments, so only results from CHN will be shown hereafter.

The CTL run produces a strong cross-equatorial winter cell (Figure 3.4A), and the magnitude of the Hadley Cells matches reanalysis data well (Schneider, 2006). When the extratropical waves are suppressed, the Hadley Cells and Ferrel Cells weaken (Figure 3.4B) if the mean state is not maintained (the CHNn run). In contrast, there is hardly any changes in the circulation over the tropics in CHN, and it suggests that the method implemented in

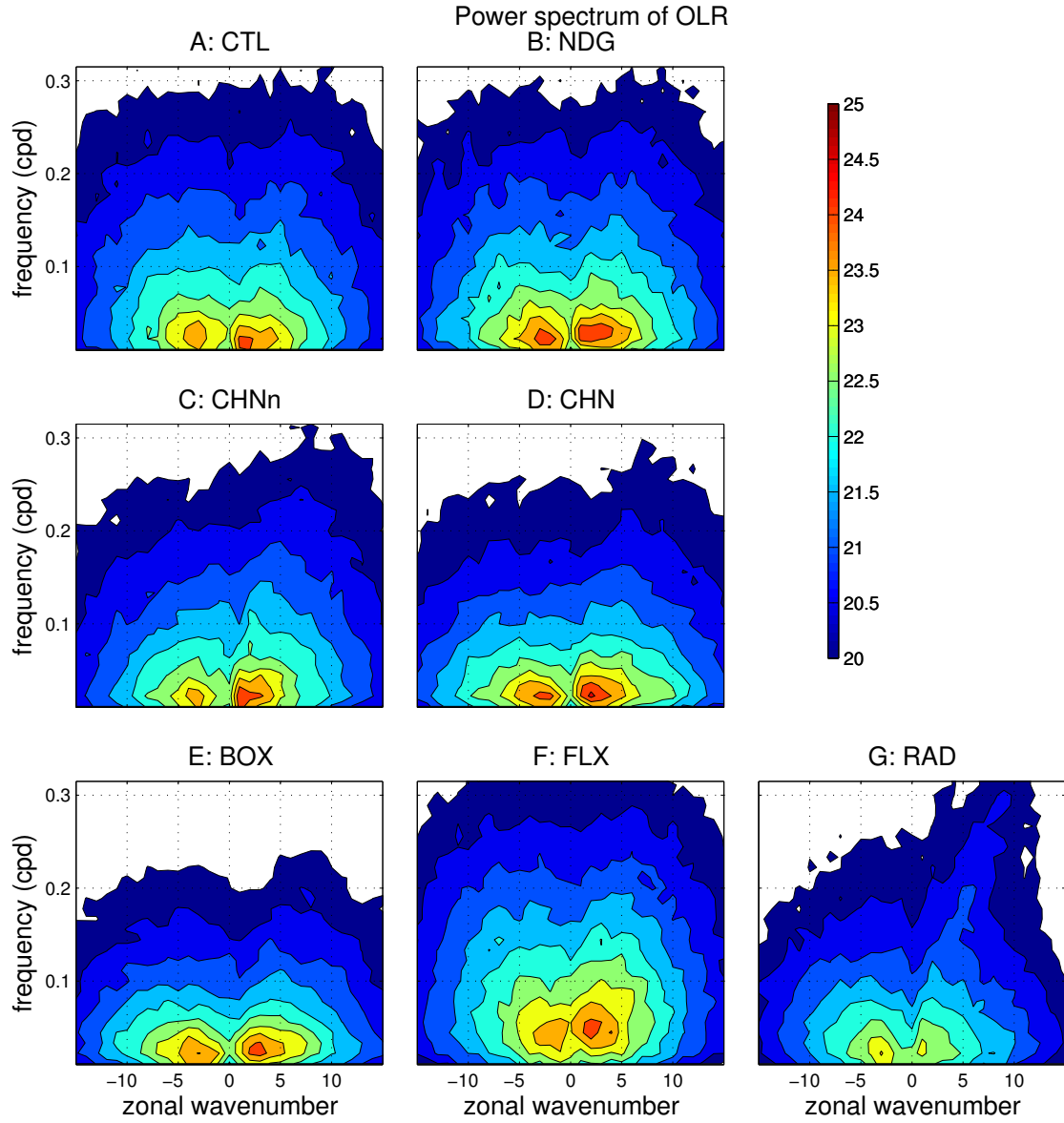


Figure 3.2: Time-space power spectra of the OLR averaged between 20°S - 0° of (A) CTL, (B) NDG, (C) CHNn, (D) CHN, (E) BOX, (F) FLX and (G) RAD.

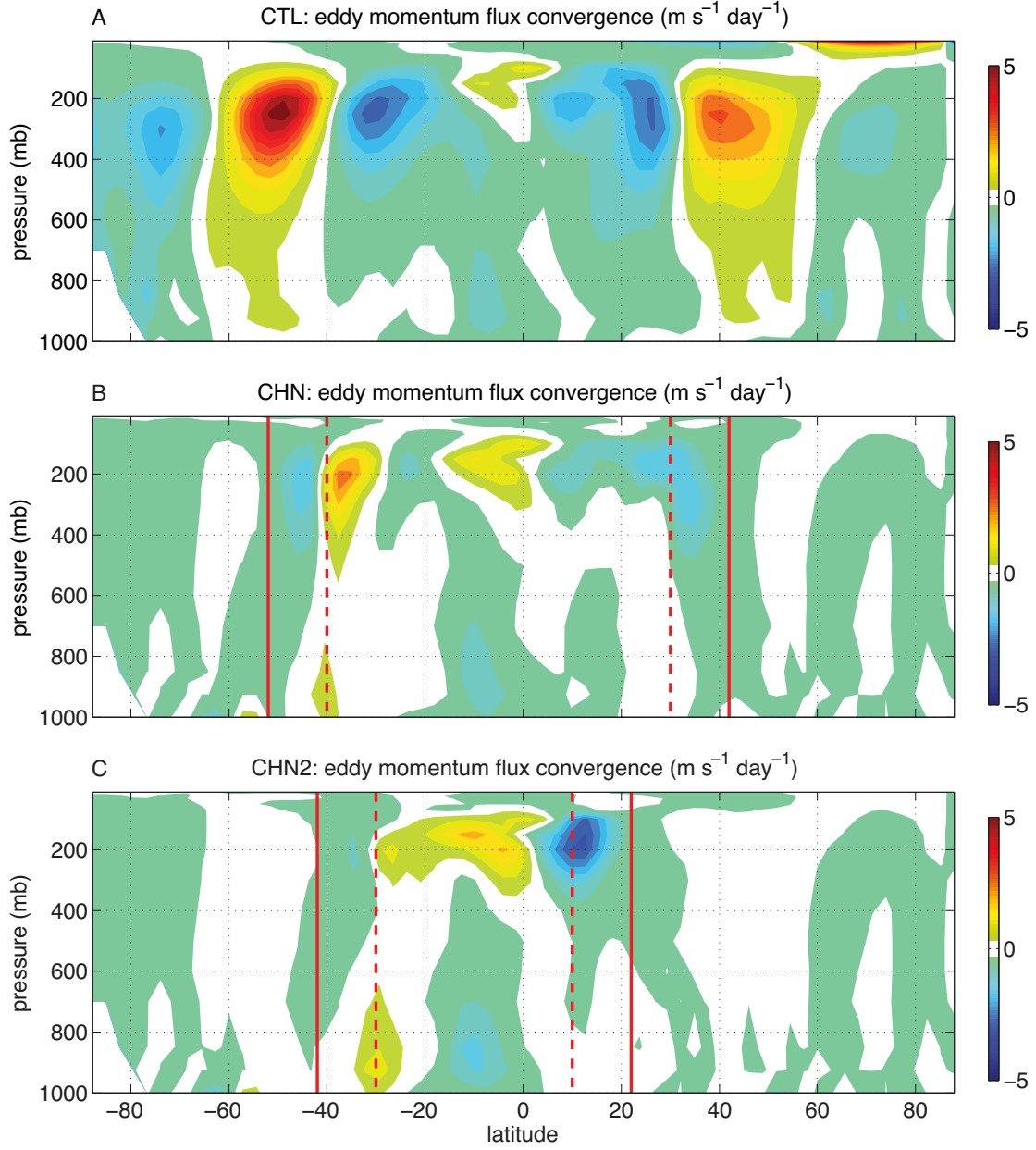


Figure 3.3: Temporal and zonal mean eddy forcing in (A) CTL, (B) CHN and (C) CHN2. In (B) and (C), the dashed lines denote the latitudes starting from which the extratropical eddies are damped. The relaxation rate increases linearly poleward till the solid lines, and remains constant poleward from the solid lines.

the present study is indeed able to minimize the departure of the mean states away from the CTL run. The response of the climatological precipitation shares a similar picture. As the Hadley Cells weaken in CHNn, the precipitation shifts poleward. The precipitation decreases over the Inter Tropical Convergence Zone, especially over the Equatorial Indian Ocean, and increases over the South Pacific Convergence Zone (Figure 3.1C), while the precipitation in CHN remains similar to that of the CTL run. The averaged precipitation over the domain with high MJO activity (between 25°S-10°N and 30°E-120°W) is 6.0 mm day⁻¹ in CTL, which is maintained to be the same in CHN, and reduced by 15% in CHNn. The pattern correlation between the precipitation in CTL and CHNn is 0.916, compared to 0.995 between that in CTL and CHN. Although the MJO signal seems to change little in the wavenumber-frequency spectrum (Figure 3.2C), the OLR variance of MJO decreases significantly in the Indian Ocean in CHNn (Figure 3.1C). As long as the climatology does not change, the spatial distribution of the MJO activity remains broadly unchanged even when the extratropical waves are suppressed (Figure 3.1D). The power spectrum also confirms that there is a strong signal of MJO without extratropical influence (Figure 3.2D).

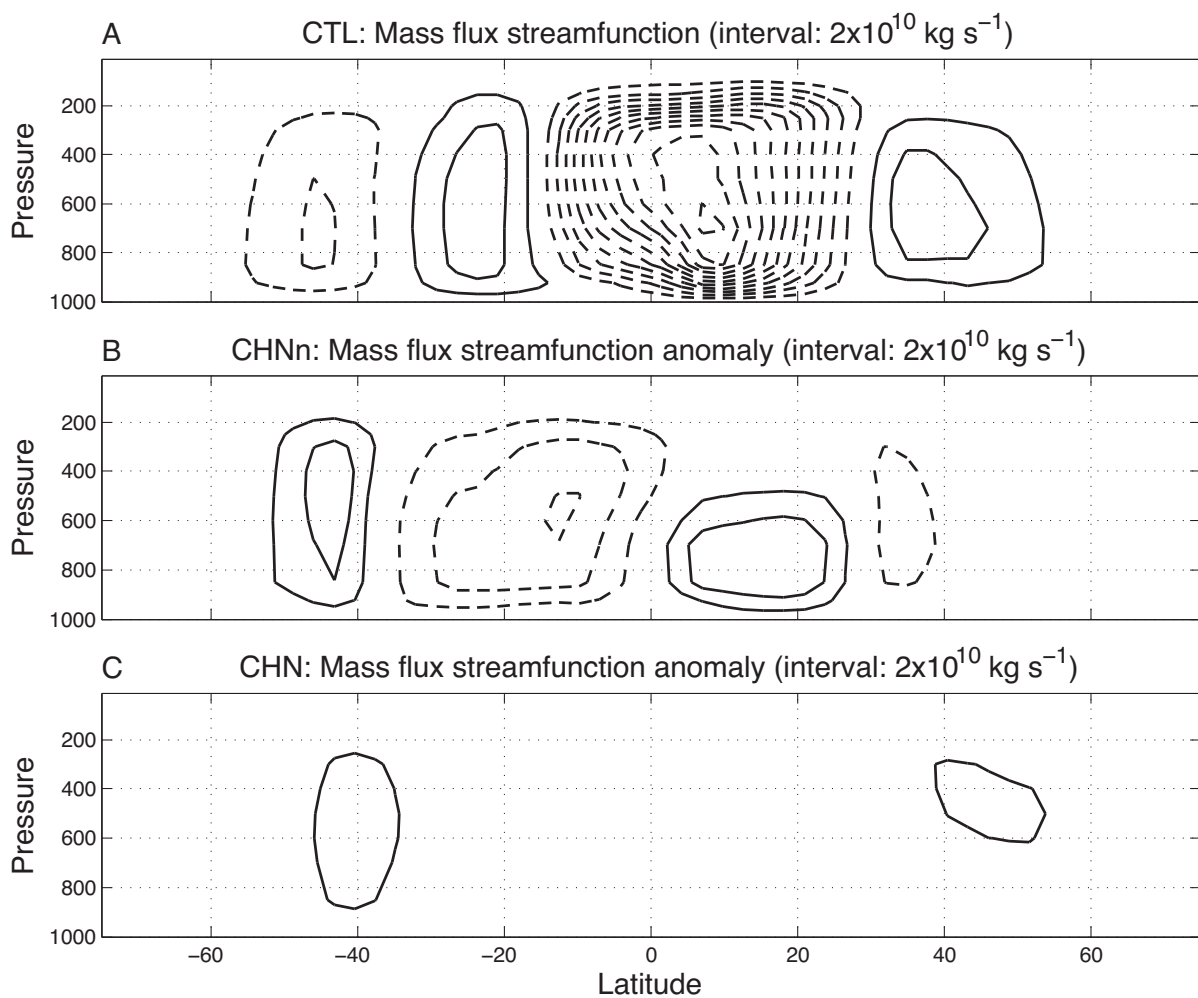


Figure 3.4: Temporal and zonal mean circulation in (A) CTL, and anomalous circulation in (B) CHNn and (C) CHN. Negative streamfunction values (dashed contours) correspond to clockwise circulation, and positive streamfunction values (solid contours) correspond to counter-clockwise circulation.

The mean states are well maintained in BOX, FLX and RAD, in which the averaged precipitation is 6.0, 6.1 and 5.9 mm day⁻¹, and the pattern correlation of the precipitation with that in CTL is 0.994, 0.993 and 0.994, respectively. The influences of the circumnavigating waves, wind-evaporation feedback and radiative-convective feedback can thus be assessed with reduced interference from mean state changes. Suppressing extratropical waves and circumnavigating waves barely changes the spatial distribution of MJO activity (Figure 3.1E). As the disturbances are suppressed over the Atlantic sector, the OLR power spectrum is dominated by a peak at zonal wavenumbers 2-3 (Figure 3.2E). The essential processes of the MJO are internal to the Equatorial Indian Ocean and the Pacific Ocean in the experiment BOX, as MJO initiation and maintenance are limited within these regions in the BOX experiment. The activity of the eastward propagating intraseasonal disturbances with planetary scales weakens significantly in FLX and RAD (Figures 3.1FG), which implies that the wind-evaporation feedback and radiative-convective feedback are important to the MJO. In FLX, the spectral peak shifts to higher frequency compared to the other experiments (Figure 3.2F), which indicates that the wind-evaporation feedback slows down MJO propagation in SPCAM. The MJO signal largely disappears in the power spectrum of the OLR when the radiative feedback is disabled (Figure 3.2G), in agreement with Kim *et al.* (2011). On the other hand, the Kelvin wave becomes stronger without interactive radiative heating in RAD, consistent with the results from Andersen and Kuang (2012).

3.4 Discussions and summary

MJO mechanism-denial experiments have been conducted in a few recent studies (e.g., Ray and Li, 2013), in which, particular processes are disabled in numerical models, and the importance of these processes to the MJO and evaluated based on how MJO responds in the simulations. The response of MJO in these studies can be decomposed into two parts: (1) response to mean state changes and (2) direct response to the suppression of certain process without being mediated by mean state changes. Using SPCAM, the present study seeks to examine the direct influences of the extratropical and circumnavigating

waves, wind-evaporation feedback and radiative-convective feedback on the MJO with reduced interference from mean state changes. Using time-invariant forcing, combined with nudging the prognostic variables back to the control run climatology on effective timescales longer than the intraseasonal timescale, we were able to minimize the changes to the climatology from CTL when processes are eliminated or suppressed in the model. Without maintaining the climatology, the strength of the general circulation and tropical precipitation is reduced in response to suppressed extratropical waves as seen in Ray and Li (2013). In particular, precipitation and MJO activity decrease significantly over the Indian Ocean. It is worth noting here the response of the mean state and MJO activity to the suppression of extratropical waves in CHNn is somewhat different from that in the simulations in Ray and Li (2013), which may be attributed to, besides model difference, the fact that the simulations are forced with perpetual February sea surface temperature in the present study, while the simulations in Ray and Li [2013] are integrated with annual cycle. The MJO activity remains generally the same as in the CTL run when the mean state change is minimized, leading to the conclusion that excitation of MJO by extratropical eddies are not essential for the existence of the MJO. This contrast highlights the importance of reducing the interference from mean state changes in mechanism-denial experiments. Results also suggest that the processes important to the MJO are internal to the tropical Indian and Pacific Oceans in SPCAM, because the simulation produces strong MJO signals when the transients can only grow and propagate within these regions. The wind-evaporation feedback is found to slow down MJO propagation in the model. When the radiative-convective feedback is turned off, the MJO signal weakens significantly.

As the results show that excitation of MJO by extratropical and circumnavigating waves are not necessary for MJO's existence, it leads to the open question that how the present results can be reconciled with previous studies, in which the influences of extratropical and circumnavigating waves are argued to be important to MJO initiation. It is possible that the extratropical waves and circumnavigating waves determine the timing for some MJO initiation events, but the collective effects of the waves over a long period have little influence

on MJO climatology. Besides, the circumnavigating waves might play a more significant role in MJO amplitude in idealized models such as that used by Maloney and Wolding (2015). The wind-evaporation feedback is shown to slow down the MJO, which is consistent with reanalysis data and numerical studies (Kiranmayi and Maloney, 2011; Maloney, 2009). In an idealized simulation of the MJO (Andersen and Kuang, 2012), the surface flux is found to project positively onto the tendency of the column MSE, and the difference is attributed to the mean surface easterly winds in the idealized simulation, compared to the weak to westerly winds in the observations and realistic simulations. One caveat with the present study is the simulations are forced with fixed sea surface temperature, while it has been argued that including air-sea coupling in SPCAM can produce more realistic phasing between surface flux and precipitation and improve the simulated MJO (Benedict *et al.*, 2011). The radiative-convective feedback amplifies the MJO not only because, in the active phase of the MJO, the anomalous column-integrated radiative heating serves as a direct source of column MSE, but also due to the bottom-heavy profile of the radiative heating anomaly (Ma and Kuang, 2011), which generates a bottom-heavy vertical velocity profile and can further import MSE into the column. In contrast, such bottom-heavy radiative heating anomaly in the convectively active phase weakens the Kelvin wave, as the stratiform instability for convectively coupled waves counts on top-heavy convective heating (Mapes, 2000; Kuang, 2008a). Also, a radiative-convective instability involving the interaction among radiative heating, water vapor, clouds and large-scale circulation has been proposed recently (Emanuel *et al.*, 2014; Wing and Emanuel, 2013), and observational and numerical studies are needed to relate this instability to realistic MJO initiations.

Chapter 4

Modulation of radiative heating by the Madden-Julian Oscillation and convectively coupled Kelvin waves as observed by CloudSat ¹

abstract

The vertical distribution of radiative heating affects the moist static energy budget and potentially the maintenance and propagation of the Madden-Julian Oscillation (MJO). This paper uses CloudSat data to examine the radiative heating climatology in the tropics and the vertical structure of its modulation by the MJO and convectively coupled Kelvin Waves (KW). Composites of active regions of the MJO and KW both show positive radiative heating anomaly in the middle and lower troposphere and slightly negative radiative heating anomaly in upper troposphere. Such bottom-heavy profiles can help to strengthen the MJO while weaken the KWs. Another finding is that cloud condensate anomalies associated with

¹Co-authored with Zhiming Kuang

the MJO are significantly more bottom-heavy than those of the KWs, while the radiative heating anomalies associated with the MJO are only very slightly more bottom-heavy.

4.1 Introduction

Although the MJO was first identified 40 years ago (Madden and Julian, 1971) and has long been recognized as an important phenomenon, it is still not well understood. The MJO features planetary scale circulation and convection signals in the tropics that propagate eastward at a speed of around 5 m s^{-1} . The convective signals of the MJO are clearly seen in the Outgoing Longwave Radiation (OLR) data, and its temperature, moisture and wind structures have been quite well documented (e.g., Wheeler and Kiladis, 1999; Kiladis *et al.*, 2005; Zhang, 2005). Besides being the dominant intraseasonal variability in the tropics, the MJO also affects the El Nino-Southern Oscillation, tropical cyclones, Asian and Australian monsoons, and mid-latitude weather (e.g., Zhang, 2005). The persistent difficulty in simulating the MJO with general circulation models highlights our insufficient knowledge of how the atmosphere operates in the tropics (e.g., Lin, 2006; Kim, 2005), and improved prediction and understanding of the MJO would also benefit weather and climate forecasts.

A recently emerged view of the MJO is that, unlike the fundamentally buoyancy driven convectively coupled waves, processes that alter the column integrated moist static energy (MSE), are essential to the existence and the propagation characteristics of the MJO (e.g., Raymond and Fuchs, 2007; Sobel *et al.*, 2008; Maloney, 2009). Radiative heating is known to be an important example of such a process. The extensive clouds in the active regions of the MJO, which have higher column-integrated MSE and enhanced convection, reduce the radiative cooling and help to amplify the original column MSE anomaly. Combining surface and top of the atmosphere radiative flux measurements, Lin and Mapes (2004) found that column integrated radiative heating anomaly is nearly in phase with the precipitation anomaly with a magnitude around 10-15% of the heating associated with the precipitation. Because column integrated radiative heating represents a net source of column integrated MSE, this amount is very significant, comparable to the amount of column MSE export

associated with the divergent flow. Because of this importance, radiative feedback is invoked in a number of simple models of the MJO and the tropical mean circulation (e.g., Raymond, 2001; Tian and Ramanathan, 2003; Bony and Emanuel, 2005; Sugiyama, 2009).

In addition to its column integral, the vertical distribution of radiative heating can also be important because it affects the efficacy of the circulation that arises in response to this radiative heating in importing or exporting column MSE. As briefly discussed by Kuang (2011) and confirmed by cloud-resolving model simulations, if the radiative heating is concentrated in the lower troposphere, the divergent circulation that arises to balance this heating results in more import of column MSE and further enhancement of convection. On the other hand, if the radiative heating is concentrated in the upper troposphere, the divergent circulation that arises results in more export of column MSE. Thus, for the same amount of column integrated radiative heating, a more bottom-heavy profile will result in a stronger response in the precipitation.

The goal of this paper is to constrain the vertical distributions of radiative heating anomalies associated with the MJO using radiative heating profiles from CloudSat, which are derived from its multiyear global reflectivity measurements from the 94 GHz Cloud Profiling Radar (CPR) (Stephens *et al.*, 2002). Previous studies have used CloudSat to examine cloud structures associated with the MJO and the boreal summer intraseasonal variabilities (Masunaga *et al.*, 2008; Riley *et al.*, 2011; Jiang *et al.*, 2011). In addition to results for the MJO, we will also present the results for convectively coupled KWs. While radiative feedback is not believed to be essential for the existence of convectively coupled waves (e.g., Mapes, 2000; Khouider and Majda, 2006; Kuang, 2008a,b; Andersen and Kuang, 2008), how radiative heating is distributed vertically could still modify the characteristics of these waves.

4.2 Data and method

We use radiative heating, cloud water/ice, water vapor and temperature data from CloudSat. The level 2 radiative fluxes and heating rates algorithm (2B-FLXHR) of CloudSat produces

vertically resolved radiative heating data set based on the results from CloudSat's CPR. Cloud water/ice content data is provided by the level 2 radar-visible optical depth cloud water content product (2B-CWC-RVOD), using a combination of measured radar reflectivity factor and estimates of visible optical depth. Radiation and cloud data from September 1, 2006 to August 31, 2010 are used. We also analyzed temperature and water vapor data contained in the ECMWF-AUX product of CloudSat, which is derived from the European Center for Medium-Range Weather Forecasts reanalysis. Temperature and moisture structures associated with the MJO have been extensively documented before (e.g., Kiladis *et al.*, 2005; Tian *et al.*, 2006) and are included here only for reference. Only one year of the temperature and water vapor data (from September 1, 2006 to August 31, 2007) was used, which already yielded clear signals for our purpose. We shall use the 2.5° latitude \times 2.5° longitude global NOAA Interpolated daily mean outgoing longwave radiation (OLR) dataset to identify the MJO and Kelvin wave events.

A major limitation of this work is that radiative heating and cloud condensate are derived products instead of raw measurements such as the radar reflectivity. The cloud condensate products are retrieval results based on a priori log-normal size distributions constrained by the measured radar reflectivity. The products also have issues in heavily precipitating scenes because of radar attenuation and deviations from log-normality. The radiation fields are results from further radiative transfer calculations based on the cloud condensate values and reanalyzed temperature and moisture data. Despite these uncertainties, the CloudSat data represent our best current estimates of global cloud condensate and radiative heating rate distributions and it is worthwhile to have a first look at the modulations of these fields by the MJO and the KWs. Furthermore, atmospheric layers with heavy precipitation are in general already optically opaque so that radiative heating rates there are not sensitive to changes/errors in the cloud condensate retrievals, as we have verified in offline radiative transfer calculations. One might also reasonably expect differences seen between the composite structures of the MJO and the KWs to be less sensitive to the aforementioned uncertainties.

To construct the MJO composite, we first average OLR data along the equator (between 10°S and 10°N), and then filter the data according to the space-time spectral window of the MJO (zonal wavenumber 0.5-9.5, frequency 0.01-0.05 cycles per day), following the approach of Wheeler and Kiladis (1999). For each day, the local minima of the filtered OLR with values less than -20 W m^{-2} are identified, and labeled as the "active convective centers". CloudSat data within 10°N/S are then binned according to their relative position to the active convective center of the MJO on the day they were collected to produce a composite structure. KWs composites are constructed similarly. With this simple procedure, we have neglected regional differences in MJO and KW structures.

4.3 Results

To provide a context for the anomalies to be discussed, we present in Figure 4.1 the 4-year (September 1, 2006-August 31, 2010) averages of (A) shortwave (SW), (B) longwave (LW), (C) total radiative heating rates, (D) total cloud water content averaged between 10°N/S and shown as a function of longitude (we have diurnally averaged the data and applied a 10°-longitude moving average). In Figure 4.1E, we also show the number of days for which the identified active convective centers of the MJO/KWs fall in a particular 2.5° longitude bin. Note that even though there are higher frequencies of convective centers associated with the KWs, the MJO is more influential because the MJO anomalies span a wider range in space. The active centers mostly reside over the Indian Ocean and the western Pacific Ocean. The climatology of cloud water content is consistent with previous studies (e.g., Waliser *et al.*, 2009). The strong impact of the time-mean cloudiness is apparent in the radiative heating climatology. Over the Indian Ocean, west Pacific Ocean and the Amazon, because of active deep convection in these regions, there is abundant cloud water between 400 hPa to 600 hPa, with a maximum cloud water content around 60 mg m^{-3} . In these regions, daily mean SW heating is strongest in the upper troposphere and peaks at around 1 K day^{-1} around 400 hPa. Over the central and eastern Pacific, cloud water is concentrated below 700 hPa, because this region is dominated by shallow stratus clouds, and the daily mean SW

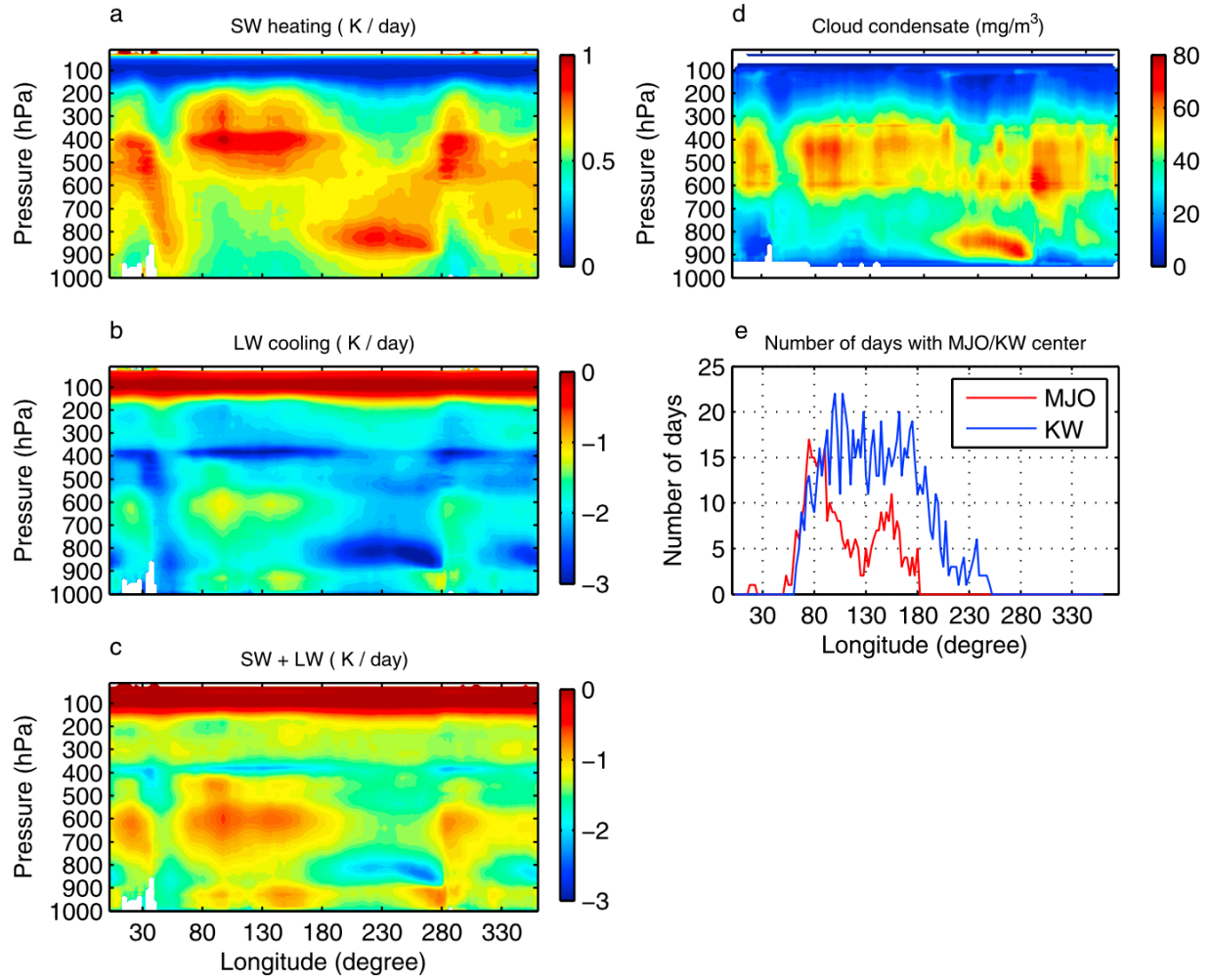


Figure 4.1: The 4-year climatology of radiative heating averaged between 10°S and 10°N (A) SW, (B) LW, (C) total radiative heating, (D) total cloud water content, and (E) the number of days for which the identified active centers of the MJO/KWs fall in a particular 2.5 degrees longitude bin.

heating peaks around 1 K day^{-1} between 700 hPa and 900 hPa. Such spatial patterns are due to SW absorption by cloud condensates. Similarly, the LW radiative heating distributions also show strong imprints of clouds, because of the strong emissivity of clouds compared to clear sky atmosphere. The maximum LW cooling at the top of the stratus clouds over the eastern Pacific Ocean reaches -3 K day^{-1} . Deep convective clouds over the warm pool strengthen the LW cooling around 400 hPa, also reaching -3 K day^{-1} , while weakening the LW cooling rates in the mid-troposphere to -1.3 K day^{-1} . Overall, the LW cooling is stronger than the SW heating so that total radiative cooling distribution to a large extent resembles that of the LW cooling. These results are generally consistent with previous estimates (e.g., L'Ecuyer and McGarragh, 2010).

Within active MJO regions, deep convection is enhanced. SW heating (Figure 4.2A) increases by around 30% above 500 hPa. There are two peaks of positive SW heating anomalies, one near 400 hPa and another near 200 hPa, the latter being the main detrainment level of anvils, and the peak values reach 0.3 K day^{-1} . Below 500 hPa is a negative SW heating anomaly of around -0.1 K day^{-1} . The signals extend 20 degrees east and west of the convective center. Patterns of LW anomalies (Figure 4.2B) are similar to those of SW except with the opposite signs. LW cooling increases by 0.5 K day^{-1} near 400 hPa and at 150 hPa. The decreased LW cooling below 400 hPa is more bottom-heavy than that of the climatology, with a maximum of 0.9 K day^{-1} at 900 hPa. The total radiative heating anomaly (Figure 4.2C) is dominated by LW anomalies. Active MJO reduces radiative cooling in the column, with a peak of 0.7 K day^{-1} near the cloud base (around 930 Pa). When we integrate the data vertically, the column integrated radiative heating anomaly peaks at around 20 W m^{-2} near the active convective center of the MJO.

The strong convection is apparent in the anomalous cloud water content (Figure 4.2D). Cloud water increases by around 50%, peaking at 30 mg m^{-3} between 500 hPa and 600 hPa. It is interesting to note that there is not a vertical tilt in the cloud condensate anomalies that is often associated with the MJO cloud fields (Benedict and Randall, 2007). The total anomalous cloud water signal extends from 900 hPa to 100 hPa and shows a middle-heavy

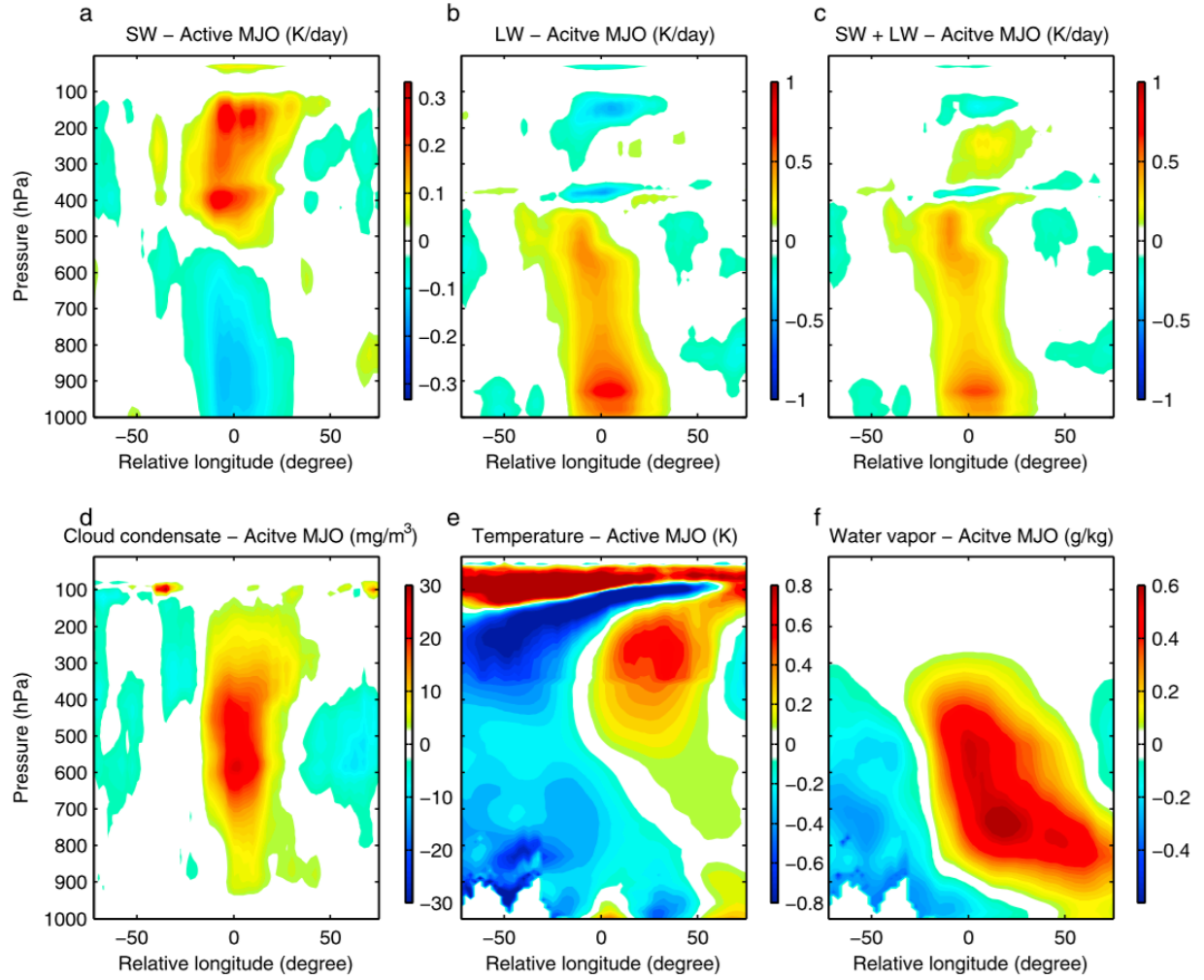


Figure 4.2: The vertical-longitudinal distributions of anomalous (A) SW, (B) LW, (C) total radiative heating, (D) total cloud water, (E) temperature, and (F) water vapor associated with the MJO.

profile, indicating a greater increase of mid-level clouds compared to the climatology. Because radiation is derived from cloud water, the distribution of cloud water is consistent with the pattern of radiation anomalies. Additional clouds absorb more solar radiation. This increases SW heating in the upper troposphere while reducing the solar radiation reaching the lower troposphere, decreasing the SW heating there. Meanwhile, cloud water is a stronger LW emitter than clear sky air so LW radiative cooling increases above 450 hPa, while radiative cooling decreases below that level because of the enhanced greenhouse effect. We have also constructed meridional composites (figures not shown) and similar characteristics are observed. The width of MJO signal in latitude is closely related to the width of the ITCZ. Composite structures of temperature and water vapor are shown in Figures 4.2EF for reference. The temperature structure shows the well-known boomerang shape, while the water vapor anomalies tilt westward with height, both consistent with previous studies (e.g., Kiladis *et al.*, 2005; Tian *et al.*, 2006).

The KWs composite structures are similar to those of the MJO except the following differences. Because the KWs have shorter zonal wavelengths than the MJO, the signal for KWs is narrower, covering only 20% in longitude compared to 50% with the MJO. More importantly, KWs are also different from the MJO in that the total radiative heating (Figure 4.3C) and cloud water (Figure 4.3D) anomaly profiles of KWs are less bottom-heavy as compared to the MJO (Figure 4.2C). Anomalous temperature (Figure 4.3E) and water vapor (Figure 4.3F) for the KWs are broadly similar to those of the MJO and consistent with previous studies (e.g., Straub and Kiladis, 2002).

To further illustrate the difference between the MJO and the KW composites, we show the radiative heating (Figure 4.4A) and cloud water condensate (Figure 4.4B) profiles averaged over the 10% longitude around the reference points of the MJO (red) and KWs (blue) composites. The profiles are normalized so all values squared sum to one. Results from two 2-year subsets of the data are shown (dashed lines) to give an indication of the robustness of the results. The MJO has a clearly more bottom-heavy profile in terms of cloud water, which peaks at 600 hPa, 200 hPa lower than that from the KWs. The profile of radiative heating

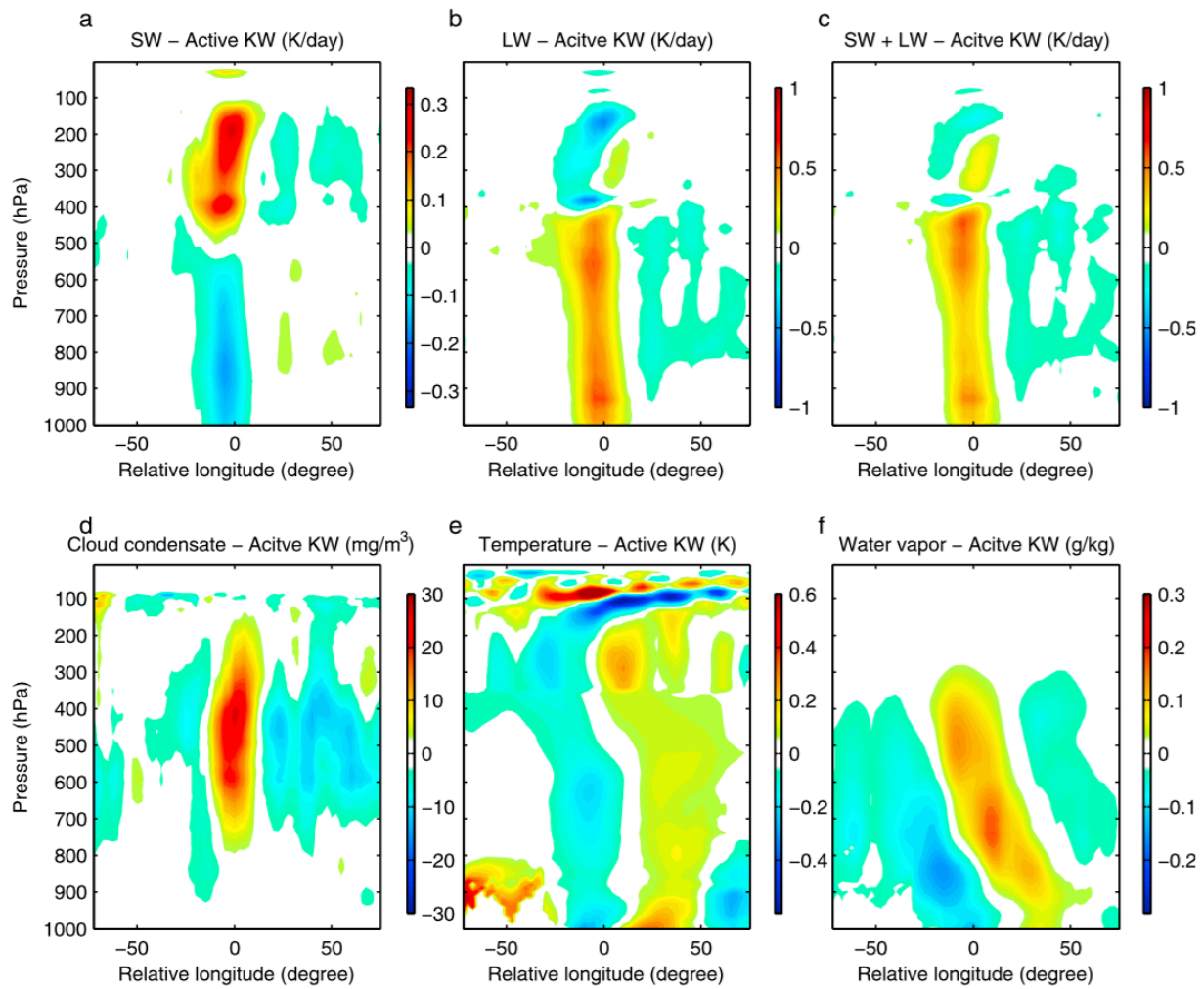


Figure 4.3: Same as Figure 4.2, but for the KWs.

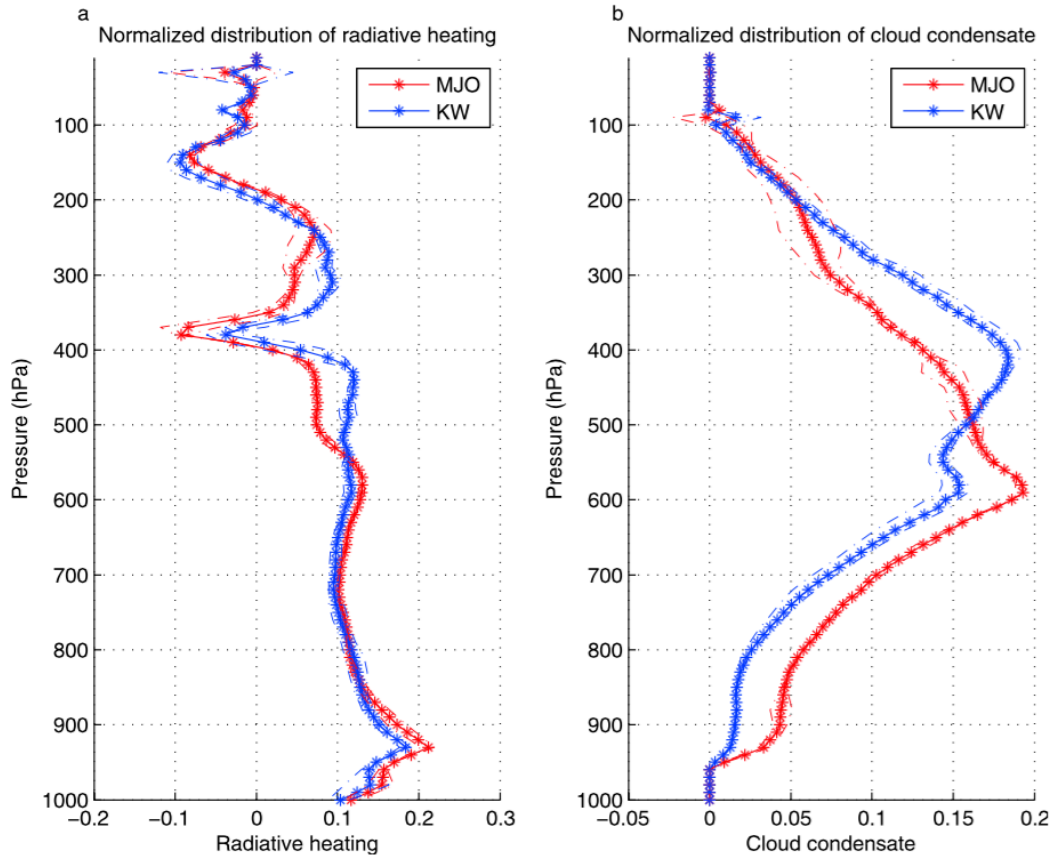


Figure 4.4: (A) Normalized vertical distribution of radiative heating and (B) total cloud water content. The solid red and blue with stars are for the MJO and KWs anomalies respectively, using the full 4-year dataset. The dashed lines are results from two 2-year subsets of the data.

anomalies associated with the MJO is also more bottom-heavy than the KWs', but only very slightly. We note that Figure 4.1E shows that the MJO and KW events that were used to produce the composites have similar spatial distributions. If anything, there are more KW events over the central Pacific, where the climatological radiative heating and cloud water profiles are more bottom-heavy. Therefore, the difference between the MJO and the KW profiles are not from biased samplings of the different local climatology. The difference in radiative heating anomalies is smaller, likely because the cloud condensate anomalies are mostly from scenes with heavy precipitation, where the atmosphere, especially the lower troposphere, is already optically opaque so that radiative heating is insensitive to cloud condensate amount.

4.4 Discussions and summary

We have used data from CloudSat, the first space-based observations of vertical cloud distributions and radiative heating profiles derived from these observations and radiative transfer calculations, to examine the modulation of radiative heating by the MJO and convectively coupled Kelvin waves. We first briefly described the climatology of radiative heating in the tropics, which shows strong imprints by clouds. Using the OLR data to identify MJO and KW events, we then made composite structures of radiative heating, cloud condensates, temperature, and water vapor for the MJO and KWs. Temperature and water vapor signals from the composites are consistent with previous studies (e.g., Straub and Kiladis, 2002; Kiladis *et al.*, 2005; Zhang, 2005; Tian *et al.*, 2006). In actively convecting regions of the MJO and the KWs, SW heating is enhanced in the upper troposphere (above 400 hPa) and reduced in the middle and lower troposphere. LW heating anomalies show a pattern of the opposite sign with larger amplitude. As a result, the total radiative heating anomaly is positive in the middle and lower troposphere and slightly negative in the upper troposphere. Such radiative heating anomaly profiles can affect the dynamics of the MJO and the KWs. Besides the net input of column MSE due to the radiative heating, the divergent circulation that arises in response to a bottom-heavy radiative heating anomaly will also

be bottom-heavy, which results in more import of column MSE and further enhancement and maintenance of column MSE anomalies associated with the MJO. On the other hand, the bottom-heavy radiative heating profile counters the top-heavy stratiform heating that convectively coupled waves rely on and can act to weaken such waves. The results presented in Figure 4.4 thus help to quantify this bottom-heaviness and its impact on the MJO and KWs. In a recent paper Andersen and Kuang (2012), it was reported that when the radiative heating feedback is disabled, convectively coupled waves are strengthened while MJO-like disturbances are weakened, consistent with the above expectations.

There are also intriguing differences between the MJO and KWs. The more bottom-heavy vertical structure of the MJO is seen clearly in the cloud condensate field. It was argued by Kuang (2011), based on cloud-system resolving model results and theoretical arguments, that for longer wavelength quasi-steady disturbances, the temperature anomalies required to drive the divergent flow become significant and will force convection to become more bottom-heavy. The finding that the MJO composite radiative heating anomaly is more bottom-heavy than that of convectively coupled KWs is consistent with this argument. Additional studies (observational and numerical) are warranted to further test this idea.

Chapter 5

Quantifying the eddy-jet feedback strength of the annular mode in an idealized GCM and reanalysis data ¹

abstract

A linear response function (LRF) that relates the temporal tendency of zonal mean temperature and zonal wind to their anomalies and external forcing is used to accurately quantify the strength of the eddy-jet feedback associated with the annular mode in an idealized GCM. Following a simple feedback model, the results confirm the presence of a positive eddy-jet feedback in the annular mode dynamics, with a feedback strength of 0.137 day^{-1} in the idealized GCM. Statistical methods proposed by earlier studies to quantify the feedback strength are evaluated against results from the LRF. It is argued that the mean-state-independent eddy forcing reduces the accuracy of these statistical methods because of the quasi-oscillatory nature of the eddy forcing. A new method is proposed to approximate the feedback strength as the regression coefficient of low-pass filtered eddy forcing onto low-pass filtered annular mode index, which converges to the value produced by the LRF

¹Co-authored with Pedram Hassanzadeh and Zhiming Kuang

when timescales longer than 200 days are used for the low-pass filtering. Applying the new low-pass filtering method to the reanalysis data, the feedback strength in the Southern annular mode is found to be 0.121 day^{-1} , which is presented as an improvement over previous estimates. This work also highlights the importance of using sub-daily data in the analysis by showing the significant contribution of medium-scale waves of periods less than 2 days to the annular mode dynamics, which was under-appreciated in most of previous research. The present study provides a framework to quantify the eddy-jet feedback strength in models and reanalysis data.

5.1 Introduction

The annular mode is a dominant mode of variability of the extratropical circulation in both hemispheres on intraseasonal to interannual timescales (Kidson, 1988; Thompson and Wallace, 1998; Gong and Wang, 1999; Thompson and Wallace, 2000). The annular mode corresponds to the leading empirical orthogonal function (EOF) of zonal mean zonal wind, which features an equivalent barotropic dipolar structure and represents latitudinal shifts of the eddy-driven midlatitude jet (Nigam, 1990; Hartmann and Lo, 1998; Thompson and Woodworth, 2014; Thompson and Li, 2015). The zonal index, the time series associated with the annular mode, is essentially the same concept as that discussed in the pioneering studies of the variability of the general circulation (Rossby, 1939; Namias, 1950; Wallace and Hsu, 1985). The annular mode in the Northern Hemisphere is often considered in recent studies as the hemispheric manifestation of the North Atlantic Oscillation (e.g., Wallace, 2000; Vallis *et al.*, 2004). The annular mode is characterized by temporal persistence (Baldwin *et al.*, 2003; Gerber *et al.*, 2008a,b), for which it has been suggested that a positive feedback between anomalous zonal flow and eddy fluxes is responsible (e.g., Feldstein and Lee, 1998; Robinson, 2000; Gerber and Vallis, 2007; Lorenz and Hartmann, 2001, hereafter, LH01). For example, Robinson (2000) suggested that at the latitudes of a positive anomaly of barotropic zonal wind, while surface drag tends to slow down low-level westerlies, it also enhances baroclinicity, which leads to stronger eddy generation. When the eddies

propagate away, in the upper troposphere, from the latitudes where they are generated, the associated anomalies of eddy momentum flux reinforce the original zonal wind anomaly. As another example, Gerber and Vallis (2007) argued that anomalous baroclinicity is not necessarily required for a positive eddy-jet feedback, as the mean flow anomaly can change the position of the critical latitudes for wave breaking and influence the eddy momentum flux convergence.

Quantifying the strength of eddy-jet feedback is important for understanding both internal variability and response to external forcing. One common issue with the current GCMs is that the simulated annular mode is too persistent compared to observations (Gerber *et al.*, 2008a), which not only indicates biases of jet variability, but also suggests overestimation of changes in the extratropical circulation in response to anthropogenic forcing in the models. According to the fluctuation-dissipation theorem (Leith, 1975), the magnitude of the forced response is positively related to the timescale of the unforced variability, a relationship that has been confirmed qualitatively in some atmospheric models (e.g., Ring and Plumb, 2008; Chen and Plumb, 2009).

Based on the assumption that the mean-state-independent eddy forcing does not have long-term memory, LH01 and Simpson *et al.* (2013, hereafter, S13) attributed positive values of lagged correlations between the zonal index and the eddy forcing, when the zonal index leads eddy forcing by a few days, to a positive feedback, and proposed statistical methods to quantify the strength of eddy-jet feedback in observations and simulations to improve understanding of the persistence of the jet. Even though S13 validated their method using synthetic time series generated by a second-order autoregressive process, their statistical method, as well as the statistical method proposed by LH01, would benefit from an assessment with more realistic time series of zonal index and eddy forcing. Due to the chaotic nature of eddies, the mean-state-dependent eddy forcing cannot be separated from the mean-state-independent part in the reanalysis data, and as a result, it is difficult to validate the assumptions of these statistical methods. Furthermore, a recent study showed that the existence of an internal eddy feedback cannot be distinguished from the presence

of external interannual forcing using only the statistical methods (Byrne *et al.*, 2016).

In the present study an LRF, following Hassanzadeh and Kuang (2016a), is used to identify the anomalous eddy fluxes in response to mean state anomalies that match the spatial pattern of annular mode in an idealized GCM. This provides the ground truth in the idealized GCM, and serves as a benchmark against which one can assess the statistical methods. The LRF will be briefly explained in Section 5.2, along with model configuration and the reanalysis data. In Section 5.3, the annular mode and a simple model of eddy-jet feedback will be introduced, followed by quantification of the feedback strength using different methods in Section 5.4. Discussions and a brief summary are presented in Section 5.5.

5.2 Methodology

For the numerical simulations, we use the Geophysical Fluid Dynamics Laboratory dry dynamical core, which solves the primitive equations with Held-Suarez forcing (Held and Suarez, 1983). Temperature is relaxed to an equinoctial radiative-equilibrium state with an equator-to-pole temperature difference of 60 K. Similar setups have been widely used to study the midlatitude circulation and its low-frequency variability (e.g., Gerber *et al.*, 2008b; Chen and Plumb, 2009; Hassanzadeh *et al.*, 2014; Hassanzadeh and Kuang, 2015; McGraw and Barnes, 2016). Each simulation is integrated for 45000 days at the T63 resolution (horizontal spacing of around 200 km) with 40 vertical levels and 6-hourly outputs, and the first 500 days are discarded. Ten ensemble simulations are conducted for the control (CTL) and an experiment (EXP). In EXP, a zonally symmetric time-invariant forcing is applied to zonal wind and temperature, so that the difference of the equilibrium mean states between EXP and CTL matches the pattern of the annular mode in CTL. This external forcing is calculated using the LRF found by Hassanzadeh and Kuang (2016a), and EXP is essentially the same as Test 3 in their article. The LRF (\mathbf{L} in Equation 5.1) relates anomalous state vector \mathbf{x} to its temporal tendency and an external forcing \mathbf{f} as,

$$\frac{d\mathbf{x}}{dt} = \mathbf{L}\mathbf{x} + \mathbf{f}, \quad (5.1)$$

in which \mathbf{x} consists of $[\mathbf{u}]$ and $[\mathbf{T}]$, zonally averaged (denoted by square brackets) zonal wind and temperature anomalies from the mean state of CTL. Assuming that eddies are in statistical equilibrium with the mean flow in the long-term integrations, Equation 5.1 is valid for weak external forcings (see Hassanzadeh and Kuang, 2016a for more details). With \mathbf{x}_o denoting the anomalous state vector associated with the annular mode, the particular external forcing for EXP is $\mathbf{f}_o = -\mathbf{L}\mathbf{x}_o$.

It is worth mentioning that Hassanzadeh and Kuang (2016a) have shown that the leading EOF of $[\mathbf{u}]$ and $[\mathbf{T}]$ strongly resembles the singular vector of the LRF that has the smallest singular number (the so-called neutral vector, see Goodman and Marshall, 2002), which confirms that the annular mode is indeed a dynamical mode, rather than a statistical artifact, in the idealized GCM. They further argued that given the similarities between the annular mode in the real atmosphere and the one simulated in the idealized GCM, it is plausible that the annular mode is also the neutral vector and hence a real dynamical mode of the real atmosphere (and atmospheres modeled with more complex GCMs), which can explain the ubiquity of annular-mode-like responses in the forced atmospheric circulations.

For the observational analysis, National Centers for Environmental Prediction reanalysis 2.5° latitude \times 2.5° longitude 6-hourly wind and temperature from 1951 to 2014 are used. Anomalies are calculated by removing the annual average and the first four Fourier harmonics as in LH01. Following Baldwin *et al.* (2009), spatial weighting is applied to EOF analysis and projections of spatial patterns to compensate for the uneven distribution of grids in both model outputs and reanalysis data. For spectral analyses, input data is divided into 1024-day segments unless otherwise noted.

Here, we emphasize that 6-hourly data, rather than daily data, is used in the present study in order to capture the medium-scale waves (Sato *et al.*, 2000). It has been shown that the medium-scale waves, which have timescales shorter than 2 days, play an important role in the annular mode dynamics despite their weak climatological amplitudes (Kuroda and

Mukougawa, 2011).

5.3 Annular mode and eddy-jet feedback

5.3.1 Jet climatology and annular mode structure

We will be focusing on the Southern annular mode in the reanalysis data for simplicity, considering the longitudinal symmetry in the Southern Hemisphere. There are two separate jets in the Southern Hemisphere climatology (Figure 5.1A), namely, the subtropical jet centering around 35°S and the midlatitude jet at around 50°S. Strictly following LH01, the zonal index is defined as the leading principal component (PC) of $\langle [\mathbf{u}] \rangle$, in which the angle brackets denote vertical average. The leading EOF of $\langle [\mathbf{u}] \rangle$ explains 40% of the total variance, while the second EOF explains 20%. Here the zonal index is normalized so that its standard deviation is one. The latitude-pressure pattern of $[\mathbf{u}]$ and $[\mathbf{T}]$ associated with the annular mode in the reanalysis data can be seen by regressing $[\mathbf{u}]$ and $[\mathbf{T}]$ on the zonal index at zero-day lag (Figures 5.1BC). Note that the correlation between the zonal index and the leading PC of $[\mathbf{u}]$ is 0.995, so Figure 5.1B is essentially equivalent to the leading EOF of $[\mathbf{u}]$. The anomalous zonal mean zonal wind associated with the annular mode is characterized by an equivalent barotropic dipole, which is, as expected, in thermal wind balance with the zonal mean temperature anomaly. Variations in the zonal index represent north-south vacillations of the eddy-driven jet (e.g., Hartmann and Lo, 1998).

For model outputs, both hemispheres are analyzed, but the Northern Hemisphere is flipped and plotted as the Southern Hemisphere, as the model is symmetric about the equator. The climatology in the simulations with the same model configuration has been well documented (e.g., Held and Suarez, 1983). In brief, a confined midlatitude jet centering around 40°S, 10° equatorward to the eddy-driven jet in the reanalysis data, is produced in the CTL (Figure 5.2A). The zonal index is again calculated as the leading PC of $\langle [\mathbf{u}] \rangle$. The leading EOF of $\langle [\mathbf{u}] \rangle$ explains 50% of the total variance in the model, while the second EOF explains 18%. Despite the idealized nature of the GCM, the tropospheric dipolar pattern of

zonal wind of the annular mode produced in the model compares reasonably well with the Southern annular mode in the reanalysis data (Figures 5.2BC).

5.3.2 Simple model of feedback

In their seminal work, LH01 introduced a simple model of the eddy-jet feedback, which will be briefly explained in this section. With the same notations as in LH01, $z(t)$ indicates the zonal index, and $m(t)$ denotes the time series of eddy forcing on the annular mode, which is defined as the projection of the anomalous eddy momentum convergence onto the leading EOF of $\langle[\mathbf{u}]\rangle$. As discussed in LH01, the tendency of z is formulated as,

$$dz/dt = m - z/\tau, \quad (5.2a)$$

in which τ is the damping timescale. Equation 5.2a can be interpreted as the zonally and vertically averaged zonal momentum equation (LH01),

$$\frac{\partial \langle[u]\rangle}{\partial t} = \frac{1}{\cos^2 \phi} \frac{\partial (\langle[u'v']\rangle \cos^2 \phi)}{a \partial \phi} - F,$$

where u' and v' are deviations of zonal wind and meridional wind from their respective zonal means, ϕ is the latitude, a is the Earth's radius, and F includes the effects of surface drag and secondary circulation.

With capital letters denoting the Fourier transform of the corresponding lower case variables and ω denoting angular frequency, Equation 5.2a can be written as,

$$i\omega Z = M - Z/\tau \quad (5.2b)$$

Figure 5.3A shows the power spectrum of the zonal index in the reanalysis data, with a lowest resolved frequency of 1/1024 cycles per day (cpd). The zonal index features increasing power with decreasing frequency. At intraseasonal and shorter timescales, where the dominant balance of Equation 5.2b is between $i\omega Z$ and M , the power spectrum of zonal index can be interpreted, to the first order, as reddening of the power spectrum of eddy forcing (Figure 5.3B). The broad peak at synoptic timescale in the power spectrum of eddy

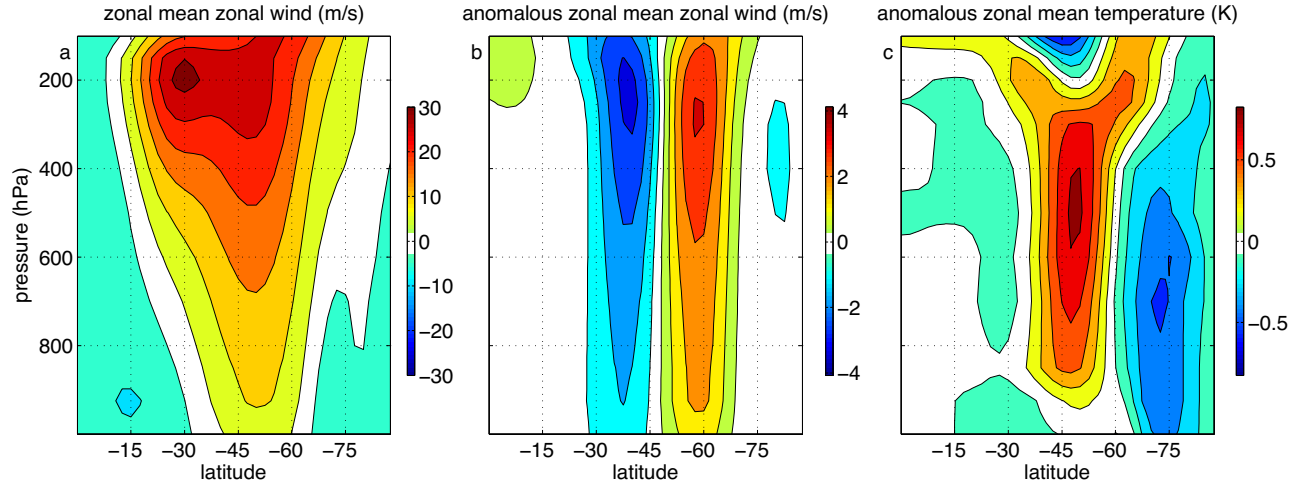


Figure 5.1: (A) Climatology of zonal mean zonal wind in the reanalysis data. Anomalous (B) zonal mean zonal wind and (C) zonal mean temperature regressed on the leading PC of $\langle [u] \rangle$.

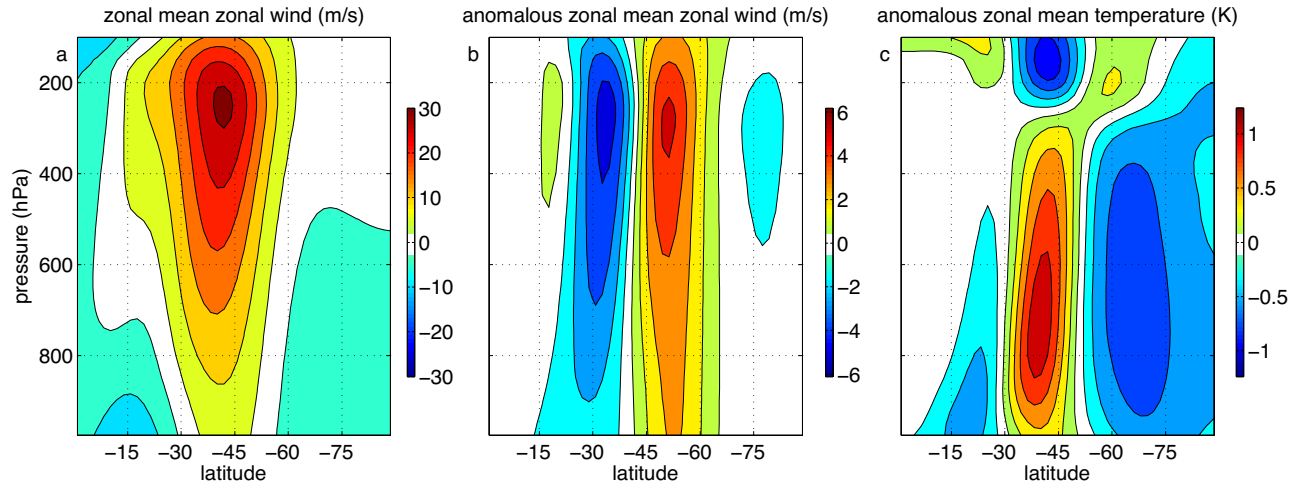


Figure 5.2: The same as Figure 5.1, except for model outputs of CTL.

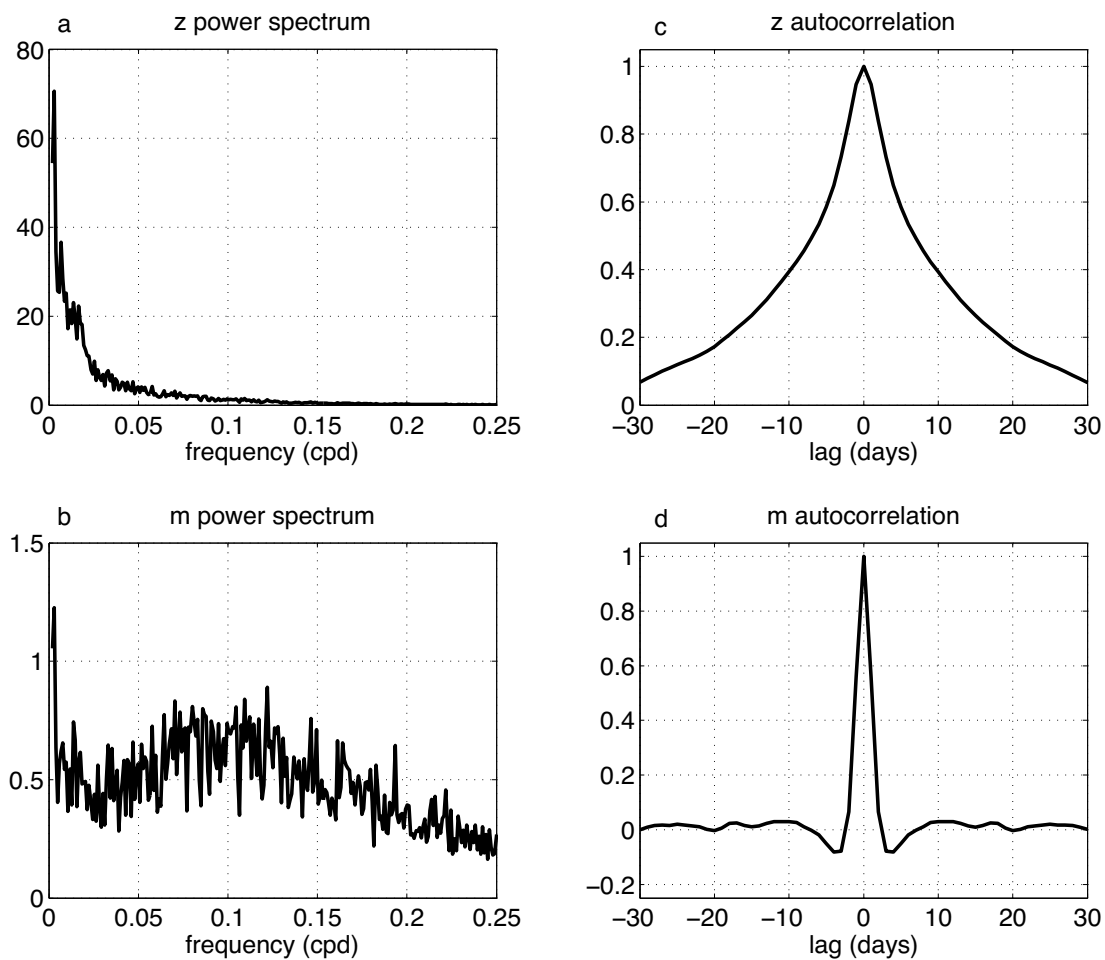


Figure 5.3: Summary statistics for z and m in the reanalysis data. Power spectrum of (A) z and (B) m , and autocorrelations of (C) z and (D) m .

forcing (Figure 5.3C) is an intrinsic characteristic of the mean-state-independent eddies (LH01). At timescales longer than around 50 days, a positive eddy-jet feedback is suggested to be responsible for the high power of both of the zonal index and eddy forcing, where the dominant balance of Equation 5.2b is between Z/τ and M . A linear feedback model for M (e.g., Hasselmann, 1976; LH01) can be written as,

$$M = \tilde{M} + bZ, \quad (5.3)$$

where \tilde{M} is the mean-state-independent eddy forcing, and b is the strength of the eddy-jet feedback. In equilibrium, b must be smaller than $1/\tau$ in both GCMs and the realistic atmosphere, otherwise the zonal index grows unboundedly. Plugging Equation 5.3 into Equation 5.2b returns,

$$i\omega Z = \tilde{M} + (b - 1/\tau)Z \quad (5.4)$$

If we consider \tilde{M} as white noise at low frequencies, the amplitude of Z is inversely proportional to the difference between $1/\tau$ and b at the low-frequency limit (i.e., neglecting the left hand side of Equation 5.4). The stronger the eddy feedback is (i.e., the closer b is to $1/\tau$), the higher power Z has at intraseasonal and longer timescales. Note that if $b = 0$, the amplitude of Z is inversely proportional to $1/\tau$ at the low-frequency limit, and at intraseasonal to interannual timescales the zonal index will still have increasing power with decreasing frequency (Hasselmann, 1976), although the annular mode will be less persistent than that with a positive eddy feedback.

The autocorrelation function of the zonal index decreases more slowly with lag time than that of the eddy forcing (Figures 5.3CD). The negative autocorrelations of eddy forcing at small lag time indicates the quasi-oscillatory nature of the eddies (Figure 5.3D), which is consistent with the broad maximum in the power spectrum at 7-15 days. The cross-correlation of m and z peaks at around 0.53, when the zonal index lags eddy forcing by 1-2 days as the zonal index is driven by the eddy forcing (Figure 5.4). Negative cross-correlations when the zonal index leads eddy forcing by a few days result from the oscillatory behavior

of eddy forcing, and positive values at large lags suggest a positive eddy-jet feedback according to LH01.

Despite some biases, the CTL is able to capture the general features of the system as in the reanalysis data described above (Figure 5.5). The broad peak of eddy forcing at synoptic timescales in the power spectrum is more pronounced in the model, which indicates that the eddy forcing is more oscillatory in the idealized GCM. Chen and Plumb (2009) argued that the shoulders in the autocorrelation function of the zonal index at around ± 4 -day lag can be attributed to the strong oscillatory nature of eddy forcing in the idealized GCM. Also, the annular mode is more persistent in this GCM, as the cross-correlation between m and z decays more slowly compared to that in the reanalysis data (Figures 5.4 and 5.6), or equivalently, the simulated zonal index has higher power at intraseasonal and longer timescales compared to that in the reanalysis data. Note that this is not just a bias of this idealized GCM. Too persistent annular modes are seen in GCMs of varying degrees of complexity, the cause of which is unknown and remains an important topic of research (Gerber *et al.*, 2008a,b; Nie *et al.*, 2014).

5.4 Eddy-jet feedback strength

The LRF will first be used to calculate the ground truth of the eddy-jet feedback strength associated with the leading EOF of $\langle [u] \rangle$ (i.e., the annular mode), as well as the second EOF, in the idealized GCM. Three different statistical methods, namely, fitting cross-correlation functions (LH01), lag regression (S13) and regression using low-pass filtered data (introduced in the present study), will be used to estimate the eddy feedback strength of the annular mode in the idealized GCM, and evaluated against the result from the LRF. Then we will apply the statistical methods to investigate the eddy feedback associated with the annular mode in the reanalysis data.

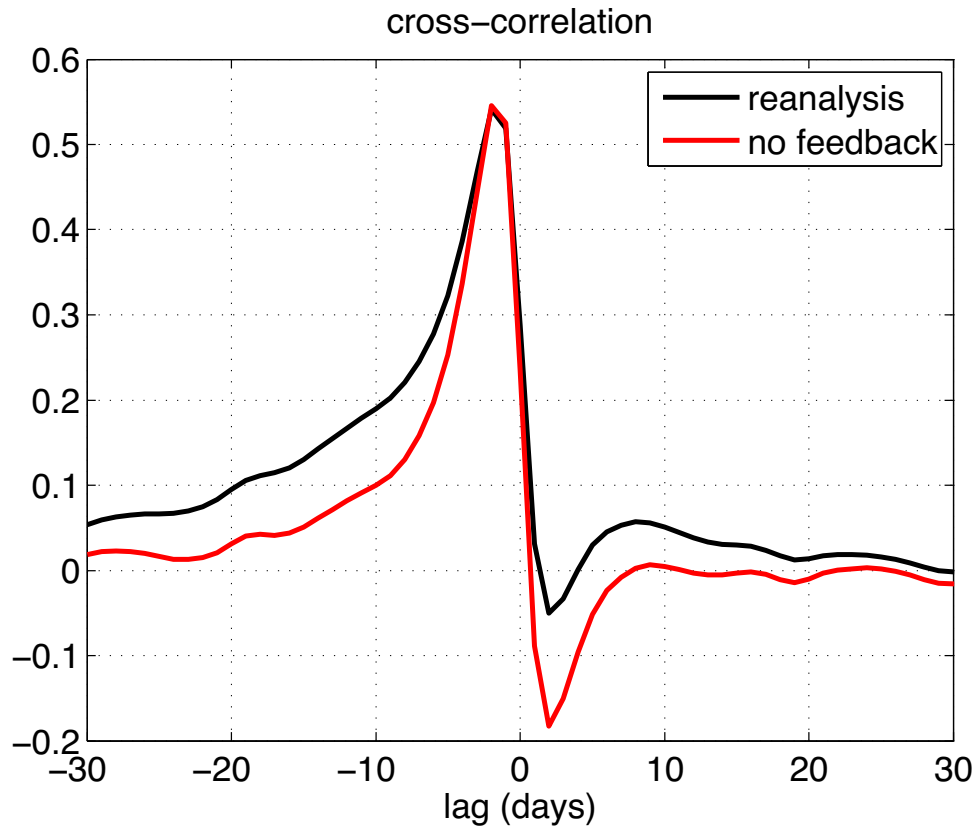


Figure 5.4: Cross-correlation between z and m in the reanalysis data (black curve), and between \tilde{z} and \tilde{m} (i.e., without eddy feedback following LH01). Positive values of lag denote that zonal index leads eddy forcing.

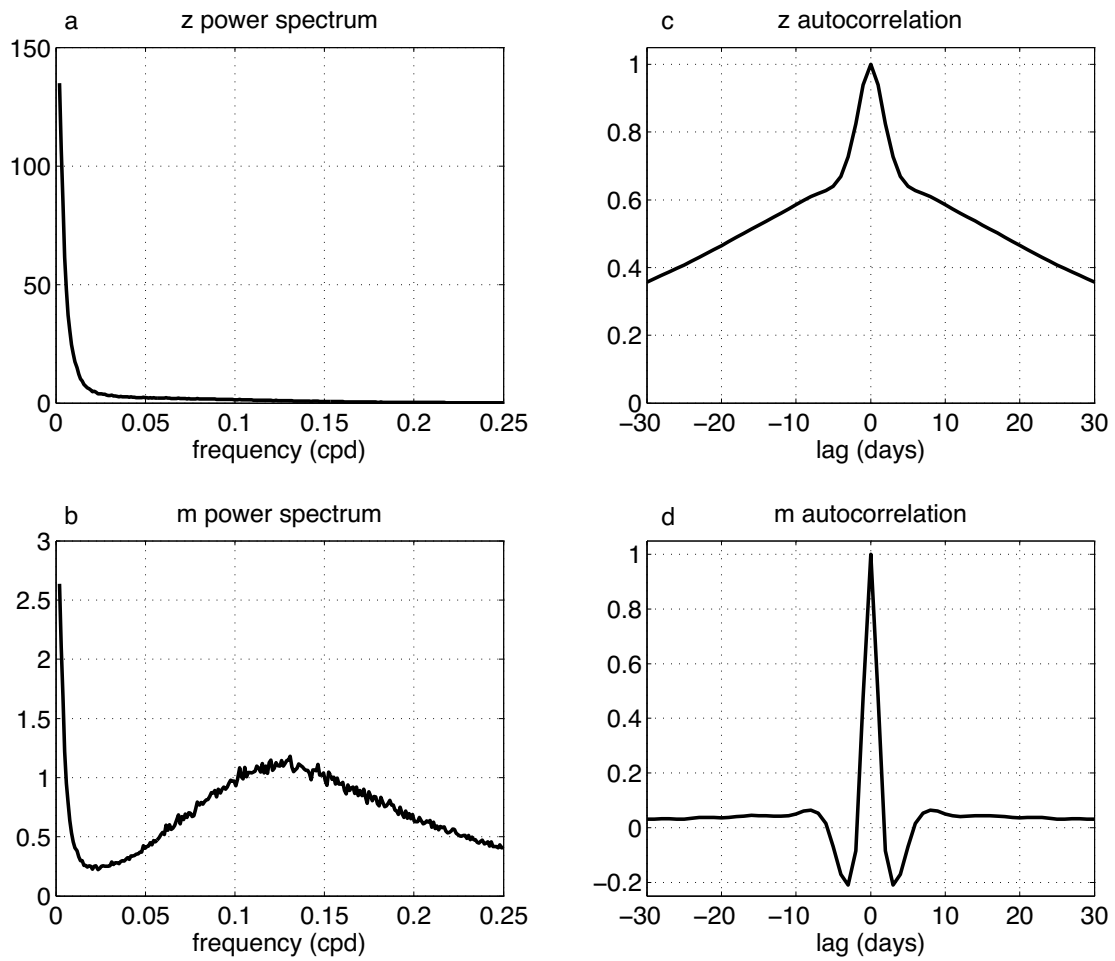


Figure 5.5: The same as Figure 5.3, except for model outputs of CTL.

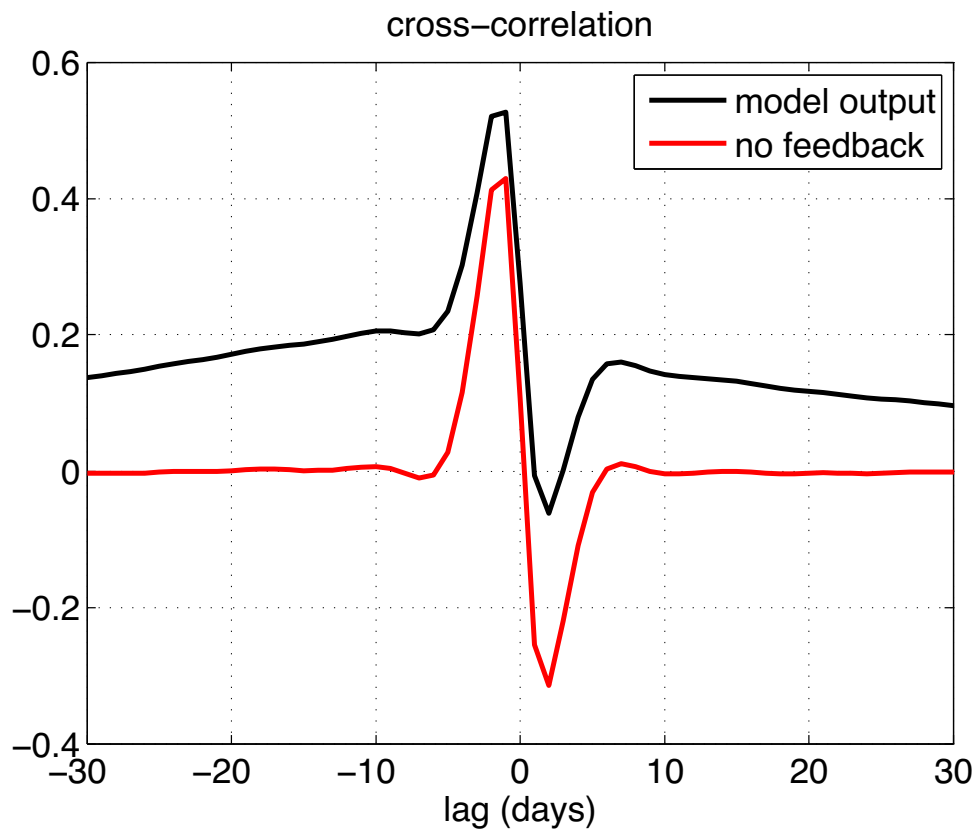


Figure 5.6: *The same as Figure 5.4, except for model outputs of CTL.*

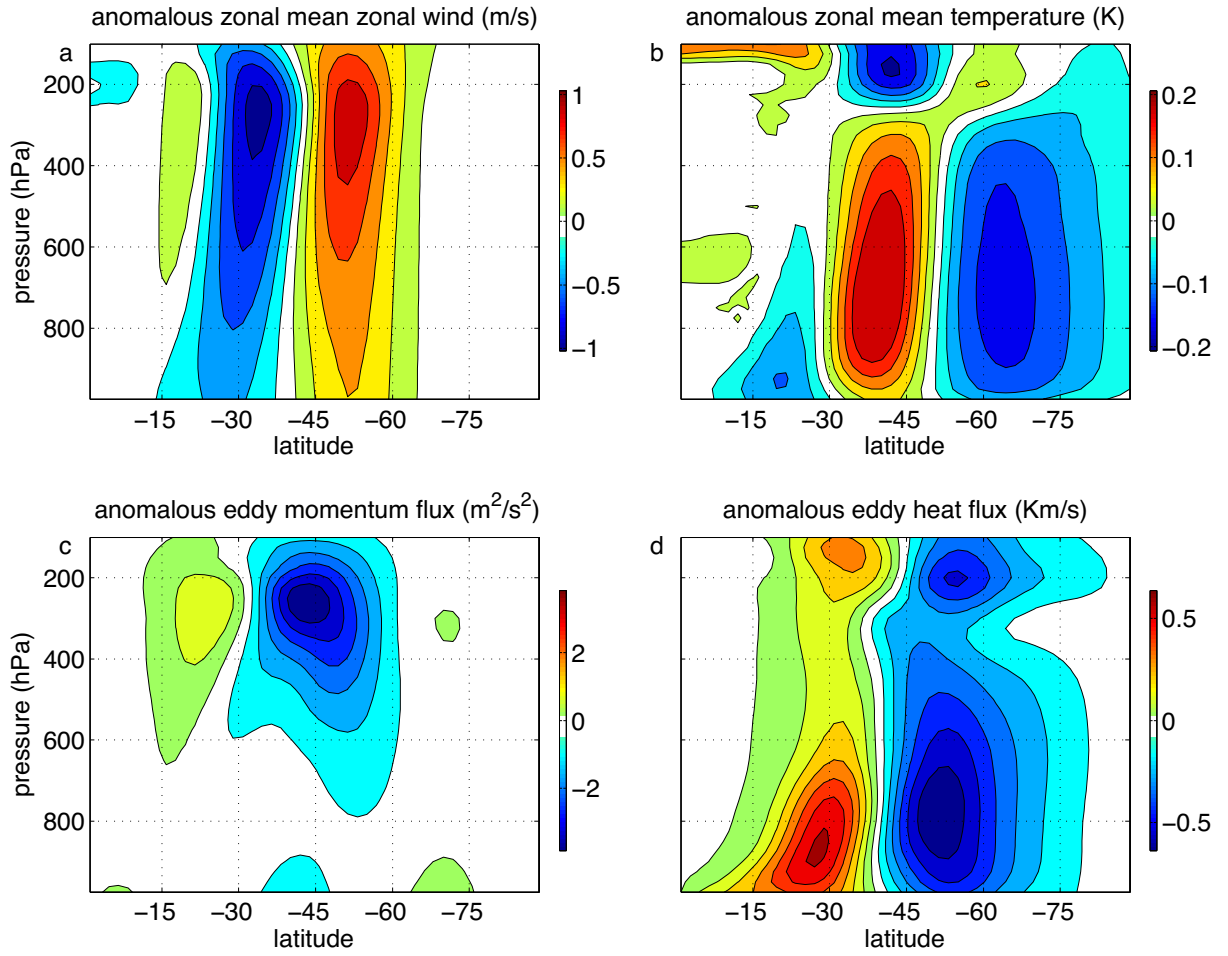


Figure 5.7: The difference of (A) zonal mean zonal wind, (B) zonal mean temperature, (C) zonal average eddy momentum flux and (D) zonal average eddy heat flux between EXP and CTL.

5.4.1 Linear response function

With a zonally symmetric time-invariant forcing, the deviations of mean state in EXP from that in CTL (Figures 5.7AB) are nearly identical to the pattern of the annular mode (Figures 5.2BC), with a pattern correlation of 0.995. Note that the changes in the mean state from CTL to EXP are caused by the imposed external forcing and are long term averages so that the eddies are in statistical equilibrium with the mean state. The changes of eddy fluxes from CTL to EXP are the response to the mean state changes, rather than the cause of the deviation of the mean state. The anomalous eddy fluxes are shown in Figures 5.7CD, the pattern of which largely agrees with LH01. In the region of positive zonal wind anomalies (around 50°), meridional temperature gradient increases at low levels (Figures 5.7AB), leading to enhanced baroclinic wave generation and stronger eddy heat flux (Figure 5.7D). Correspondingly, the equatorward propagation of waves enhances the poleward eddy momentum flux at around 45° , which reinforces the zonal wind anomaly (Figure 5.7D). The strength of the eddy feedback can be calculated by projecting the anomalous eddy momentum flux convergence onto the anomalous zonal wind (see Baldwin *et al.*, 2009 for details about projection of data with spatial weighting). The averaged feedback strength of the 10 ensemble simulations (referred to as b_{LRF} hereafter) is around 0.137 day^{-1} , which is denoted by the red solid line in Figure 5.8. The red dashed lines in Figure 5.8 show the 95% confidence intervals of b_{LRF} , indicating little spread across the ensemble members. b_{LRF} is considered as the ground truth in the idealized GCM.

The mean-state-independent eddy forcing is not directly observable and cannot be separated from the mean-state-dependent eddy forcing in the reanalysis data, but can be computed in the idealized GCM as $\tilde{M} = M - b_{LRF}Z$. The power spectrum of the mean-state-independent eddy forcing is shown in Figure 5.9. At timescales shorter than around 50 days, the mean-state-independent eddy forcing dominates the total eddy forcing. In particular, it is confirmed that the mean-state-independent eddy forcing is responsible for the broad peak of total eddy forcing at synoptic timescales. At timescales longer than 50 days, the strength of the mean-state-independent eddy forcing decreases with decreasing frequency, while the

strength of the total eddy forcing rises as frequency decreases.

At intraseasonal to interannual timescales, the total eddy forcing is dominated by mean-state-dependent eddy forcing. Here, the role of the medium-scale waves, whose period is shorter than 2 days, in the annular mode dynamics is emphasized. It has been shown that the amplitude of the medium-scale waves, which is weak in the climatology, is strongly modified by the annular mode, and the fluxes resulting from these waves have a substantial contribution to the annular mode dynamics (Kuroda and Mukougawa, 2011). At interannual timescales, the total eddy forcing calculated from daily wind anomalies captures less than half of the total eddy forcing calculated from 6-hourly wind anomalies in the idealized GCM (Figure 5.10A). The results suggest that the eddy-jet feedback will be strongly underestimated without accounting for medium-scale waves. In fact, with daily model outputs, b_{LRF} is around 0.083 day^{-1} , 40% weaker than that calculated using 6-hourly model outputs.

Although the focus of the present work is on the annular mode (i.e., the leading EOF of the zonal mean zonal wind), we also apply the LRF framework to the second EOF, which is characterized by a tripolar pattern of zonal wind anomalies and corresponds to the fluctuations of the amplitude of the jet (Figure 5.11A). With a stronger midlatitude jet, temperature gradient is enhanced between 30°S - 40°S below around 300 hPa (Figure 5.11B). Poleward eddy heat flux is strengthened due to sharper temperature gradient (Figure 5.11D), and the anomalous eddy momentum flux associated with second EOF tends to export momentum out of the jet (Figure 5.11C). Using another ensemble of 10 simulations with an external forcing calculated for the second EOF, it is found that the eddy feedback associated with the second EOF is negative, and the strength of the feedback is -0.264 day^{-1} . This is consistent with the findings of LH01, who inferred from a lag-regression analysis that the feedback is negative. LH01 also argued that the anomalous eddy momentum flux associated with the second EOF tend to weaken the jet as a result of increased barotropic shear, i.e. the barotropic governor effect (James, 1987).

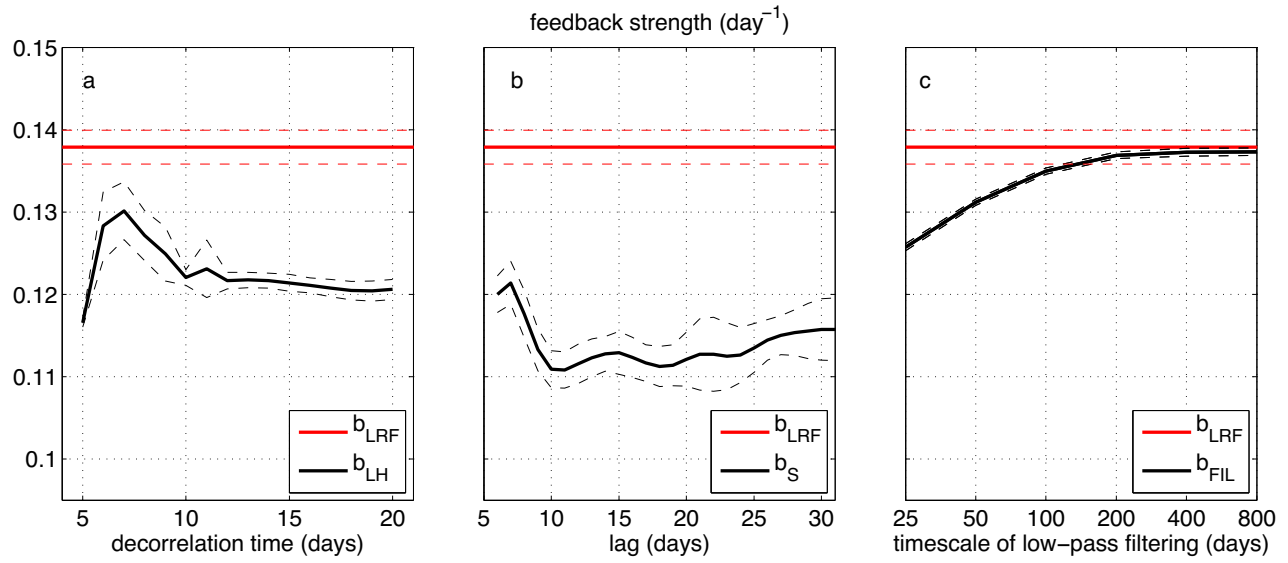


Figure 5.8: Strength of eddy-jet feedback estimated in the idealized GCM following different methods: (A) LH01, (B) S13 and (C) low-pass filtering. The red lines in each panel shows the value calculated using the LRF. The dashed lines denoting 95% confidence intervals

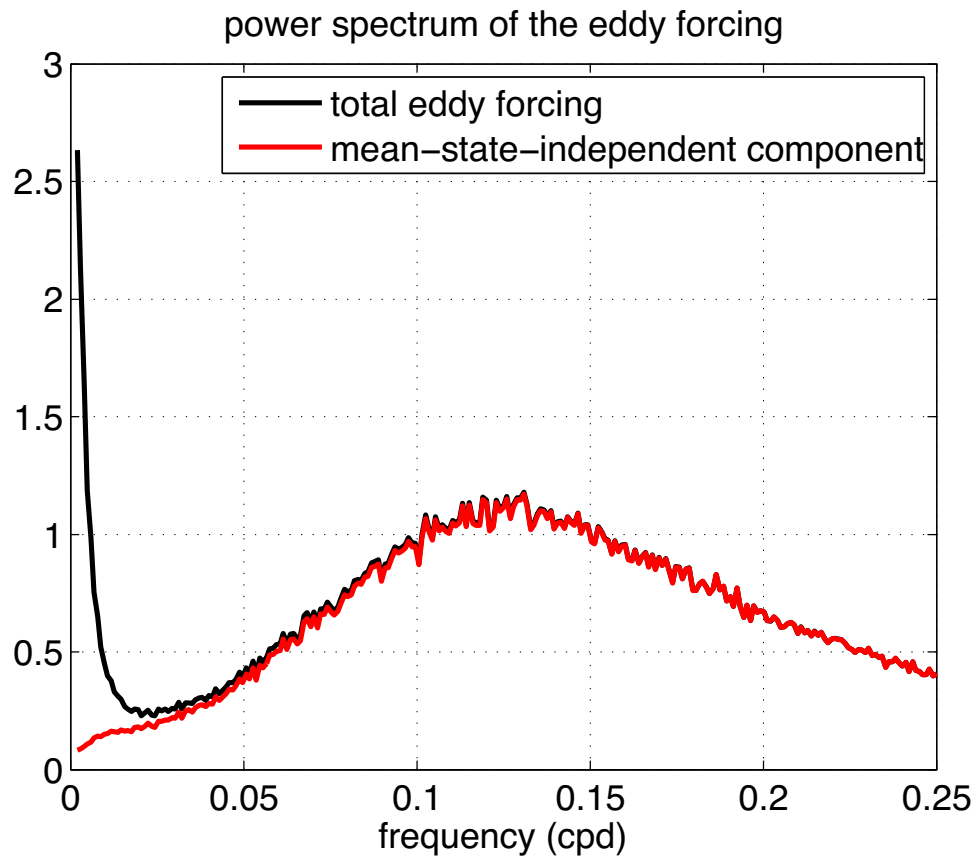


Figure 5.9: Power spectrum of the total eddy forcing (black) and the mean-state-independent eddy forcing (red).

5.4.2 Fitting cross-correlation functions

In a pioneering study, LH01 inferred the existence of a positive eddy-jet feedback in the annular mode dynamics from the reanalysis data and based on the the assumption that the mean-state-independent eddy forcing has short memory (i.e., the time series of \tilde{m} has a short decorrelation timescale), and proposed the following method to quantify the strength of the feedback by fitting the covariance functions. If $b = 0$, Equation 5.4 becomes,

$$i\omega\tilde{Z} = \tilde{M} - \tilde{Z}/\tau, \quad (5.5)$$

where \tilde{Z} denotes the zonal index in a system without eddy-jet feedback. The covariance between \tilde{z} and \tilde{m} must be close to zero when \tilde{z} leads \tilde{m} by a period longer than the decorrelation timescale of the mean-state-independent eddies. It has been shown that the covariance between \tilde{z} and \tilde{m} is a function of b and the covariance between z and m (see LH01 for details), and b can be estimated by minimizing the mean squared cross-correlations at lags longer than a particular decorrelation timescale. For instance, assuming a decorrelation time of 7 days, the estimated strength of eddy-jet feedback (hereafter b_{LH}) is around 0.13 day^{-1} , and the red curve in Figure 5.6 shows the corresponding cross-correlations between \tilde{z} and \tilde{m} . Bootstrap confidence intervals (at 95% confidence levels) are plotted to indicate errors (black dashed curves in Figure 5.8A). A bootstrap ensemble of 5000 members is constructed by resampling from the original time series. Feedback strength is calculated for each of the bootstrap ensemble member, which provides the probability density function of b_{LH} and thus the confidence intervals. b_{LH} varies with the choices of decorrelation time. Note that it is difficult to determine an optimal decorrelation time *a priori* due to the quasi-oscillatory behavior of \tilde{m} , especially when the decorrelation timescale varies by season (e.g., Sheshadri and Plumb, 2016).

5.4.3 Lag regressions

Lag regression is applied to find the feedback strength following S13. Denote the auto-covariance function of z with lag l as $\gamma_z(l)$, and write the cross-covariance function between

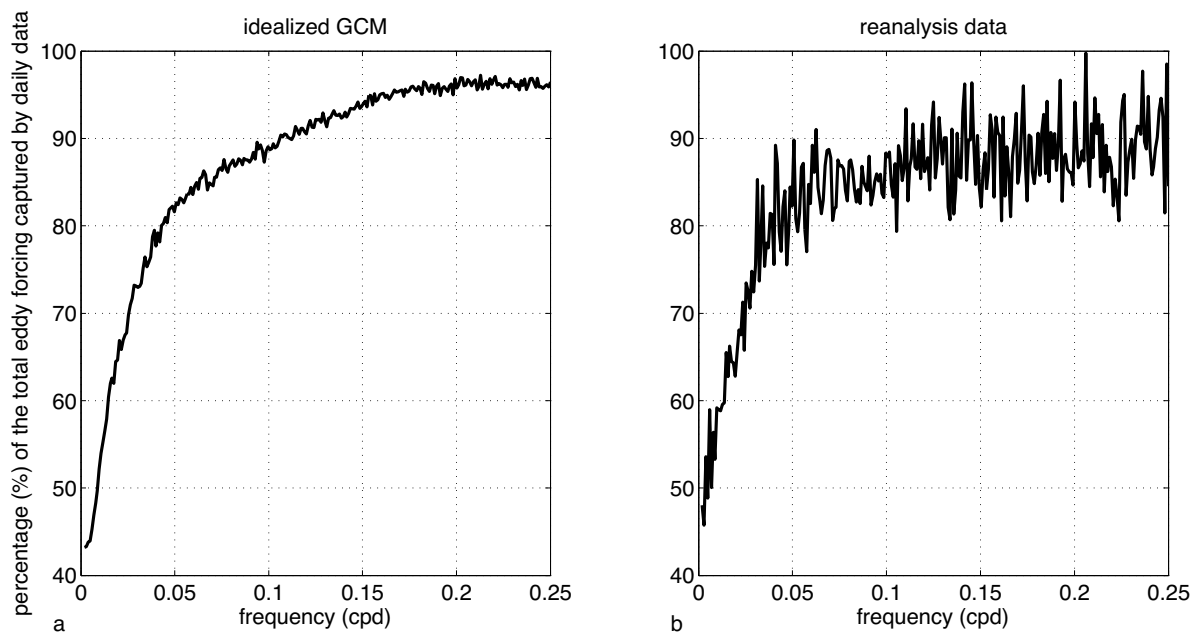


Figure 5.10: The ratio between the total eddy forcing calculated from daily wind anomalies and that calculated from 6-hourly wind anomalies for (A) model outputs of CTL and (B) the reanalysis data.

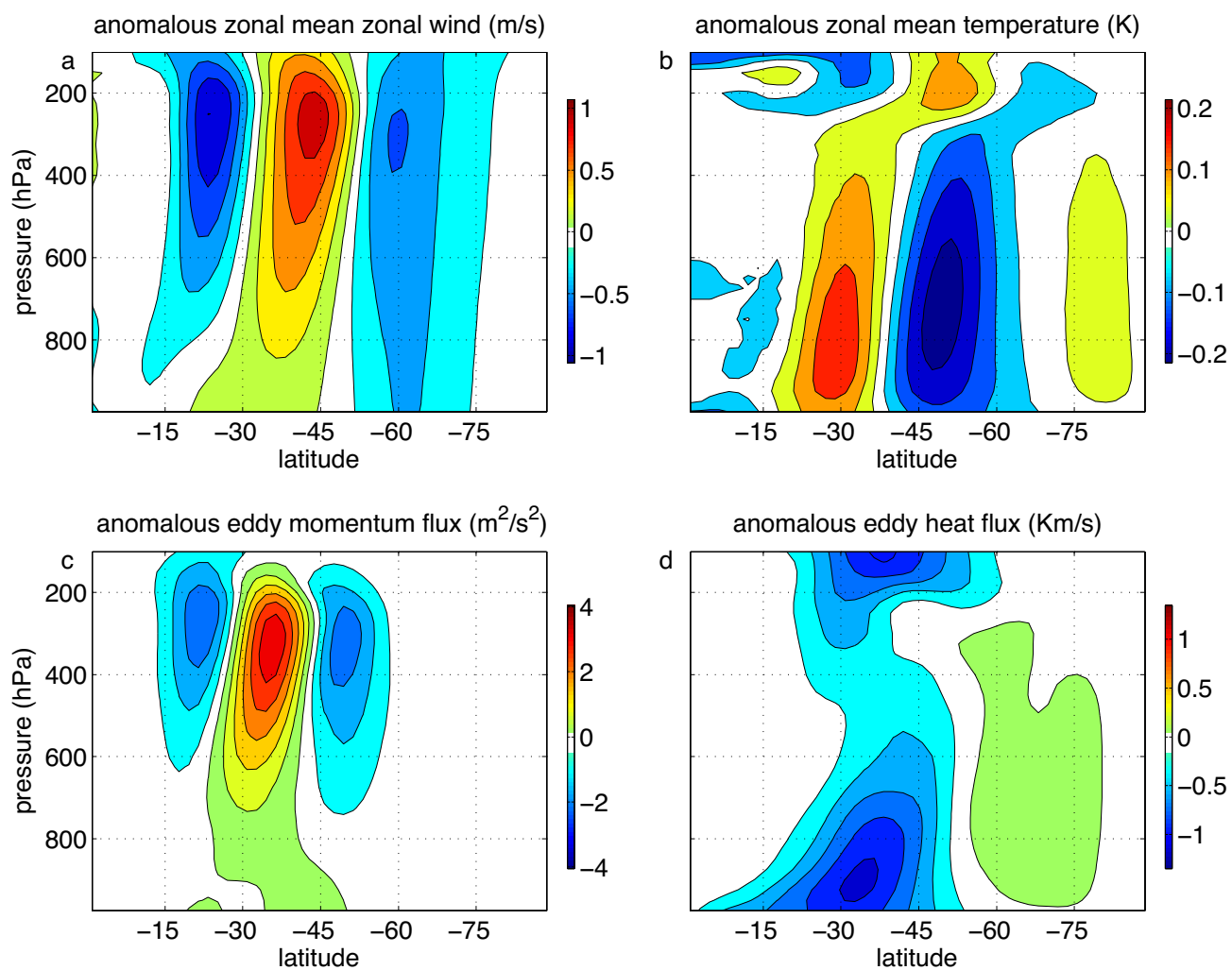


Figure 5.11: The same as Figure 5.7, except for the second EOF of zonal mean zonal wind.

z and m as $\gamma_{zm}(l)$ when z leads m by l days. Consider the lag regression model $m(t) = \beta(l)z(t-l)$, the lag regression coefficient β is,

$$\beta(l) = \frac{\gamma_{zm}(l)}{\gamma_z(0)} \quad (5.6)$$

With Equation 5.3, the right hand side of Equation 5.6 can be decomposed into two parts:

$$\beta(l) = \frac{\gamma_{z\tilde{m}}(l)}{\gamma_z(0)} + b \frac{\gamma_z(l)}{\gamma_z(0)}, \quad (5.7)$$

in which the first term on the right hand side is negligible if z is decorrelated with \tilde{m} beyond lag l days, and therefore the feedback strength can be estimated as,

$$b_S = \beta(l) \frac{\gamma_z(0)}{\gamma_z(l)} \quad (5.8)$$

Figure 5.8B shows the strength of eddy-jet feedback calculated using Equation 5.8, with 95% confidence intervals estimated with bootstrapping as in Section 5.4.2. While the margin of error grows with lag time, the strength of eddy-jet feedback is largely underestimated, and the bias results from the quasi-oscillatory nature of the eddy forcing. Using lag regression, we are also able to estimate the pattern of anomalous eddy fluxes associated with the annular mode. The pressure-latitude distribution of eddy flux anomaly generally agrees with the results from LRF, with a pattern correlation over 0.9 through a wide range of lag days (figures not shown).

5.4.4 Low-pass filtering

The bias with lag regression suggests that the correlation between \tilde{m} and z is not negligible relative to the correlation between m and z at a lag as long as 30 days (Figure 5.8B). One can expect that at longer lag timescales, \tilde{m} and z eventually become decorrelated and thus Equation 5.8 will be valid, but it can also be expected that with such long lag time, the margin of error will be large so that the estimation is uninformative. Inspired by the observation that the strength of the mean-state-independent eddy forcing vanishes at the low-frequency limit (Figure 5.9), here we propose a new method to bypass this issue.

Multiplied by $Z^*/(ZZ^*)$ on both sides, where Z^* denotes the conjugate of Z , Equation 5.3 becomes:

$$\frac{MZ^*}{ZZ^*} = \frac{\tilde{M}Z^*}{ZZ^*} + b \quad (5.9)$$

Using the LRF, the real component of the first term on the right hand side can be explicitly calculated and is found to be negligible at the low-frequency limit (Figure 5.12). As a result, the feedback strength equals the real component of the left hand side of Equation 5.9 at the lowest frequencies, which can be calculated as the regression coefficient of low-pass filtered m on low-pass filtered z . In practice, Lanczos filtering is applied with the number of weights covering the length of four times of the cut-off periods. The estimated feedback strength (denoted as b_{FIL}) is plotted in Figure 5.8C. When timescales longer than 200 days are used for the low-pass filtering, this method yields remarkably accurate results. b_{FIL} is calculated for each hemisphere of the 10 ensemble members of CTL, and 95% confidence intervals are then calculated assuming these samples follow Gaussian distribution. The pressure-latitude pattern of eddy flux anomaly associated with the annular mode is also constructed by regressing low-pass filtered eddy fluxes onto the low-pass filtered zonal index, and the results compares well with those from LRF, with a pattern correlation exceeding 0.9.

5.4.5 Application to the reanalysis data

The above three statistical methods are applied to estimate the strength of eddy-jet feedback in the reanalysis data, and the results are summarized in Figure 5.13.

By minimizing the mean squared cross-correlations at lags longer than certain number of days as illustrated in Figure 5.4, b_{LH} spans a range of values from around 0.06 to 0.12 day^{-1} with the choices of decorrelation timescales of 5-20 days. The estimation for the reanalysis data is more sensitive to the choices of decorrelation and has larger margin of error compared to that of the idealized GCM (Figure 5.13A), which may partly be attributed to the shorter temporal length of the reanalysis data. Using lag regression, the estimated feedback strength is a function of lag days, and the margin of error grows with increasing

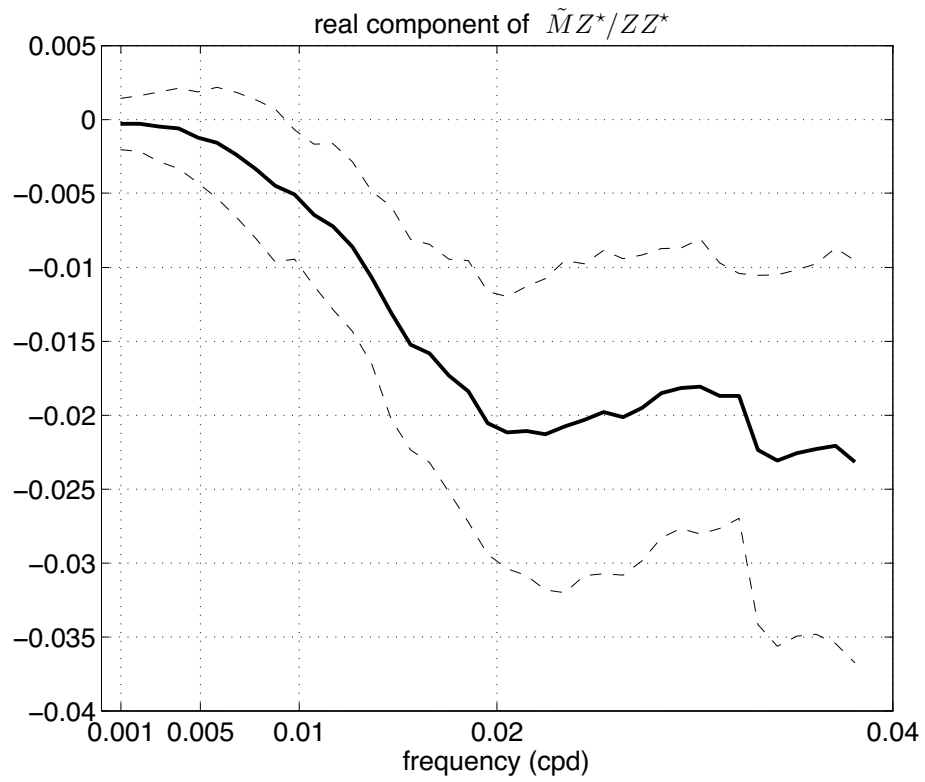


Figure 5.12: Real component of $\frac{\tilde{M}Z^*}{ZZ^*}$ in CTL, with the dashed curves denoting 95% confidence intervals.

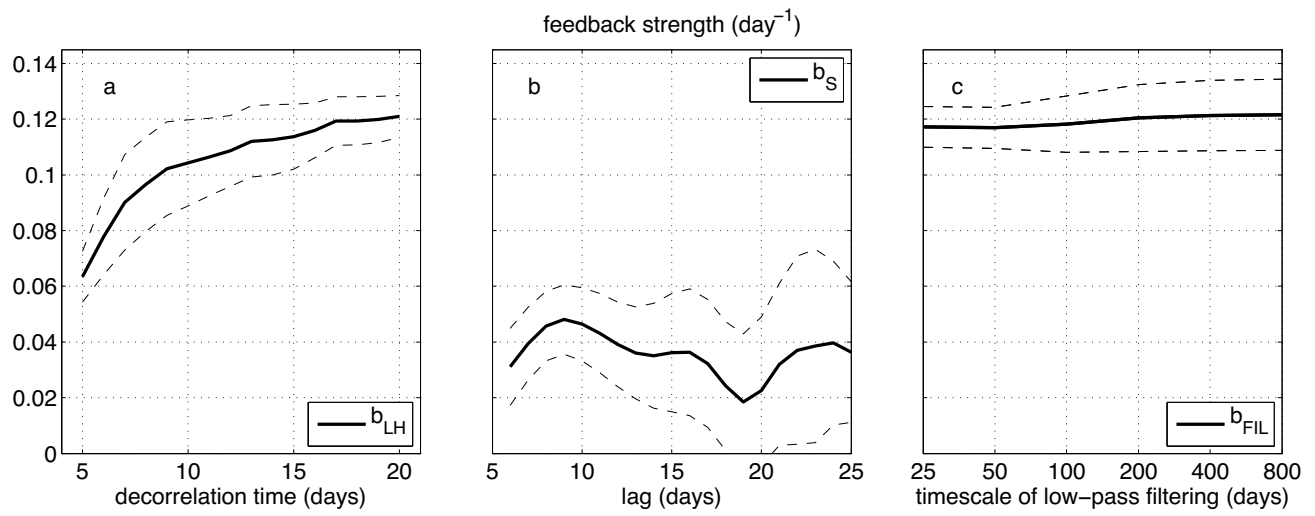


Figure 5.13: Similar to Figure 5.8, except for the reanalysis data.

lag (Figure 5.13B). Also, b_S is more sensitive to the choices of lag days and has larger uncertainties than its counterpart with model outputs.

Although there is no ground truth for the reanalysis data, the result obtained from regression with low-pass filtered data seems encouraging (Figure 5.13C). b_{FIL} converges to around 0.121 day^{-1} at low-frequency limit, which matches well with b_{LH} with the decorrelation time of around 2 weeks. There is also a significant contribution of medium-scales waves to total eddy forcing at intraseasonal to interannual timescales in the reanalysis data (Figure 5.10B), and with daily data, b_{FIL} is only around 0.053 day^{-1} . The pattern of anomalous eddy fluxes associated with the annular mode is also calculated by regressing low-pass filtered time series (Figure 5.14). As expected, anomalous eddy flux converges zonal momentum into 60°S - 70°S in the upper troposphere, and reinforces the anomalous zonal wind. Eddy anomalies originate from 60°S - 75°S near the surface, where eddy heat flux is strengthened due to increased baroclinicity.

While we do not have the LRF to separate out the mean-state-independent eddy forcing in the reanalysis, the low-pass filtering method only assumes that the mean-state-independent eddy forcing is sufficiently weak at the low-frequency limit so that the first term on the right hand side of Equation 5.9 is substantially smaller than the feedback factor b . Given that eddies are mostly generated at synoptic timescales, this seems a rather reasonable assumption. A caveat of this assumption is that in the presence of an external low-frequency forcing (for example, due to stratospheric variability), the mean-state-independent eddy forcing might not be small at low frequencies (see an illustrative example in Byrne *et al.* (2016) and more discussions in the next section).

5.5 Discussions and summary

The temporal persistence of the atmospheric annular mode has long been attributed to a positive eddy-jet feedback (e.g., Feldstein and Lee, 1998; Robinson, 2000; LH01), and statistical methods have been used to quantify the strength of the eddy feedback (LH01; S13). However, a recent study argues that one cannot discern the difference between the presence

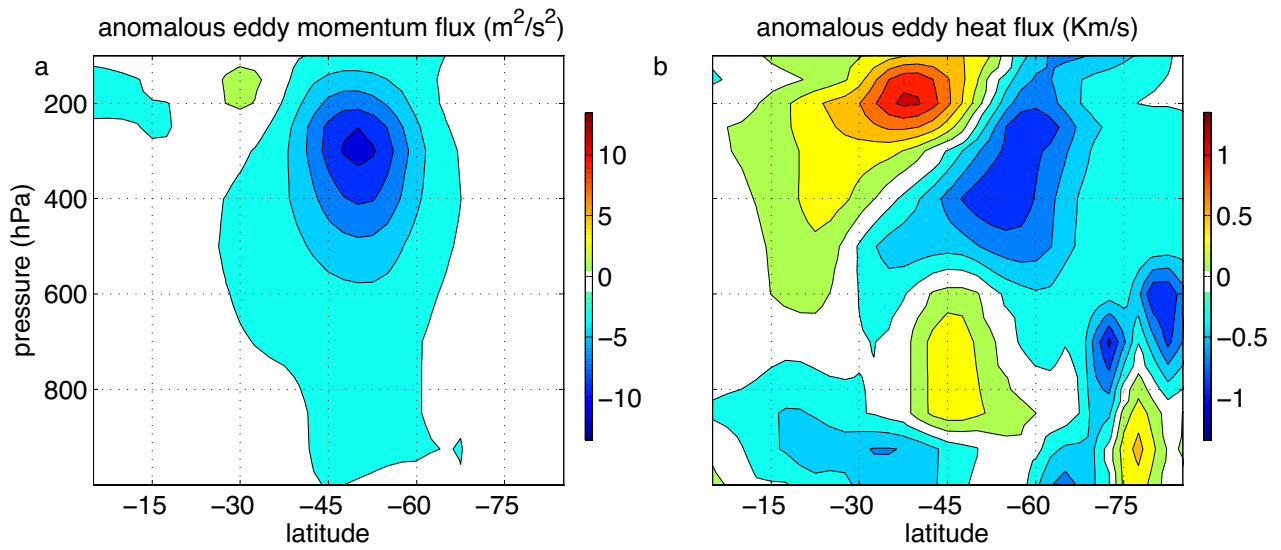


Figure 5.14: Anomalous zonal average (A) eddy momentum flux and (B) eddy heat flux associated with the Southern annular mode in the reanalysis data.

of an internal eddy feedback and external interannual forcing using only the statistical methods (Byrne *et al.*, 2016). Due to the stochastic nature of eddies, it is indeed impossible to separate the mean-state-dependent eddy flux from the mean-state-independent eddy flux and infer causality in the reanalysis data. In the present study, an LRF is used to identify the eddy response to anomalous mean flow associated with the annular mode in an idealized GCM, in which a positive eddy-jet feedback is confirmed unequivocally. With little spread across ten 44500-day integrations, EXP yields an eddy feedback strength of around 0.137 day^{-1} . When the LRF is applied to the second EOF of zonal mean zonal wind, it yields a negative eddy feedback of -0.264 day^{-1} , consistent with the findings of LH01 who inferred the existence of a negative feedback in the second EOF of the observed Southern annular mode and attributed it to the barotropic governor effect (James, 1987).

Using the LRF, the present study is able to provide a reasonably accurate estimation of the mean-state-independent eddy forcing. It is found that the spectral peak at synoptic timescales in the power spectrum of total eddy forcing (m) is dominated by the mean-state-independent eddy forcing (\tilde{m}). At intraseasonal and longer timescales, the amplitude of the mean-state-independent eddy forcing decreases with decreasing frequency, and the total eddy forcing is dominated by mean-state-dependent eddy forcing. The role of the medium-scale waves on the annular mode is emphasized in the present study, which shows that less than half of the total eddy forcing can be captured using daily wind anomalies at interannual timescales as reported before in Kuroda and Mukougawa (2011). Without accounting for the medium-scales waves, the eddy feedback strength is underestimated by around 40%.

The present study focuses on an equinoctial mean state in the idealized GCM. While a number of previous studies (e.g., Barnes and Hartmann, 2010; Byrne *et al.*, 2016; Sheshadri and Plumb, 2016) have brought attention to the seasonality of the annular mode. Seasonal variations of the persistence of the annular mode and eddy-jet feedback will be explored using the present methodology in a future study.

The statistical methods proposed by LH01 and S13 are evaluated against the result from

the LRF. By fitting the cross-correlations between the zonal index and eddy forcing as in LH01, the estimated feedback strength is fairly close to the result from the LRF, but it is difficult to determine *a priori* an optimal value of decorrelation timescales, a parameter needed to calculate the best-fit. Following S13, the output from lag-regression varies with lag days, and the feedback strength is largely underestimated, which suggests that the estimator is biased, and the assumption of S13 that the zonal index is decorrelated with the mean-state-independent eddy forcing beyond a lag time of a few days is not valid. To be specific, the correlation between \tilde{m} and z cannot be neglected with a lag time spanning from a few days to as long as 30 days, as the mean-state-independent eddy forcing is quasi-oscillatory, with a broad peak in the power spectrum at synoptic timescale.

To reduce the interference from the spectral peak of eddy forcing at synoptic timescales, we applied regressions on low-pass filtered eddy forcing and zonal index. The results converge to the value produced by the LRF when timescales longer than 200 days are used for the low-pass filtering. Given that the left hand side of Equation 5.4 is negligible at the low frequency limit, the fact that the power of the mean-state-independent eddy forcing is low at low frequencies implies that b and $1/\tau$ are close to each other. The difference between $1/\tau$ and b , denoted as $1/\tau_e$, is constrained by examining $|Z/\tilde{M}|$, which can be derived from Equation 5.4:

$$\left| \frac{Z}{\tilde{M}} \right| = \left| \frac{1}{i\omega - 1/\tau_e} \right| = \frac{1}{\sqrt{\omega^2 + 1/\tau_e^2}} \quad (5.10)$$

Taking advantage of the length of CTL, spectral analysis is conducted at very fine spectral resolution, i.e., 1/10000 cpd as in Figure 5.15. At intraseasonal and shorter timescales, when $1/\tau_e$ is small compared to ω , $|Z/\tilde{M}|$ is close to the $1/\omega$ curve (Figure 5.15). At the lowest frequencies, $|Z/\tilde{M}|$ is limited by τ_e . The best-fit value of τ_e is 91 days from least squares fitting. The difference between $1/\tau$ and b is smaller than 0.011 day^{-1} . The result is robust as $1/\tau_e$ ranges from 0.009 to 0.014 day^{-1} when we applied least squares fitting to the ten ensemble members of CTL. It leaves an intriguing question as to what physical processes determine the difference between $1/\tau$ and b , as $1/\tau$ and b are connected, for example, via

surface friction (Chen and Plumb, 2009).

When the statistical methods are applied to the reanalysis data, the performance of the methods proposed by LH01 and S13 is influenced by the mean-state-independent eddy forcing. For the reanalysis data, b_{LH} and b_S are more sensitive to the choices of parameters compared to their counterparts with model results. When the synoptic spectral peak is filtered out by low-pass filtering, with timescales longer than 200 days used for the low-pass filtering, b_{FIL} converges to around 0.121 day^{-1} , which is close to the strength of eddy feedback in the idealized GCM.

Although we cannot deny the presence of external eddy forcing at interannual timescale in the reanalysis data and its contribution to the persistence of the annular mode as suggested by Byrne *et al.* (2016), the present study confirms the importance of a positive eddy-jet feedback to the persistence of the annular mode in an idealized GCM. The annular mode in this GCM compares well with that in reanalysis data, in terms of the spatial pattern of the leading EOF and the statistics of the zonal index and eddy forcing. The resemblance between the simulated annular mode and that in the reanalysis data suggests that the dry dynamical core with Held-Suarez physics, despite its idealized nature, is able to capture the essential dynamics of the annular mode. However, it should also be highlighted that the idealized model indeed produces a too persistent annular mode compared to the reanalysis. The eddy feedback is too strong in the idealized GCM, and it can be inferred that the difference between $1/\tau$ and b is too small in the model. To what extent the results of the idealized GCM connect to the real atmosphere requires further research using observational data and a hierarchy of models.

In addition, the present article provides another application of the LRF (Hassanzadeh and Kuang, 2015, 2016a,b). To quantify the strength of the eddy-jet feedback, one must be able to separate the anomalous eddies in response to a mean flow anomaly from the anomalous eddies that leads to the mean flow anomaly, which is difficult to do with statistical methods alone. Here the LRF is used to untangle the causal relationship in this eddy-jet feedback system, and provides the ground truth in the idealized GCM. Statistical

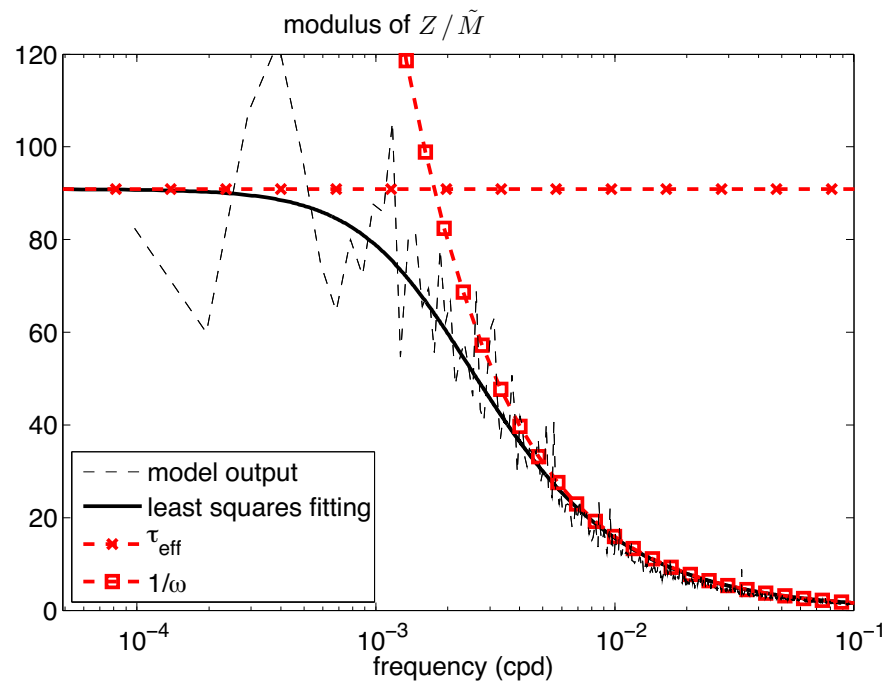


Figure 5.15: Modulus of Z / \tilde{M} from model outputs (black dashed curve) and least squares fitting (black solid curve) for model outputs of CTL.

methods are evaluated using model outputs, and then applied to the reanalysis data. The LRF can be calculated for GCMs of varying complexities, and the paradigm can be applied to a variety of problems involving identification of internal feedbacks.

Chapter 6

Summary and future directions

This work covers the investigations of three dominant patterns of large-scale circulation variability in the atmosphere, namely the South Asian summer monsoon, the Madden-Julian Oscillation (MJO) and the annular mode. Beside intense scientific interests, these phenomena have tremendous societal impacts. Numerical simulations and observational analysis have been applied to pursue a better theoretical understanding of these systems.

6.1 South Asian summer monsoon

The classic view about the South Asian summer monsoon holds that the Tibetan Plateau drives a strong monsoon as an elevated heat source (e.g., Yeh *et al.*, 1957; Li and Yanai, 1996), which is challenged by new interpretations of observations with modern theories (see review by Boos, 2015). Under the framework of convective quasi-equilibrium (CQE), it is argued that the orography creates a strong monsoon mainly by insulating the thermal maximum from extratropical air (e.g., Boos and Kuang, 2010).

Here, the role of the orography on South Asian monsoon is comprehensively examined with state-of-the-art numerical modeling. Altered orography and surface flux perturbations are applied in numerical simulations using a global model with 40 km horizontal resolution, which resolves the narrow Himalayan mountains and is finer than that in previous studies. To avoid the uncertainties from parameterized convection, large-scale circulations and

convective motions are rescaled following Kuang *et al.* (2005), so that convection is allowed to be represented explicitly at such horizontal resolution. It is confirmed that the monsoon strength is not sensitive to the orography and surface heating perturbations north of the Himalayas, and the results show that the monsoon strength is almost linearly related with the height of the Himalayas with no threshold behavior. Moreover, despite the high correlations between the monsoon strength and the maximum sub-cloud moist entropy, that free-tropospheric moisture anomaly leads to deviations from strict CQE, implying complexities that need to be included in existing theories of monsoon strength.

The focus of the present study is on the mature phase of the monsoon. Meanwhile, the onset of the South Asian monsoon is found to be substantially delayed without global orography, and it has been argued that the heating and mechanical impact of Tibetan Plateau are important to monsoon onset based on statistical analysis and numerical simulations (e.g., Park *et al.*, 2012; Rajagopalan and Molnar, 2013), which leaves an open question regarding the role of the orography on monsoon onset. Recent studies have advanced the understanding of the abrupt onset of monsoons in general, as simple theories building on reanalysis data and idealized general circulation models were proposed, emphasizing the roles of transient eddies, meridional advection, surface flux and stationary waves (e.g., Boos and Emanuel, 2009; Schneider and Bordoni, 2008; Shaw, 2014). There is still a gap between these simple theories and the realistic South Asian monsoon onset. In addition, the MJO, equatorial waves and monsoon depressions are suggested to influence the monsoon onset (e.g., Flatau *et al.*, 2003; Straub *et al.*, 2006).

The following questions will be explored in future studies.

1. What is the role of the Tibetan Plateau on South Asian summer monsoon onset?
2. How do simple theories built on idealized models relate to realistic monsoon onset?
3. How do the tropical transient disturbances influence the monsoon onset?

Realistic numerical simulations will be conducted, and the moist entropy budget during monsoon onset will be analyzed in order to provide insight into the dynamical mechanisms that modulate the timing of South Asian summer monsoon onset.

6.2 Madden-Julian Oscillation

Since the MJO, the dominant mode of intraseasonal variability in the tropics, was discovered in the early 1970s (Madden and Julian, 1971), it has been extensively studied and well documented (see review by Zhang, 2005). Under a recently proposed framework, the MJO is regarded as a moisture mode, where column-integrated moisture is the central prognostic variable.

A mechanism-denial study is conducted to examine the importance of influences from extratropical and circumnavigating waves, wind-evaporation feedback and radiative-convective feedback to the MJO. In particular, time-invariant forcing and nudging are implemented to maintain the climatology in the experiments, so as to reduce the interference from mean state changes, which is a common issue in previous mechanism-denial studies (e.g., Ray and Li, 2013). It is found that MJO activity remains largely unchanged with suppressed extratropical and circumnavigating waves, suggesting that the essential MJO dynamics are internal to the equatorial Indian and Pacific Oceans, consistent with the framework of moisture mode. The wind-evaporation feedback is shown to slow down propagation of the MJO. It is also found that the radiative-convective feedback is important to MJO amplitude, which is consistent with observations. The vertical profile of the radiative heating anomaly associated with the MJO is constructed using satellite products. The results show that the radiative heating anomaly, while in phase with the MJO, is characterized by a bottom-heavy vertical profile, which leads to a bottom-heavy divergent circulation, and results in further import of moist static energy into the column.

One challenge of MJO studies is to combine the complex numerical simulations with a simple idealized model so as to deepen the understanding of MJO dynamics. Many simple models have been proposed to explain the MJO (e.g., Fuchs and Raymond, 2002; Majda and Stechmann, 2009; Sobel and Maloney, 2012), but one common caveat is that it is difficult to relate the disturbances in simple models to the realistic MJO. Following Andersen and Kuang (2008), a 2D simple model with two vertical baroclinic modes and prognostic water vapor has been developed, which is able to produce some features of the tropical transients

such as convectively coupled equatorial waves. Guided by observations and results from state-of-the-art numerical simulations, I will further develop this simple model to study MJO dynamics. Essential mechanisms for the MJO identified in observation and realistic simulations will be implemented in the simple model.

6.3 Annular mode

The annular mode corresponds to the latitudinal shifts of the eddy-driven midlatitude jet, and is a dominant mode of variability of the extratropical circulation in both hemispheres on intraseasonal to interannual timescales (Kidson, 1988; Thompson and Wallace, 1998; Gong and Wang, 1999; Thompson and Wallace, 2000). It has been suggested that a positive feedback between anomalous zonal flow and eddy fluxes is responsible for the temporal persistence of the annular mode (e.g., LH01), and statistical methods have been used to quantify the strength of the eddy feedback (LH01; S13). However, the accuracy of these statistical methods are reduced by the mean-state-independent eddy forcing because of the quasi-oscillatory nature of eddies. Furthermore, a recent study showed that the existence of an internal eddy feedback cannot be distinguished from the presence of external interannual forcing using only the statistical methods (Byrne *et al.*, 2016).

In the present study, a linear response function (LRF) is used to identify the eddy response to anomalous mean flow associated with the annular mode in an idealized GCM, in which a positive eddy-jet feedback is confirmed unequivocally. The eddy feedback strength calculated using the LRF is 0.137 day^{-1} , which is used as a benchmark to evaluate three statistical methods. It is shown that previous statistical methods tend to underestimate the eddy feedback strength while a new method based on low-pass filtering proposed in the present study yield remarkably accurate result. The statistical methods are applied to the reanalysis data, and an eddy feedback strength of 0.121 day^{-1} associated with the Southern annular mode is found, which is presented as an improvement over previous estimates.

This work also highlights the importance of using sub-daily data in the analysis by showing the significant contribution of medium-scale waves of periods less than 2 days to

the annular mode dynamics, which was under-appreciated in most of previous research. It has been shown that the amplitude of these short period (smaller than 2 days) waves, which is weak in the climatology, is strongly modified by the annular mode. How does the annular mode modulate the medium-scale waves will be explored in the future.

The present study focuses on an equinoctial mean state in the idealized GCM. While a number of previous studies (e.g., Barnes and Hartmann, 2010; Byrne *et al.*, 2016; Sheshadri and Plumb, 2016) have brought attention to the seasonality of the annular mode. Seasonal variations of the persistence of the annular mode and eddy-jet feedback will be investigated using the present methodology.

Appendix A

Nudging on effective timescales longer than intraseasonal timescale

In the experiments where we aim to minimize changes to the mean state, the tendency of the state vector Ψ is described by the following equation:

$$\frac{\partial \Psi}{\partial t} = \mathbf{N}(\Psi) + \mathbf{g} + \mathbf{D}, \text{ and } \mathbf{D} = \frac{\Psi_m - \overline{\Psi}_c}{\tau}. \quad (\text{E1})$$

\mathbf{N} is a nonlinear operator representing the processes captured by the model. \mathbf{g} is the time-invariant forcing as in Hall (2000), and \mathbf{D} is the nudging (i.e., damping) term, with a damping time τ of 12 hours. Ψ_m is the moving average of Ψ , and $\overline{\Psi}_c$ is the mean state in the control. If Ψ_m is averaged over a period longer than the intraseasonal timescale, the intraseasonal variability will not be damped by the nudging term.

With Ψ_m^n (Ψ^n) denoting Ψ_m (Ψ) after n time steps, and $\Psi_m^0 = \Psi^0$ as the initial condition, Ψ_m^n is computed as:

$$\Psi_m^n = (1 - \Delta t / \tau_m) \Psi_m^{n-1} + (\Delta t / \tau_m) \Psi^n, n = 1, 2, 3... \quad (\text{E2})$$

τ_m limits the timescale over which the running mean is averaged, and is set to be 1000 days in this paper, while Δt , the time step, is 900 s. Equation E2 can be rewritten as,

$$\Psi_m^n = w_n \Psi^0 + \Delta t / \tau_m \sum_{i=0}^{n-1} w_i \Psi^{n-i}, n = 1, 2, 3..., \text{ where } w_i = (1 - \Delta t / \tau_m)^i \quad (\text{E3})$$

w_i can be viewed as a weight function for the moving average, and the weight function used in this paper is plotted in Figure S1A. The effective damping coefficients are different for oscillations with different periods (Figure S1B). The nudging time start from 0.5 day for infinitely long period, and increases as the period of the oscillations decreases. In particular, for the oscillations with a period of 68 days, the damping time is the same as the period.

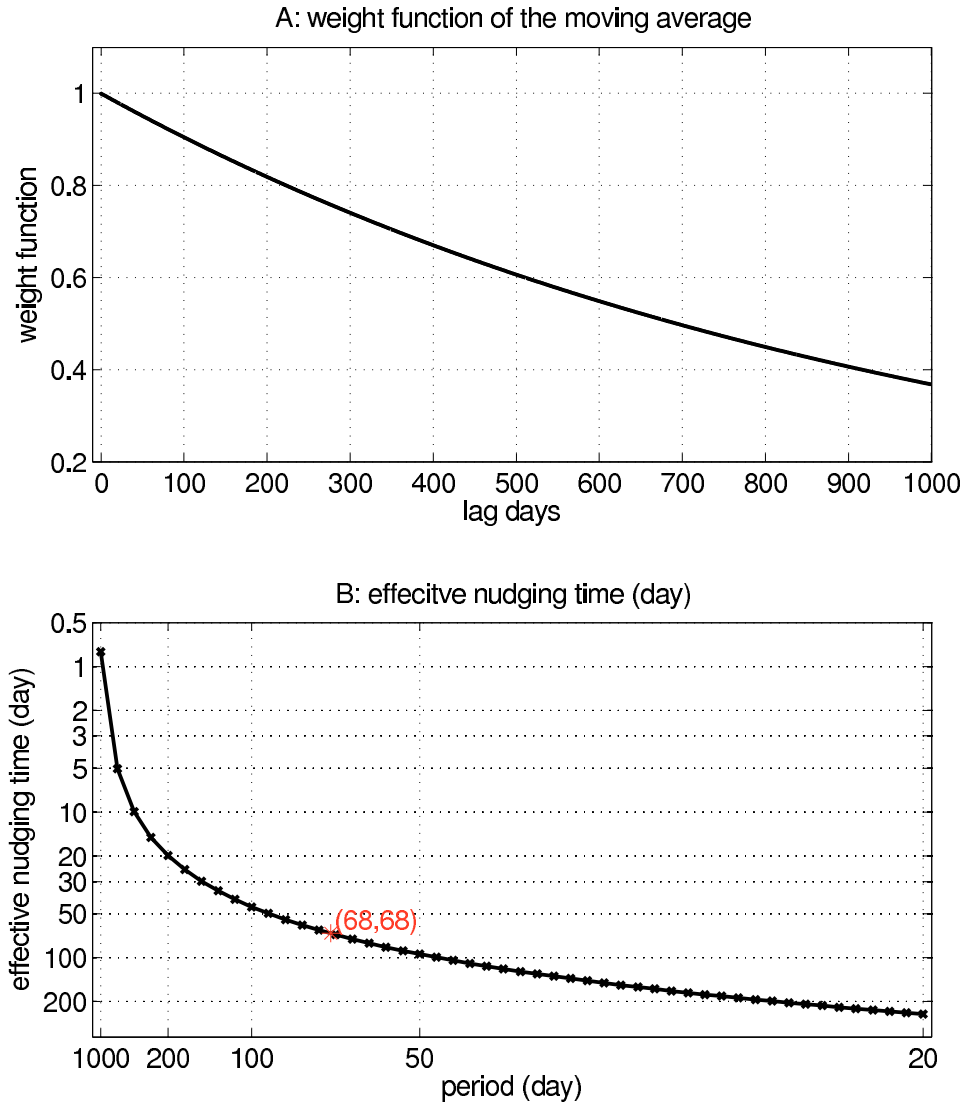


Figure S1: (A) the weight function of the moving average. (B) the effective damping time of the nudging term on oscillations with different periods. The red star denotes that for the oscillations with a period of 68 days, the effective damping time is the same as the period.

References

- ABE, M., KITO, A. and YASUNARI, T. (2003). An evolution of the Asian summer monsoon associated with mountain uplift – simulation with the MRI Atmosphere-Ocean Coupled GCM. *Journal of the Meteorological Society of Japan*, **81**, 909–933.
- AN, Z., KUTZBACH, J., PRELL, W. and PORTER, S. (2001). Evolution of Asian monsoons and phased uplift of the Himalaya-Tibetan plateau since Late Miocene times. *Nature*, **411**, 62–66.
- ANDERSEN, J. and KUANG, Z. (2008). A toy model of the instability in the equatorially trapped convectively coupled waves on the equatorial beta plane. *Journal of the Atmospheric Sciences*, **65**, 3736–3757.
- and — (2012). Moist static energy budget of MJO-like disturbances in the atmosphere of a zonally symmetric aquaplanet. *Journal of Climate*, **25**, 2782–2804.
- BALDWIN, M., STEPHENSON, D., THOMPSON, D., DUNKERTON, T., CHARLTON, A. and O’NEILL, A. (2003). Stratospheric memory and skill of extended-range weather forecasts. *Science*, **301**, 636–640.
- BALDWIN, M. P., STEPHENSON, D. and JOLLIFFE, I. (2009). Spatial weighting and iterative projection methods for EOFs. *Journal of Climate*, **22**, 234–243.
- BARNES, E. and HARTMANN, D. (2010). Dynamical feedbacks of the Southern annular mode in winter and summer. *Journal of the Atmospheric Sciences*, **67**, 2320–2330.
- BENEDICT, J., MALONEY, E., SOBEL, A. and DARGAN, M. (2014). Gross moist stability and MJO simulation skill in three full-physics GCMs. *Journal of the Atmospheric Sciences*, **71**, 1990–2008.
- and RANDALL, D. (2007). Observed characteristics of the MJO relative to maximum rainfall. *Journal of the Atmospheric Sciences*, **64**, 2332–2354.
- BONY, S. and EMANUEL, K. (2005). On the role of moist processes in tropical intraseasonal variability : cloud-radiation and moisture-convection feedbacks. *Journal of the Atmospheric Sciences*, **62**, 2770–2789.
- Boos, W. (2015). A review of recent progress on Tibet’s role in the South Asian monsoon. *CLIVAR Exchanges*, **19**, 23–27.

- and EMANUEL, K. (2009). Annual intensification of the Somali jet in a quasi-equilibrium framework: Observational composites. *Quarterly Journal of the Royal Meteorological Society*, **135**, 319–335.
- and HURLEY, J. (2013). Thermodynamic bias in the multimodel mean boreal summer monsoon. *Journal of Climate*, **26**, 2279–2287.
- and KUANG, Z. (2010). Dominant control of the South Asian monsoon by orographic insulation versus plateau heating. *Nature*, **463**, 218–223.
- and — (2013). Sensitivity of the South Asian monsoon to elevated and non-elevated heating. *Scientific Reports*, **3**, 1192.
- BYRNE, N., SHEPHERD, T., WOOLINGS, T. and PLUMB, R. A. (2016). Annular modes and apparent eddy feedbacks in the Southern Hemisphere. *Geophysical Research Letters*, **43**, 3897–3902.
- CANE, M. (2010). Climate: a moist model monsoon. *Nature*, **463**, 163–164.
- CHAKRABORTY, A., NANJUNDIAH, R. and SRINIVASAN, J. (2002). Role of Asian and African orography in Indian summer monsoon. *Geophysical Research Letters*, **29**, 50–51.
- , — and — (2006). Theoretical aspects of the onset of Indian summer monsoon from perturbed orography simulations in a GCM. *Annals of Geophysics*, **24**, 2075–2089.
- CHEN, G. and PLUMB, R. A. (2009). Quantifying the eddy feedback and the persistence of the zonal index in an idealized atmospheric model. *Journal of the Atmospheric Sciences*, **66**, 3707–3720.
- CHOU, C. and NEELIN, J. D. (2003). Mechanisms limiting the northward extent of the northern summer monsoons over North America, Asia, and Africa. *Journal of Climate*, **16**, 406–425.
- EMANUEL, K. (1987). An air-sea interaction model of intraseasonal oscillations in the tropics. *Journal of the Atmospheric Sciences*, **44**, 2324–2340.
- (1995). On thermally direct circulation in moist atmospheres. *Journal of the Atmospheric Sciences*, **52**, 1529–1534.
- , NEELIN, J. D. and BRETHERTON, C. (1994). On large-scale circulations in convecting atmospheres. *Quarterly Journal of the Royal Meteorological Society*, **120**, 1111–1143.
- , WING, A. and VINCENT, E. (2014). Radiative-convective instability. *Journal of Advances in Modeling Earth Systems*, **6**, 75–90.
- FELDSTEIN, S. and LEE, S. (1998). Is the atmospheric zonal index driven by an eddy feedback? *Journal of the Atmospheric Sciences*, **55**, 3077–3086.
- FLATAU, M., FLATAU, P., SCHMIDT, J. and KILADIS, G. (2003). Delayed onset of the 2002 Indian monsoon. *Geophysical Research Letters*, **30**, 28–31.

- FUCHS, Z. and RAYMOND, D. (2002). Large-scale modes of a non-rotating atmosphere with water vapor and cloud-radiation feedbacks. *Journal of the Atmospheric Sciences*, **59**, 1669–1679.
- GERBER, E., POLVANI, L. and ANCUKIEWICZ, D. (2008a). Annular mode time scales in the intergovernmental panel on climate change fourth assessment report models. *Geophysical Research Letters*, **35**, L22707.
- and VALLIS, G. (2007). Eddy-zonal flow interactions and the persistence of the zonal index. *Journal of the Atmospheric Sciences*, **64**, 3296–3311.
- , VORONIN, S. and POLVANI, L. (2008b). Testing the annular mode autocorrelation time scale in simple atmospheric general circulation models. *Monthly Weather Review*, **136**, 1523–1536.
- GHIL, M. and MO, K. (1991). Intraseasonal oscillations in the global atmosphere. Part I: Northern Hemisphere and tropics. *Journal of the Atmospheric Sciences*, **48**, 752–779.
- GILL, A. (1980). Some simple solutions for heat-induced tropical circulation. *Quarterly Journal of the Royal Meteorological Society*, **106**, 447–462.
- GONG, D. and WANG, S. (1999). Definition of Antarctic oscillation index. *Geophysical Research Letters*, **26**, 459–462.
- GOODMAN, J. and MARSHALL, J. (2002). Using neutral singular vectors to study low-frequency atmospheric variability. *Journal of the Atmospheric Sciences*, **59**, 3206–3222.
- HAHN, D. and MANABE, S. (1975). The role of mountains in the South Asian monsoon circulation. *Journal of the Atmospheric Sciences*, **32**, 1515–1541.
- HALL, N. (2000). A simple GCM based on dry dynamics and constant forcing. *Journal of the Atmospheric Sciences*, **57**, 1557–1572.
- HALLEY, E. (1686). An historical account of the trade winds, and monsoons, observable in the seas between and near the tropics, with an attempt to assign the physical cause of the said winds. *Philosophical Transactions of the Royal Society of London*, **16**, 153–168.
- HARTMANN, D. and LO, F. (1998). Wave-driven zonal flow vacillation in the Southern Hemisphere. *Journal of the Atmospheric Sciences*, **55**, 1303–1315.
- HASSANZADEH, P., FARRELL, B. and KUANG, Z. (2014). Responses of midlatitude blocks and wave amplitude to changes in the meridional temperature gradient in an idealized dry GCM. *Geophysical Research Letters*, **41**, 5223–5232.
- and KUANG, Z. (2015). Blocking variability: Arctic Amplification versus Arctic Oscillation. *Geophysical Research Letters*, **42**, 8586–8595.
- and — (2016a). The linear response function of an idealized atmosphere. Part I: Construction using Green’s functions and applications. *Journal of the Atmospheric Sciences*, **73**, 3423–3439.

- and — (2016b). The linear response function of an idealized atmosphere. Part II: Implications for the practical use of the Fluctuation-Dissipation Theorem and the role of operator's nonnormality. *Journal of the Atmospheric Sciences*, **73**, 3441–3452.
- HASSELMANN, K. (1976). Stochastic climate models: Part I. Theory. *Tellus*, **28**, 474–485.
- HE, H., MCGINNIS, J., SONG, Z. and YANAI, M. (1987). Onset of the Asian summer monsoon in 1979 and the effect of the Tibetan Plateau. *Monthly Weather Review*, **115**, 1966–1995.
- HELD, I. and SUAREZ, M. (1983). A proposal for the intercomparison of the dynamical cores of atmospheric general circulation models. *Bulletin of the American Meteorological Society*, **75**, 1825–1830.
- HOSKINS, B. and YANG, G.-Y. (2000). The equatorial response to higher-latitude forcing. *Journal of the Atmospheric Sciences*, **57**, 1197–1213.
- HSU, H.-H. (1996). Global view of the intraseasonal oscillation during Northern winter. *Journal of Climate*, **9**, 2386–2406.
- , HOSKINS, B. J. and JIN, F.-F. (1990). The 1985/86 intraseasonal oscillation and the role of the extratropics. *Journal of the Atmospheric Sciences*, **47**, 823–839.
- HU, Q. and RANDALL, D. (1994). Low-frequency oscillations in radiative-convective systems. *Journal of the Atmospheric Sciences*, pp. 1089–1099.
- HURLEY, J. and BOOS, W. (2013). Interannual variability of monsoon precipitation and local subcloud equivalent potential temperature. *Journal of Climate*, **26**, 9507–9527.
- JAMES, I. (1987). Suppression of baroclinic instability in horizontally sheared flows. *Journal of the Atmospheric Sciences*, **44**, 3710–3720.
- JIANG, X., WALISER, D., LI, J.-L. and WOODS, C. (2011). Vertical cloud structures of the boreal summer intraseasonal variability based on cloudsat observations and era-interim reanalysis. *Climate dynamics*, **36**, 2219–2232.
- JIN, F.-F. and HOSKINS, B. (1995). The direct response to tropical heating in a baroclinic atmosphere. *Journal of the Atmospheric Sciences*, **52**, 307–319.
- KHAIROUTDINOV, M. and RANDALL, D. (2001). A cloud resolving model as a cloud parameterization in the NCAR Community Climate System Model: preliminary results. *Geophysical Research Letters*, **28**, 3617–3620.
- and — (2003). Cloud resolving modeling of the ARM summer 1997 IOP: model formulation, results, uncertainties, and sensitivities. *Journal of the Atmospheric Sciences*, **60**, 607–625.
- , — and DEMOTT, C. (2005). Simulations of the atmospheric general circulation using a cloud-resolving model as a superparameterization of physical processes. *Journal of the Atmospheric Sciences*, **62**, 2136–2154.

- KHOUIDER, B. and MAJDA, A. (2006). A simple multicloud parameterization for convectively coupled tropical waves. Part I: Linear analysis. *Journal of the Atmospheric Sciences*, **63**, 1308–1323.
- KIDSON, J. (1988). Indices of the Southern Hemisphere zonal wind. *Journal of Climate*, **1**, 183–194.
- KILADIS, G., STRAUB, K. and HAERTEL, P. (2005). Zonal and vertical structure of the Madden-Julian Oscillation. *Journal of the Atmospheric Sciences*, **62**, 2790–2809.
- KIM, D. (2005). Application of MJO simulation diagnostics to climate models. *Journal of Climate*, **22**, 6413–6436.
- , SOBEL, A. and KANG, I.-S. (2011). A mechanism denial study on the Madden-Julian Oscillation. *Journal of Advances in Modeling Earth Systems*, **3**, M12007.
- KIRANMAYI, L. and MALONEY, E. (2011). Intraseasonal moist static energy budget in reanalysis data. *Journal of Geophysical Research: Atmospheres*, **116**.
- KNUTSON, T. and WEICKMANN, K. (1987). 30-60 day atmospheric oscillations: composite life cycles of convection and circulation anomalies. *Monthly Weather Review*, **115**, 1407–1436.
- KUANG, Z. (2008a). A moisture-stratiform instability for convectively coupled waves. *Journal of the Atmospheric Sciences*, **65**, 834–854.
- (2008b). Modeling the interaction between cumulus convection and linear gravity waves using a limited-domain cloud system-resolving model. *Journal of the Atmospheric Sciences*, **65**, 576–591.
- (2011). The wavelength dependence of the gross moist stability and the scale selection in the instability of column integrated moist static energy. *Journal of the Atmospheric Sciences*, **68**, 61–74.
- , BLOSSEY, P. and BRETHERTON, C. (2005). A new approach for 3d cloud-resolving simulations of large-scale atmospheric circulation. *Geophysical Research Letters*, **32**, L02809.
- KURODA, Y. and MUKOUGAWA, H. (2011). Role of medium-scale waves on the Southern annular mode. *Journal of Geophysical Research*, **116**, D22107.
- LAU, K. M., KIM, M. K. and KIM, K. M. (2006). Asian summer monsoon anomalies induced by aerosol direct forcing: the role of the Tibetan Plateau. *Climate Dynamics*, **26**, 855–864.
- and PHILLIPS, T. (1986). Coherent fluctuations of extratropical geopotential height and tropical convection in intraseasonal time scales. *Journal of the Atmospheric Sciences*, **43**, 1164–1181.
- L'ECUYER, T. and MCGARRAGH, G. (2010). A 10-year climatology of tropical radiative heating and its vertical structure from TRMM observations. *Journal of Climate*, **23**, 519–541.
- LEITH, C. (1975). Climate response and fluctuation dissipation. *Journal of the Atmospheric Sciences*, **32**, 2022–2026.

- LIEBMANN, B. and HARTMANN, D. (1984). An observational study of tropical-midlatitude interaction on intraseasonal time scales during winter. *Journal of the Atmospheric Sciences*, **41**, 3333–3350.
- LIN, H., BRUNET, G. and DEROME, J. (2007). Intraseasonal variability in a dry atmospheric model. *Journal of the atmospheric sciences*, **64**, 2422–2441.
- LIN, J.-L. (2006). Tropical Intraseasonal variability in 14 IPCC AR4 climate models. Part I: Convective signals. *Journal of Climate*, **19**, 2665–2690.
- and MAPES, B. E. (2004). Radiation budget of the tropical intraseasonal oscillation. *Journal of the Atmospheric Sciences*, **61**, 2050–2062.
- LORENZ, D. and HARTMANN, D. (2001). Eddy-zonal flow feedback in the Southern Hemisphere. *Journal of the Atmospheric Sciences*, **58**, 3312–3327.
- MA, D. and KUANG, Z. (2011). Modulation of radiative heating by the Madden-Julian Oscillation and convectively coupled Kelvin waves as observed by CloudSat. *Geophysical Research Letters*, **38**, L21813.
- MADDEN, R. and JULIAN, P. (1971). Detection of a 40-50 day oscillation in the zonal wind in tropical pacific. *Journal of the Atmospheric Sciences*, **28**, 702–708.
- MALONEY, E. (2009). The moist static energy budget of a composite tropical intraseasonal oscillation in a climate model. *Journal of Climate*, **22**, 711–729.
- , SOBEL, A. and HANNAH, W. (2010). Intraseasonal variability in an aquaplanet general circulation model. *Journal of Advances in Modeling Earth Systems*, **2**, 5.
- and WOLDING, B. (2015). Initiation of an intraseasonal oscillation in an aquaplanet general circulation model. *Journal of Advances in Modeling Earth Systems*, **7**, 1956–1976.
- MAPES, B. (2000). Convection inhibition, subgridscale triggering, and stratiform instability in a toy tropical wave model. *Journal of the Atmospheric Sciences*, **57**, 1515–1530.
- MASUNAGA, H., SATOH, M. and MIURA, H. (2008). A joint satellite and global cloud-resolving model analysis of a Madden-Julian Oscillation event: Model diagnosis. *Journal of Geophysical Research: Atmospheres*, **113**, D17210.
- MATTHEWS, A., HOSKINS, B. and MASUTANI, M. (2004). The global response to tropical heating in the Madden-Julian Oscillation during the Northern winter. *Quarterly Journal of the Royal Meteorological Society*, **130**, 1991–2011.
- MCGRAW, M. and BARNES, E. (2016). Seasonal sensitivity of the eddy-driven jet to tropospheric heating in an idealized AGCM. *Journal of Climate*, **29**, 5223–5240.
- MOLNAR, P., BOOS, W. and BATTISTI, D. (2010). Orographic controls on climate and paleoclimate of Asia: thermal and mechanical roles for the Tibetan Plateau. *Annual Review of Earth and Planetary Sciences*, **38**, 77–102.

- NAMIAS, J. (1950). The index cycle and its role in the general circulation. *Journal of Meteorology*, **7**, 130–139.
- NEELIN, J. D., HELD, I. and COOK, K. (1987). Evaporation-wind feedback and low-frequency variability in the tropical atmosphere. *Journal of the Atmospheric Sciences*, **44**, 2341–2348.
- NIE, Y., ZHANG, Y., CHEN, G., YANG, X.-Q. and BURROWS, D. (2014). Quantifying barotropic and baroclinic eddy feedbacks in the persistence of the Southern Annular Mode. *Geophysical Research Letters*, **41**, 8636–8644.
- NIGAM, S. (1990). On the structure of variability of the observed tropospheric and stratospheric zonal-mean zonal wind. *Journal of the Atmospheric Sciences*, **47**, 1799–1813.
- PARK, H.-S., CHIANG, J. and BORDONI, S. (2012). The mechanical impact of the Tibetan Plateau on the seasonal evolution of the South Asian monsoon. *Journal of Climate*, **25**, 2394–2407.
- PRELL, W. and KUTZBACH, E. (1992). Sensitivity of the Indian monsoon to forcing parameters and implications for its evolution. *Nature*, **360**, 647–652.
- PRITCHARD, M. and BRETHERTON, C. (2014). Causal evidence that rotational moisture advection is critical to the superparameterized Madden-Julian Oscillation. *Journal of the Atmospheric Sciences*, **71**, 800–815.
- PRIVE, N. and PLUMB, R. A. (2007a). Monsoon dynamics with interactive forcing. Part I: Axisymmetric studies. *Journal of the Atmospheric Sciences*, **64**, 1417–1430.
- and — (2007b). Monsoon dynamics with interactive forcing. Part II: Impact of eddies and asymmetric geometries. *Journal of the Atmospheric Sciences*, **64**, 1431–1442.
- RAJAGOPALAN, B. and MOLNAR, P. (2013). Signatures of Tibetan Plateau heating on Indian summer monsoon rainfall variability. *Journal of Geophysical Research: Atmospheres*, **118**, 1170–1178.
- RAY, P. and LI, T. (2013). Relative roles of circumnavigating waves and extratropics on the MJO and its relationship with the mean state. *Journal of the Atmospheric Sciences*, **70**, 876–893.
- and ZHANG, C. (2010). A case study of the mechanics of extratropical influence on the initiation of the Madden-Julian Oscillation. *Journal of the Atmospheric Sciences*, **67**, 515–528.
- , —, DUDHIA, J. and CHEN, S. (2009). A numerical case study on the initiation of the Madden-Julian Oscillation. *Journal of the Atmospheric Sciences*, **66**, 310–331.
- RAYMOND, D. (2001). A new model of the Madden-Julian Oscillation. *Journal of the Atmospheric Sciences*, **58**, 2807–2819.
- and FUCHS, Z. (2007). Convectively coupled gravity and moisture mode in a simple atmospheric model. *Tellus A*, **59**, 627–640.

- RILEY, E., MAPES, B. and TULICH, S. (2011). Clouds associated with the Madden-Julian Oscillation: A new perspective from CloudSat. *Journal of the Atmospheric Sciences*, **68**, 876–893.
- RING, M. and PLUMB, R. A. (2008). The response of a simplified GCM to axisymmetric forcing: Applicability of the Fluctuation-Dissipation Theorem. *Journal of the Atmospheric Sciences*, **65**, 3880–3898.
- ROBINSON, W. (2000). A baroclinic mechanism for the eddy feedback on the zonal index. *Journal of the Atmospheric Sciences*, **57**, 415–422.
- ROSSBY, C.-G. (1939). Relation between variations in the intensity of the zonal circulation of the atmosphere and the displacements of the semi-permanent centers of action. *Journal of Marine Research*, **2**, 38–55.
- SATO, K., YAMADA, K. and HIROTA, I. (2000). Global characteristics of medium-scale tropopausal waves observed in ECMWF operational data. *Monthly Weather Review*, **128**, 3808–3823.
- SCHNEIDER, T. (2006). The general circulation of the atmosphere. *Annual Review of Earth and Planetary Sciences*, **34**, 655–688.
- and BORDONI, S. (2008). Eddy-mediated regime transitions in the seasonal cycle of a Hadley Circulation and implications for monsoon dynamics. *Journal of the Atmospheric Sciences*, **65**, 915–934.
- SHAW, T. (2014). On the role of planetary-scale waves in the abrupt seasonal transition of the Northern Hemisphere general circulation. *Journal of the Atmospheric Sciences*, **71**, 1724–1746.
- SHESHADRI, A. and PLUMB, R. A. (2016). Sensitivity of the surface responses of an idealized AGCM to the timing of imposed ozone depletion-like polar stratospheric cooling. *Geophysical Research Letters*, **43**, 2330–2336.
- SIMPSON, I., SHEPHERD, T., HITCHCOCK, P. and SCINOCICA, J. (2013). Southern annular mode dynamics in observations and models. Part II: eddy feedbacks. *Journal of Climate*, **26**, 5220–5241.
- SOBEL, A. and MALONEY, E. (2012). An Idealized Semi-Empirical Framework for Modeling the Madden-Julian Oscillation. *Journal of the Atmospheric Sciences*, **69**, 1691–1705.
- , —, BELLON, G. and FRIERSON, D. (2008). The role of surface heat fluxes in tropical intraseasonal oscillations. *Nature Geoscience*, **1**, 653–657.
- , —, — and — (2010). Surface fluxes and tropical intraseasonal variability: A reassessment. *Journal of Advances in Modeling Earth Systems*, **2**, 2.
- , WANG, S. and KIM, D. (2014). Moist static energy budget of the MJO during DYNAMO. *Journal of the Atmospheric Sciences*, **71**, 4276–4291.

- STEPHENS, G., VANE, D., BOAIN, R., MACE, G., SASSEN, K., WANG, Z., ILLINGWORTH, A., O'CONNOR, E., ROSSOW, W., DURDEN, S. *et al.* (2002). The CloudSat mission and the A-Train: A new dimension of space-based observations of clouds and precipitation. *Bulletin of the American Meteorological Society*, **83**, 1771–1790.
- STRAUB, K. and KILADIS, G. (2002). Observations of a convectively coupled Kelvin wave in the eastern Pacific ITCZ. *Journal of the Atmospheric Sciences*, **59**, 30–53.
- , — and CIESIELSKI, P. (2006). The role of equatorial waves in the onset of the South China Sea summer monsoon and the demise of El Nino during 1998. *Dynamics of Atmospheres and Oceans*, **42**, 216–238.
- SUGIYAMA, M. (2009). The moisture mode in the quasi-equilibrium tropical circulation model. Part I: Analysis based on the weak temperature gradient approximation. *Journal of the Atmospheric Sciences*, **66**, 1507–1523.
- THOMPSON, D. and LI, Y. (2015). Baroclinic and barotropic annular variability in the Northern Hemisphere. *Journal of the Atmospheric Sciences*, **72**, 1117–1136.
- and WALLACE, J. (1998). The Arctic Oscillation signature in the wintertime geopotential height and temperature fields. *Geophysical Research Letters*, **25**, 1297–1300.
- and — (2000). Annular mode in the extratropical circulation. Part I: month-to-month variability. *Journal of Climate*, **13**, 1000–1016.
- and WOODWORTH, J. (2014). Barotropic and baroclinic annular variability in the Southern Hemisphere. *Journal of the Atmospheric Sciences*, **71**, 1480–1493.
- TIAN, B. and RAMANATHAN, V. (2003). A simple moist tropical atmosphere model: The role of cloud radiative forcing. *Journal of Climate*, **16**, 2086–2092.
- , WALISER, E., FETTER, E., LAMBRIGTSEN, B., YUNG, Y. and WANG, B. (2006). Vertical moist thermodynamic structure and spatial temporal evolution of the MJO in AIRS observations. *Journal of the Atmospheric Sciences*, **63**, 2462–2485.
- VALLIS, G., GERBER, E., KUSHNER, P. and CASH, B. (2004). A mechanism and simple dynamical model of the North Atlantic Oscillation and annular modes. *Journal of the Atmospheric Sciences*, **61**, 264–280.
- WALISER, D., LI, J.-L., WOODS, C., AUSTIN, R., BACMEISTER, J., CHERN, J., DEL GENIO, A., JIANG, J., KUANG, Z., MENG, H., MINNIS, P., PLATNICK, S., ROSSOW, W., STEPHENS, G., SUN-MACK, S., TAO, W.-K., TOMPKINS, A., VANE, D., WALKER, C. and WU, D. (2009). Cloud ice: A climate model challenge with signs and expectations of progress. *Journal of Geophysical Research: Atmospheres*, **114**, D00A21.
- WALLACE, J. (2000). North Atlantic Oscillation/annular mode: Two paradigms – one phenomenon. *Quarterly Journal of the Royal Meteorological Society*, **126**, 791–805.
- and HSU, H.-H. (1985). Another look at the index cycle. *Tellus A*, **37**, 478–486.

- WANG, B., WU, R. and LAU, K. M. (2001). Interannual variability of the Asian summer monsoon: contrasts between the Indian and the Western North Pacific-East Asian monsoons. *Journal of Climate*, **14**, 4073–4090.
- WEBSTER, P. and YANG, S. (2012). Monsoon and ENSO: Selectively interactive systems. *Scientific Reports*, **2**, 404.
- WEICKMANN, K. (1983). Intraseasonal circulation and outgoing longwave radiation modes during Northern Hemisphere winter. *Monthly Weather Review*, **5**, 1838–1858.
- WHEELER, M. and KILADIS, G. (1999). Convectively coupled equatorial waves: analysis of clouds and temperature in the wavenumber-frequency domain. *Journal of the Atmospheric Sciences*, **56**, 374–399.
- WING, A. and EMANUEL, K. (2013). Physical mechanisms controlling self-aggregation of convection in idealized numerical modeling simulations. *Journal of Advances in Modeling Earth Systems*, **5**, 1–14.
- WU, G., LIU, Y., HE, B., BAO, Q., DUAN, A. and JIN, F. (2012). Thermal controls on the Asian summer monsoon. *Scientific Reports*, **2**, 404.
- and ZHANG, Y. (1998). Tibetan Plateau forcing and the timing of the monsoon onset over South Asia and the South China Sea. *Monthly Weather Review*, **126**, 913–927.
- YANAI, M., LI, C. and SONG, Z. (1992). Seasonal heating of the Tibetan Plateau and its effects on the evolution of the Asian summer monsoon. *Journal of the Meteorological Society of Japan*, **70**, 189–211.
- YASUNARI, T., SAITO, K. and TAKATA, K. (2006). Relative roles of large-scale orography and land surface processes in the global hydroclimate. Part I: impacts on monsoon systems and the tropics. *Journal of Hydrometeorology*, **7**, 626–641.
- YEH, T.-C., LO, S.-W. and SHU, P.-C. (1957). The wind structure and heat balance in the lower troposphere over Tibetan Plateau and its surroundings. *Acta Meteorologica Sinica*, **28**, 108–121.
- ZHANG, C. (2005). Madden-Julian Oscillation. *Reviews of Geophysics*, **43**, RG2003.
- and DONG, M. (2004). Seasonality in the Madden-Julian Oscillation. *Journal of Climate*, **17**, 3169–3180.